ABSTRACT

Title of Document: PASSIVE VIBRAION CONTROL OF PERIODIC DRILL STRING

Yaser A. Alsaffar, Doctoral of Philosophy, 2018

Directed By: Professor Amr Baz, Department of Mechanical Engineering

In this dissertation, the stop and pass bands (*i.e.* the band gaps) characteristics are determined for gyroscopic systems by developing an approach which is compatible with such class of systems which is based on the concept of Bloch wave propagation in periodic structures. In this approach, the dispersion curves of the periodic gyroscopic systems are determined for different rotational speeds. The obtained characteristics are compared with non-rotating systems in an attempt to quantify the effect of the gyroscopic forces on the "*band gap*" characteristics. The developed approach is illustrated by a new class of drill strings with passive periodic inserts. These inserts are utilized to filter out the vibration transmission along the drill string. Such mechanical filtering capabilities allow the vibrations to propagate along the periodic drill string only within specific frequency bands called the '*pass bands*' and completely block it within other frequency bands called the '*stop bands*'. The inserts introduce impedance mismatch zones along the vibration transmission path to impede the propagation of vibration along the drill string. The design and the location of the inserts are optimized to confine the dominant modes of vibration of the drill string within the stop bands generated by the periodic arrangement of the inserts in order to completely block the propagation of the vibrations.

A finite element model (*FEM*) that simulates the operation of this new class of drill strings is developed to describe the complex nature of the vibration encountered during drilling operations. The *FEM* is used to extract the dispersion characteristics of the gyroscopic unit cell of the drill string in order to determine its stop and pass band characteristics. Experimental prototype of the passive periodic drill string is built and tested to demonstrate the feasibility and effectiveness of the concept of periodic drill string

in mitigating undesirable vibrations. The experimental results are used to validate the developed theoretical model in order to develop a scalable design tool that can be used to predict the dynamical behavior of this new class of drill strings.

PASSIVE VIBRATION CONTROL
OF
PERIODIC DRILL STRING

By

Yaser A. Alsaffar

Dissertation submitted to the Faculty of the Graduate School of the
University of Maryland, College Park, in partial fulfillment
of the requirements for the degree of
Doctoral of Philosophy
2018

Advisory Committee:
Professor Amr Baz, Chair
Professor Abhijit Dasgupta
Associate Professor Peter Chung
Associate Professor Teng Li
Assistant Professor Jin-Oh Hahn
Professor Inderjit Chopra, Dean's Representative

Dedication

I dedicate this dissertation to

My Beloved Parents & Parents-In-Law
For their prayers, kindness, endless support & relentless encouragement

My Lovely Wife
For her sacrifices, persistent patience & heartfelt support

My Adorable Children
For the enduring joy they bring to my life

Acknowledgements

In the name of Allah, the Most Gracious, the Most Merciful

First and foremost, all praise to Allah, Almighty who empowered me with strength, knowledge, ability and opportunity to purse my graduate studies and to accomplish the completion of my research work competently. This achievement would not have been possible without Almighty Allah's relentless grace and mercy.

I wish to thank and express my sincere gratitude to my respected mentor and academic advisor Professor Amr Baz, Minta Martin Professor & Director of Smart Materials and Structures Research Center at the University of Maryland, for his heartfelt support, invaluable guidance, and endless encouragement throughout the course of my research work. His immense knowledge of research and pioneer ideas have improved my research skills substantially.

I am deeply indebted to my parents, parents-in-law and wife whose prayers, generosity, and enduring love have been a lifetime blessing. Thank you for your persistent patience and support. All your sacrifices are highly appreciated.

Special thanks are due to Dr. Sadok Sassi, Associate Professor at Qatar University, for his invaluable technical inputs and for the support from Qatar National Research Foundation (QNRF) for funding this work under grant number NPRP No.: 7-124-2-060.

I would like to thank Mr. Majid Aroom, Faculty Specialist at University of Maryland Machine Shop, for his guidance and assistance with the experimental set-up.

I humbly extend my thanks to my colleagues Dr. Mostafa Nouh, Assistant Professor at University of Bufalo, Dr. Abdul Aziz AlAdwani, Assistant Professor at Public Authority

for Applied Education and Training - Kuwait, Yaqoub Abdullah, Mohammad Raafat, for their discussions, suggestions and criticism.

Thanks are also due to the University of Maryland Supercomputing resources (http://www.it.umd.edu/hpcc) made available for conducting the research reported in this dissertation.

I would like to also thank Kuwait Oil Company, a subsidiary of Kuwait Petroleum Corporation, for granting me a scholarship to purse my Ph.D. degree.

Finally yet importantly, I wish to thank my committee members Dr. Abhijit Dasgupta, Dr. Peter Chung, Dr. Teng Li, Dr. Jin-Oh Hahn and Dr. Inderjit Chopra for their support, encouragements and invaluable technical inputs.

Table of Contents

List of Tables

List of Figures

Chapter 1

Introduction

1.1 Overview

Drilling rigs are machines used to bore holes into the earth's crust in order to extract natural resources such as crude oil, natural gas, water and mineral materials. Typically, the main components associated with the drilling rigs are hoisting, fluid circulation, rotary table and drill string systems. The hoisting system is used to support the drill string while the rotary table system provides the necessary torque to rotate the drill string. The fluid circulation system not only provides the proper cooling and lubrication to the drill string but also extracts the waste of rock chips and soil from the drill bit to the surface. Fig. 1.1 displays a schematic drawing of a typical drilling rig machine.

1.1.1 Drill String Major Components

Drill string system, which is the primary focus of this dissertation, is a slender complex structure comprises essentially of two sections, namely drill pipes and Bottom-Hole-Assembly (*BHA*). The main function of the drill string system is to transmit the required torque provided at the surface by the rotary table system to the drill bit. Also the drill string transfers the hydraulic fluid, known as drilling mud, to the drill bit. Depending on the type of drilling applications, the drill string can extend several kilometers below the earth surface. Drill string major components are presented in Fig. 1.4.

Drill pipes are hollow steel pipes joined together to form along continuous structure which constitutes most of the length of the drill string system. The length of this section ranges between 1 to 8 kilometers long. Therefore, the drill pipes are designed to operate in tension. Typically, the pipes have outside diameter between 9 to 15 cm and wall thickness of approximately 1 cm.

The *BHA* consists of three main components, namely drill bit, drill collars and stabilizers. The drill bit is a cutting mechanism attached at the bottom of the *BHA* which is capable of crushing or shearing rocks. The drill collars are similar to the drill pipes except that they are larger in diameter. The primary objective of the drill collars is to generate the weight necessary to bore into the earth's crust with sufficient force. Such force is called Weight-On-Bit (*WOB*) which typically ranges from 10^4 to 10^6 N [1]. Therefore, the *BHA* is designed to operate mostly in compression with neutral point located at 80 to 95% of its total length for a particular *WOB* which allows for a margin of WOB overload [2]. Usually the drill collars outside diameter ranges between 10 to 25 centimeters and the wall thickness ranges between 6 to 16 centimeters. The *BHA* has a length of approximately 100 to 300 meters.

Stabilizers are downhole tools placed above the drill bit and along the drill collars in order to hold the drill collars in the center of the borehole and to avoid sidetracking. In addition, the stabilizers keep the drill bit perpendicular to the drilling surface thereby optimizing its performance. The stabilizers blades are usually of the same diameter as that of the drill bit and the distance between the stabilizers can range from 5 to 50 meters.

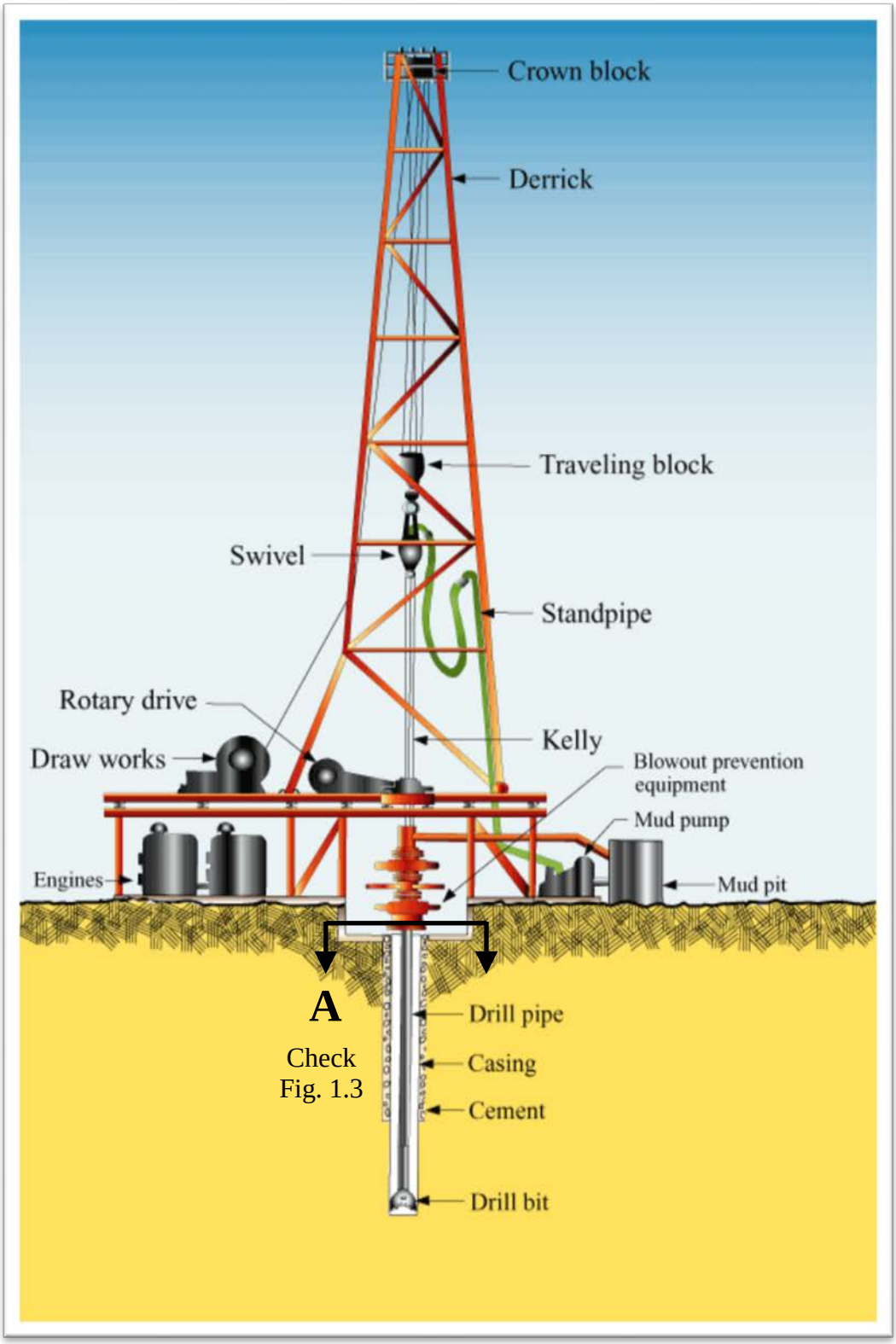

Fig. 1.1 Schematic drawing of typical oil well drilling rig, California Department of Conservation

1.1.2 Drill String Vibration Modes

The dynamical behavior of drill strings is extremely complex problem. The complexity stems from the fact that a typical drill string has a diameter-to-length ratio of about 10^{-5}, which is of same order of magnitude as an average human hair. Furthermore, such long and slender structures are usually subjected to complex simultaneous vibrational phenomena which need to be adequately analyzed and efficaciously controlled to avoid undesirable destructive potential. During drilling process, the drill strings vibration modes can be categorized as longitudinal, torsional and lateral according to vibrations direction. Each vibration mode has its own destructive nature affecting the drill string overall performance. Fig. 1.2 depicts drill string vibration modes.

Drill string longitudinal (axial) mode creates a vibration motion parallel to its axis. This mode of vibration is induced by a phenomenon known as a *bit-bounce*. When it happens, this instability causes the drill bit to lose contact with rack surface intermittently. Consequently, bit bounce phenomenon strongly influences the drill string response to the applied Weight-On-Bit (*WOB*) and severely damages the drill bit cutting structure such as bearings and seals [3].

The vibration resistance to rotation results in torsional vibrations which are induced by virtue of the *stick-slip* phenomenon that make the drill bit stops rotating for short periods causing the drill string to periodically torque up and spin freely to reach speeds as high as ten times the rotary table speed [4]. The nonlinear interaction between the frictional torque and the angular velocity at the bit results in extensive bit wear, severe shock loading, fatigue and eventually equipment failure.

Lateral (transverse) vibration mode is side-to-side motion that generates an eccentric rotation of the drill string and the Bottom-Hole-Assembly (*BHA*) around a point other than their geometric center. Such a motion is known as the whirling phenomenon. This vibration mode is widely recognized as the most damaging stress form in drilling assemblies and as a leading cause of *BHA* failure. Also, transverse oscillations of the drill string severely damage the wellbore wall and affect the overall drilling operation [5].

During drilling process, the drill string longitudinal, torsional and lateral vibration modes occur usually simultaneously. The combined effects of the coupled drill string modes of vibration dramatically increase the complexity of drill string analysis. A summary of the different modes of vibrations encountered by the drill strings and the associated physical mechanisms contributing to such modes is given by [6] and Table 1.1 lists these modes and the corresponding mechanisms as reported by [7].

Table 1.1 Drill string excitation mechanisms [7]

Physical Mechanism	Primary Excitation	Secondary Excitation
Mass Imbalance	Lateral	Axial-Torsional-Lateral
Misalignment	Lateral	Axial
Three-Cone Bit	Axial	Torsional-Lateral
Loose Drill String	Axial-Torsional-Lateral	
Rotational Walk	Lateral	Axial-Torsional
Asynchronous Whirl	Lateral	Axial-Torsional
Drill String Whip	Lateral	Axial-Torsional

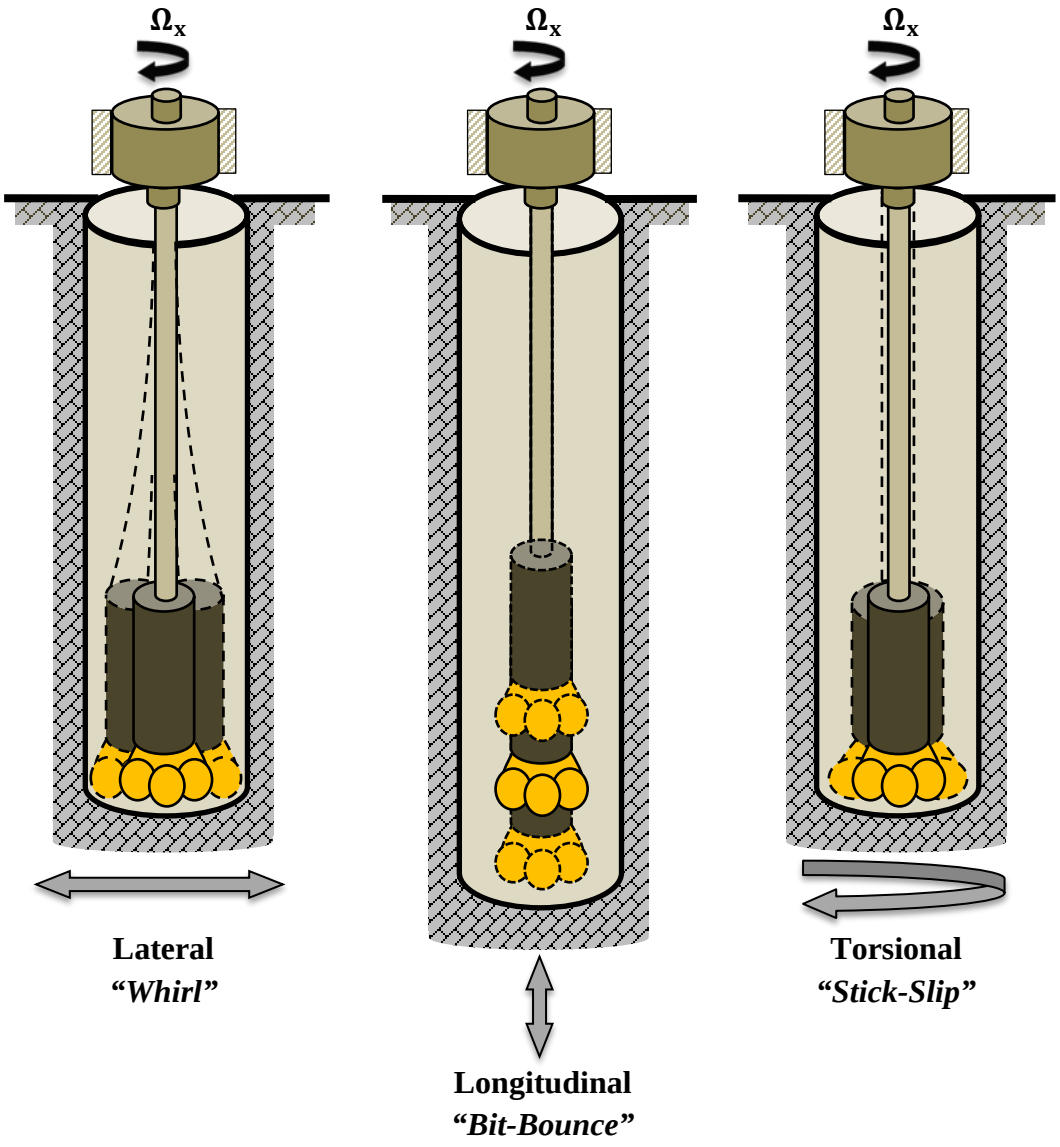

Fig. 1.2 Drill string vibration modes

1.2 Literature Review

Extensive efforts have therefore been exerted during the past decades to understand the underlying physical phenomena governing such complex vibration behavior of the drill strings to develop appropriate means for mitigating the resulting

destructive effects. These efforts include the mathematical modeling, simulation, and/or experimental investigation. Examples of these efforts include the work of [6-31].

In 1986, [8] presented the first theoretical and experimental investigation of the vibration of full-scale drilling rig. In 1991, [9] modeled the Bottom-Hole-Assembly (*BHA*) to study the nonlinearities due to the interaction between the drill string and the outer shell. [10], presented a finite element model of transverse vibration of drill strings under axial loading in 1995. A linear finite element model has been developed by [11] in 2005 to predict the buckling loads and critical rotational speeds of the drill strings. In 1996 and 1997, [12] and [13] developed finite element models to study the coupled torsional and bending vibration as well as the axial and transverse vibrations of passive drill strings. In 2000 and 2003, their models were extended to simulate the dynamics of drill strings with active control capabilities. Similar attempt has been reported by [14] in 2003 to control the nonlinearly coupled torsional and bending vibration of drill string. The effect of interaction with the bore hole has been analyzed theoretically by [13] and both theoretically experimentally by [15]. The effect of stick-slip and whirl vibrations on the stability and bifurcation of drill strings were studied by [16] using a two degrees-of-freedom model. In 2006 [17] presented an extensive study of the limit cycles of torsional vibrations of drill strings subjected to constant input torque. Also the equilibrium points are determined and related stability properties are discussed. In 2007, [18] extended their finite element model to study the dynamics of drill string system in the presence of *stick-slip* excitations.

Several attempts have been carried out to suppress passively the vibration of drill strings. Distinct among these attempts are the nonlinear energy sink approach of [19], the magnetorheological damping method of [20], the adjustable vibration absorber of [21] and the anti-stalling technology (AST) and V-stab vibration reduction tools of [22].

In all the previously mentioned studies, the emphasis has been placed on conventional drill strings of uniform cross sections. No attempt has been made to consider radically different designs such as periodic drill strings in spite of the potential of this class of drill strings in minimizing the vibration transmission. It is therefore the purpose of this dissertation to introduce the concept of periodic drill strings, and demonstrate theoretically and experimentally its unique mechanical filtering characteristics. Particular focus is placed on filtering out the transverse vibrations of the periodic drill string.

1.3 The Concept of Passive Periodic Drill Strings

The concept of the periodic drill strings can be best understood by considering the schematic drawing displayed in Fig. 1.4. The periodic drill strings in Fig. 1.4 will be provided with optimally designed and placed periodic inserts which can be either passive or active. The passive inserts will introduce zones of impedance mismatch along the vibration transmission path to impede the propagation through geometrical or material discontinuities. In addition, the design and the location of the inserts can be optimized to confine the dominant modes of vibrations of the drill string within the stop bands generated by the periodic arrangement of the inserts.

It is important to note that the concept and filtering characteristics of periodic drill string is particularly suitable for mitigating and blocking the vibration over a wide range of drilling depths as shown in Fig. 1.3. The figure indicates that at shallow drilling depth, the drill string dominant natural frequency is usually high and is bounded to lie inside the stop band. However, as the drilling depth becomes deeper, the drill string becomes longer and softer, hence is likely to vibrate at higher amplitudes. If the periodic inserts are designed properly, then the corresponding dominant natural frequency can still be confined within the stop band. Thus, the expected severe vibrations can be completely blocked. This is unlike the current conventional drill strings, which can be operated effectively at one operating condition only (either speed or drilling depth).

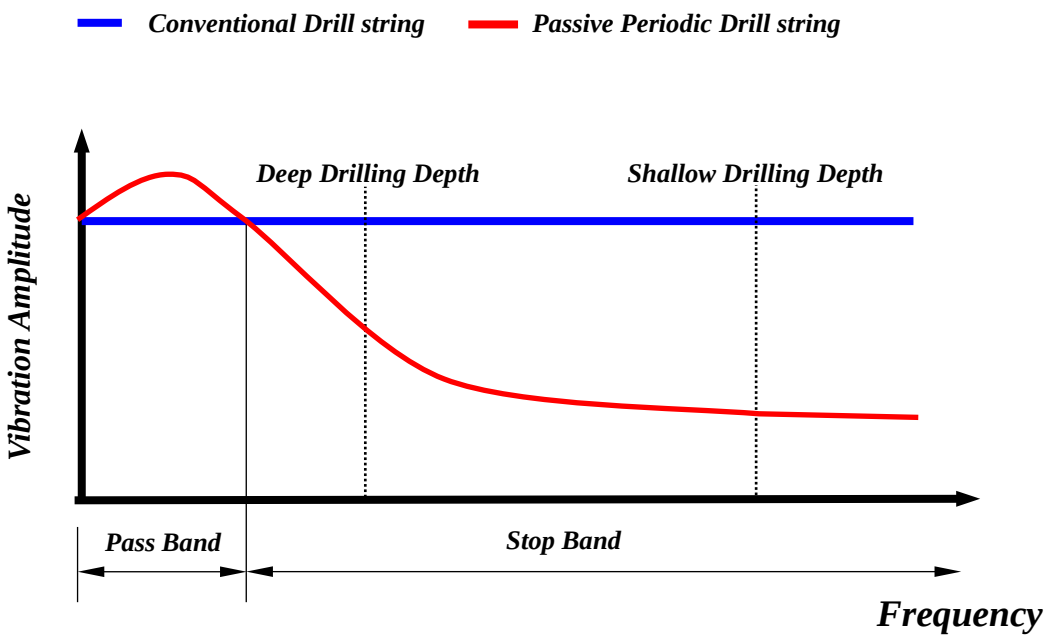

Fig. 1.3 Vibration mitigation characteristics of conventional & periodic drill strings

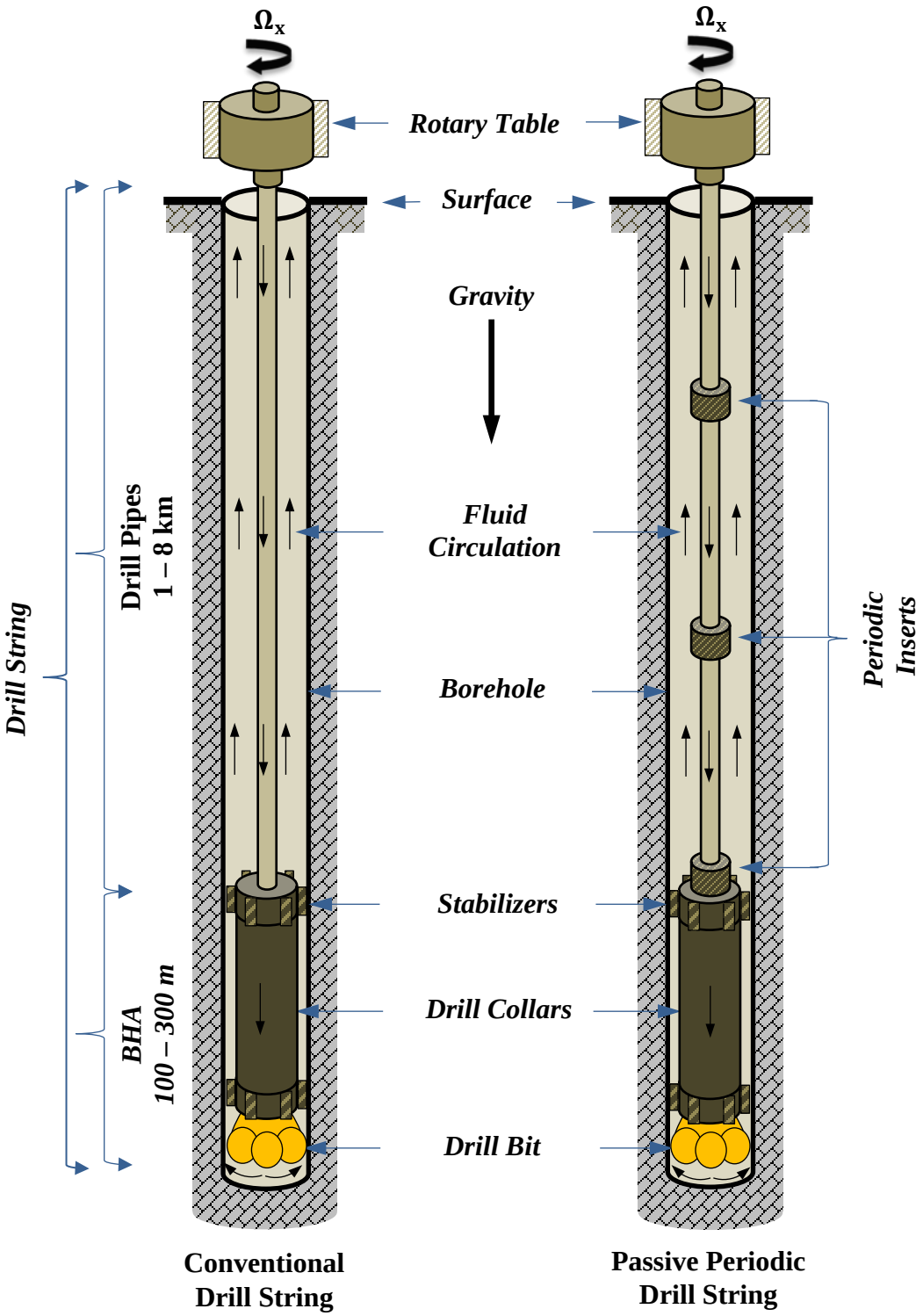

Fig. 1.4 Conventional & Periodic Drill string schematic drawing (Fig. 1.1 - section A)

1.4 Scope of the Dissertation

There is no doubt that all major oil companies are always pursuing cutting-edge technologies to balance the continuously rising global demand for oil with an equal increase in the exploration and production activities. Such a balance can only be achieved through drilling technology that pushes the envelope of the state-of-the-art.

In this work, I have attempted to present a new class of drill strings that can meet such future challenges and enables fast drilling with minimal down time due to premature failures because of excessive vibration. The proposed concept of periodic drills strings can be a viable solution to mitigate the catastrophic problems that arise from excessive vibrations. With such a new class of drill strings, the interaction between the drill collars and the bore hole can be minimized, the whirling effect can be reduced, and the most importantly the effect of the drill bounce can be decreased.

The objective of this dissertation is to develop the theory governing the operation of this new class of drill strings to account for the simultaneous longitudinal, torsional and lateral vibrations. Experimental prototype is built and tested to demonstrate the feasibility of the concept of periodic drill string in mitigating undesirable vibrations. The experimental results are used to validate the theoretical model in order to develop a scalable design tool that maybe used in real life drilling applications to predict the dynamical behavior of this new class of drill strings. It is important to note that the manufacturing of the proposed passive and active periodic drill string will require minimal modification of the designs of conventional drill string as the periodic inserts can be manufactured as an integral part of each drill pipe section.

The aforementioned objectives are achieved by organizing the dissertation in five chapters. Chapter 1 briefly summarizes the literature review and introduces the concept of passive periodic drill strings. In chapter 2, a finite element model of conventional drill string is developed and validated by considering four different simulations. Chapter 3 presents the theory of periodic structures as well as the Bloch wave propagation theory, which govern the operation of passive periodic drill string. In addition, numerical examples of passive drill string are presented and compared with the conventional drill string to emphasize the potential and merit of the proposed new class of periodic drill string. In chapter 4, the prediction of finite element model is validated against the performance of experimental prototype of both the conventional and periodic drill strings. Chapter 5 summarizes the conclusions of the arrived at theoretical and experimental results. Furthermore, a brief summary of the future extension of this dissertation is outlined. Also, the major contributions of this dissertation are presented.

1.5 Summary

This chapter has presented the major components and the modes of vibration of the drill string and a brief review of the literature of the underlying physical phenomena governing such complex vibration behavior of the drill strings in order to develop appropriate means for mitigating the resulting destructive effects. The concept of passive drill string has been briefly introduced. The significance and the objective of the present work have been discussed.

Chapter 2

Finite Element Modeling of Conventional Drill String

2.1 Overview

This chapter presents the development of a finite element model (*FEM*) of a conventional drill string. The development of the *FEM* model is guided by the work cited in references [10], [11] and [23-25]. The *FEM* model is a three-dimensional model based on Bernoulli-Euler beam theory, which accounts for simultaneous longitudinal, lateral, and torsional vibrations. In addition, the gyroscopic and gravitational stiffening effects of the drill string are considered in the *FEM* model.

Expressions for the drill string kinetic and strain energies are derived using the theory of finite element with appropriate interpolating functions. The developed energy expressions are utilized to determine the drill string element mass, gyroscopic and stiffness matrices. The equation of motion of the drill string is extracted by employing the Lagrange dynamics approach. The resulting equation of motion is exercised to predict the drill string modal parameters, band gap characteristics and Campbell diagram at different rotational speeds and design parameters.

Computational algorithm is developed using commercial software package such as *MATALB*® and validation of the performance of the developed *FEM* model is achieved by performing four different numerical simulations. Furthermore, the transfer matrix and the dispersion characteristics of the periodic drill string presented in chapter 3 are extracted utilizing the developed *FEM* model in order to validate the predictions of the band gap characteristics.

2.2 The Finite Element Model

The dynamics of the drill string are modeled using theory of finite element with a three-dimensional beam element based on Bernoulli-Euler beam theory. As displayed in Fig. 2.1(a), the *FEM* model divides the drill string into *N* finite beam elements.

2.2.1 Beam Element

Fig. 2.1(b) describes a three-dimensional beam element extending between two nodes. The bounding nodes connect the element to neighboring elements. Each node has six degrees of freedom defining its motions in the *x*-*y*, *x*-*z* and *y*-*z* planes. The six degrees of freedom consist of three translations (u, v, w) and three rotations $(\theta_x, \theta_y, \theta_z)$. The translations degrees of freedom are two transverse displacements in the *y* & *z* directions and one axial displacement in the *x* direction while the rotations degrees of freedom are two bending rotations about the *y* & *z* axes and one torsional rotation about the *x* axis. The rotations $\theta_y = \frac{\partial v}{\partial x}$ and $\theta_z = -\frac{\partial w}{\partial x}$ define the slope of deflection line with respect to *x* axis as implied by the Euler-Bernoulli material constraint that enforces the shear strains to vanish. Accordingly, the nodal deflection vector $\{\Delta^e(x)\}$ of the e^{th} element can be expressed as follows:

$$\{\Delta^e(x)\} = \begin{bmatrix} u & v & w & \theta_x & \theta_y & \theta_z \end{bmatrix}^T \tag{2.1}$$

The beam element has constant area moment of inertia *I*, modulus of elasticity *E* and length l_e. The beam element is subject to an axial compressive load *P* and a torque τ.

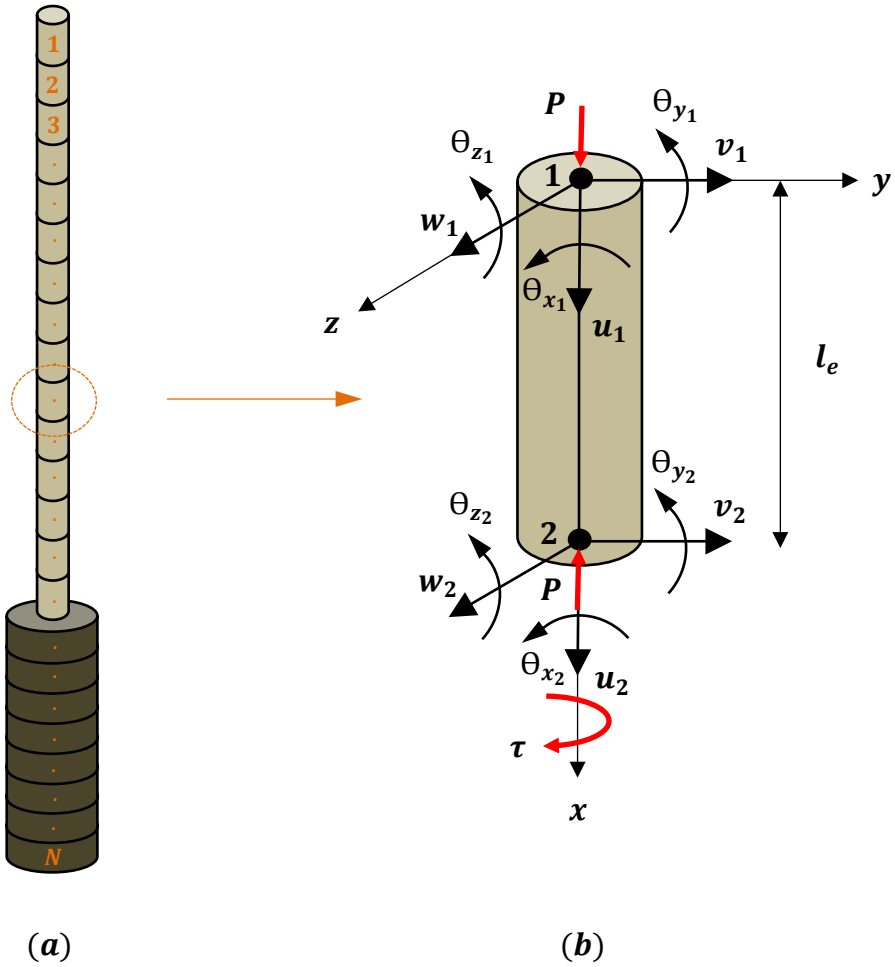

Fig. 2.1 Schematic drawing of finite element drill string, (a) Drill string finite element model and (b) Drill string element

2.2.2 Shape Functions

The displacements field can be expressed using the classical finite element cubic interpolating equation.

$$\{\Delta^e(x)\} = [N]\{\delta^e\} \tag{2.2}$$

where $[N]$ is the shape function matrix of the three dimensional finite element and $\{\delta^e\}$ is the element nodal displacement vector given as

$$\{\delta^e\} = \begin{bmatrix} u_1 & v_1 & w_1 & \theta_{x_1} & \theta_{y_1} & \theta_{z_1} & u_2 & v_2 & w_2 & \theta_{x_2} & \theta_{y_2} & \theta_{z_2} \end{bmatrix}^T \tag{2.3}$$

The translations and rotations deformations of an element can be expressed in terms of shape functions respectively as

$$\begin{Bmatrix} u(x) \\ v(x) \\ w(x) \end{Bmatrix} = [N_T]\{\delta^e\} \tag{2.4}$$

$$\begin{Bmatrix} \theta_y(x) \\ \theta_z(x) \end{Bmatrix} = [N_\theta]\{\delta^e\} \tag{2.5}$$

$$\{\theta_x(x)\} = [N_\varphi]\{\delta^e\} \tag{2.6}$$

where $[N_T]$, $[N_\theta]$ and $[N_\varphi]$ are the translation (axial and transverse), bending rotations and torsional rotation shape function matrices, respectively.

$$[N_T] = \begin{bmatrix} N_{u_1} & 0 & 0 & 0 & 0 & 0 & N_{u_2} & 0 & 0 & 0 & 0 & 0 \\ 0 & N_{v_1} & 0 & 0 & 0 & N_{v_2} & 0 & N_{v_3} & 0 & 0 & 0 & N_{v_4} \\ 0 & 0 & N_{v_1} & 0 & -N_{v_2} & 0 & 0 & 0 & N_{v_3} & 0 & -N_{v_4} & 0 \end{bmatrix} \tag{2.7}$$

$$[N_\theta] = \begin{bmatrix} 0 & N_{\theta_1} & 0 & 0 & 0 & N_{\theta_2} & 0 & N_{\theta_3} & 0 & 0 & 0 & N_{\theta_4} \\ 0 & 0 & -N_{\theta_1} & 0 & N_{\theta_2} & 0 & 0 & 0 & -N_{\theta_3} & 0 & N_{\theta_4} & 0 \end{bmatrix} \tag{2.8}$$

$$[N_\varphi] = [0 \quad 0 \quad 0 \quad N_{\varphi_1} \quad 0 \quad 0 \quad 0 \quad 0 \quad 0 \quad N_{\varphi_1} \quad 0 \quad 0] \tag{2.9}$$

The expressions of the linear shape functions with element coordinate $\xi = x/l_e$ are derived in [23] and [24] which are provided in Table 2.1 for the case without shear deformations.

Table 2.1 Element linear shape functions

$\boldsymbol{N_{u_1} = 1 - \xi}$	$\boldsymbol{N_{u_1} = \xi}$
$\boldsymbol{N_{v_1} = 1 - 3\xi^2 + 2\xi^3}$	$N_{v_2} = l_e(\xi - 2\xi^2 + \xi^3)$
$\boldsymbol{N_{v_3} = 3\xi^2 - 2\xi^3}$	$N_{v_4} = l_e(-\xi^2 + \xi^3)$
$\boldsymbol{N_{\theta_1} = \frac{6}{l_e}(-\xi + \xi^2)}$	$N_{\theta_2} = 1 - 4\xi + 3\xi^2$
$\boldsymbol{N_{\theta_3} = \frac{6}{l_e}(\xi - \xi^2)}$	$N_{\theta_4} = -2\xi + 3\xi^2$
$\boldsymbol{N_{\varphi_1} = 1 - \xi}$	$N_{\varphi_2} = \xi$

2.2.3 Element Kinetic Energy

The kinetic energy of an element due to translation and rotary inertias which includes the gyroscopic moment can be expressed as

$$KE = \frac{1}{2}\int_0^{l_e} (\mathbf{v}^T m\mathbf{v} + \boldsymbol{\omega}^T \mathbf{I}\boldsymbol{\omega})dx \tag{2.10}$$

where m is the mass per unit length, l_e is the length of the element, **v** is the velocity vector, **I** is the mass moment of inertia matrix and **ω** is the angular velocity vector

$$\mathbf{v} = \begin{bmatrix} \dot{u} \\ \dot{v} \\ \dot{w} \end{bmatrix},\ \mathbf{I} = \begin{bmatrix} I_p & 0 & 0 \\ 0 & I_c & 0 \\ 0 & 0 & I_c \end{bmatrix},\ \boldsymbol{\omega} = \begin{bmatrix} \dot{\theta}_x - \theta_y\dot{\theta}_z \\ \dot{\theta}_y\cos(\theta_x) - \dot{\theta}_z\sin(\theta_x) \\ \dot{\theta}_z\cos(\theta_x) + \dot{\theta}_y\sin(\theta_x) \end{bmatrix} \tag{2.11}$$

In Eq. (2.11), the time derivative (d/dt) is denoted by a superposed dot, I_c is cross sectional mass moment of inertia and I_p is polar mass moment of inertia $\left(I_p = 2I_c\right)$.

Eq. (2.10) can be simplified and expressed in a matrix form as

$$KE = \frac{1}{2}\{\dot{\delta}^e\}^T[M^e]\{\dot{\delta}^e\} + \Omega_x\{\dot{\delta}^e\}^T[G^e]\{\delta^e\} \tag{2.12}$$

where $\Omega_x = \dot{\theta}_x$ is the angular velocity along the *x*-axis of the drill string beam element and $[M^e] = [M_T^e] + [M_\theta^e] + [M_\varphi^e]$ is the augmented element mass matrix given by $[M_T^e]$ as the translational, $[M_\theta]$ as the rotary inertia and $[M_\varphi]$ as torsional mass matrices respectively.

The aforementioned element mass matrices are defined as

$$[M_T^e] = \int_0^{l_e} m[N_T]^T[N_T]\,dx \tag{2.13}$$

$$[M_\theta^e] = \int_0^{l_e} I_c[N_\theta]^T[N_\theta]\,dx \tag{2.14}$$

$$[M_\varphi^e] = \int_0^{l_e} I_p[N_\varphi]^T[N_\varphi]\,dx \tag{2.15}$$

while the element gyroscopic matrix $[G^e]$ is written as

$$[G^e] = \left[\int_0^{l_e} I_p[N_{\theta_y}]^T[N_{\theta_z}]dx\right] - \left[\int_0^{l_e} I_p[N_{\theta_y}]^T[N_{\theta_z}]dx\right]^T \tag{2.16}$$

where $[N_{\theta_y}]$ and $[N_{\theta_z}]$ are the first and second row of Eq. (2.8) respectively.

Expressions of the aforementioned element mass and gyroscopic matrices are provided in Tables 2.2 - 2.5.

Table 2.2 Element translation mass matrix

$$[M_T^e] = \frac{ml_e}{420}$$

$$\begin{bmatrix} 140 & 0 & 0 & 0 & 0 & 0 & 70 & 0 & 0 & 0 & 0 & 0 \\ 0 & 156 & 0 & 0 & 0 & 22l_e & 0 & 54 & 0 & 0 & 0 & -13l_e \\ 0 & 0 & 156 & 0 & -22l_e & 0 & 0 & 0 & 54 & 0 & 13l_e & 0 \\ 0 & 0 & 0 & 0 & 0 & 0 & 0 & 0 & 0 & 0 & 0 & 0 \\ 0 & 0 & -22l_e & 0 & 4l_e^2 & 0 & 0 & 0 & -13l_e & 0 & -3l_e^2 & 0 \\ 0 & 22l_e & 0 & 0 & 0 & 4l_e^2 & 0 & 13l_e & 0 & 0 & 0 & -3l_e^2 \\ 70 & 0 & 0 & 0 & 0 & 0 & 140 & 0 & 0 & 0 & 0 & 0 \\ 0 & 54 & 0 & 0 & 0 & 13l_e & 0 & 156 & 0 & 0 & 0 & -22l_e \\ 0 & 0 & 54 & 0 & -13l_e & 0 & 0 & 0 & 156 & 0 & 22l_e & 0 \\ 0 & 0 & 0 & 0 & 0 & 0 & 0 & 0 & 0 & 0 & 0 & 0 \\ 0 & 0 & 13l_e & 0 & -3l_e^2 & 0 & 0 & 0 & 22l_e & 0 & 4l_e^2 & 0 \\ 0 & -13l_e & 0 & 0 & 0 & -3l_e^2 & 0 & -22l_e & 0 & 0 & 0 & 4l_e^2 \end{bmatrix}$$

$$[M_T^e] = [M_T^e]^T$$

Table 2.3 Element rotary inertia mass matrix

$$[M_\theta^e] = \frac{I_c}{30l_e}$$

$$\begin{bmatrix} 0 & 0 & 0 & 0 & 0 & 0 & 0 & 0 & 0 & 0 & 0 & 0 \\ 0 & 36 & 0 & 0 & 0 & 3l_e & 0 & -36 & 0 & 0 & 0 & 3l_e \\ 0 & 0 & 36 & 0 & -3l_e & 0 & 0 & 0 & -36 & 0 & -3l_e & 0 \\ 0 & 0 & 0 & 0 & 0 & 0 & 0 & 0 & 0 & 0 & 0 & 0 \\ 0 & 0 & -3l_e & 0 & 4l_e^2 & 0 & 0 & 0 & 3l_e & 0 & -l_e^2 & 0 \\ 0 & 3l_e & 0 & 0 & 0 & 4l_e^2 & 0 & -3l_e & 0 & 0 & 0 & -l_e^2 \\ 0 & 0 & 0 & 0 & 0 & 0 & 0 & 0 & 0 & 0 & 0 & 0 \\ 0 & -36 & 0 & 0 & 0 & -3l_e & 0 & 36 & 0 & 0 & 0 & -3l_e \\ 0 & 0 & -36 & 0 & 3l_e & 0 & 0 & 0 & 36 & 0 & 3l_e & 0 \\ 0 & 0 & 0 & 0 & 0 & 0 & 0 & 0 & 0 & 0 & 0 & 0 \\ 0 & 0 & -3l_e & 0 & -l_e^2 & 0 & 0 & 0 & 3l_e & 0 & 4l_e^2 & 0 \\ 0 & 3l_e & 0 & 0 & 0 & -l_e^2 & 0 & -3l_e & 0 & 0 & 0 & 4l_e^2 \end{bmatrix}$$

$$[M_\theta^e] = [M_\theta^e]^T$$

Table 2.4 Element torsional mass matrix

$$[\boldsymbol{M}_{\boldsymbol{\varphi}}^{\boldsymbol{e}}] = \frac{\boldsymbol{I_p l_e}}{\boldsymbol{6}}$$

$$\begin{bmatrix} 0 & 0 & 0 & 0 & 0 & 0 & 0 & 0 & 0 & 0 & 0 & 0 \\ 0 & 0 & 0 & 0 & 0 & 0 & 0 & 0 & 0 & 0 & 0 & 0 \\ 0 & 0 & 0 & 0 & 0 & 0 & 0 & 0 & 0 & 0 & 0 & 0 \\ 0 & 0 & 0 & 2 & 0 & 0 & 0 & 0 & 0 & 1 & 0 & 0 \\ 0 & 0 & 0 & 0 & 0 & 0 & 0 & 0 & 0 & 0 & 0 & 0 \\ 0 & 0 & 0 & 0 & 0 & 0 & 0 & 0 & 0 & 0 & 0 & 0 \\ 0 & 0 & 0 & 0 & 0 & 0 & 0 & 0 & 0 & 0 & 0 & 0 \\ 0 & 0 & 0 & 0 & 0 & 0 & 0 & 0 & 0 & 0 & 0 & 0 \\ 0 & 0 & 0 & 0 & 0 & 0 & 0 & 0 & 0 & 0 & 0 & 0 \\ 0 & 0 & 0 & 1 & 0 & 0 & 0 & 0 & 0 & 2 & 0 & 0 \\ 0 & 0 & 0 & 0 & 0 & 0 & 0 & 0 & 0 & 0 & 0 & 0 \\ 0 & 0 & 0 & 0 & 0 & 0 & 0 & 0 & 0 & 0 & 0 & 0 \end{bmatrix}$$

$$[M_{\varphi}^{e}] = [M_{\varphi}^{e}]^{T}$$

Table 2.5 Element gyroscopic mass matrix

$$[G^e] = \frac{I_p}{30 l_e}$$

$$\begin{bmatrix} 0 & 0 & 0 & 0 & 0 & 0 & 0 & 0 & 0 & 0 & 0 & 0 \\ 0 & 0 & -36 & 0 & 3l_e & 0 & 0 & 0 & 36 & 0 & 3l_e & 0 \\ 0 & 36 & 0 & 0 & 0 & 3l_e & 0 & -36 & 0 & 0 & 0 & 3l_e \\ 0 & 0 & 0 & 0 & 0 & 0 & 0 & 0 & 0 & 0 & 0 & 0 \\ 0 & -3l_e & 0 & 0 & 0 & -4l_e^2 & 0 & 3l_e & 0 & 0 & 0 & l_e^2 \\ 0 & 0 & -3l_e & 0 & 4l_e^2 & 0 & 0 & 0 & 3l_e & 0 & -l_e^2 & 0 \\ 0 & 0 & 0 & 0 & 0 & 0 & 0 & 0 & 0 & 0 & 0 & 0 \\ 0 & 0 & 36 & 0 & -3l_e & 0 & 0 & 0 & -36 & 0 & -3l_e & 0 \\ 0 & -36 & 0 & 0 & 0 & -3l_e & 0 & 36 & 0 & 0 & 0 & -3l_e \\ 0 & 0 & 0 & 0 & 0 & 0 & 0 & 0 & 0 & 0 & 0 & 0 \\ 0 & -3l_e & 0 & 0 & 0 & l_e^2 & 0 & 3l_e & 0 & 0 & 0 & -4l_e^2 \\ 0 & 0 & -3l_e & 0 & -l_e^2 & 0 & 0 & 0 & 3l_e & 0 & 4l_e^2 & 0 \end{bmatrix}$$

$$[G^e] = -[G^e]^T$$

2.2.4 Element Strain Energy

The strain energy of an element is given by

$$U = \frac{1}{2}\int_V \{\varepsilon\}^T\{\sigma\}dV \tag{2.17}$$

where ε and σ denote the strain and stress respectively.

The relationship between the stress σ and ε strain for linearly elastic material is defined as

$$\{\sigma\} = [E]\{\varepsilon\} \tag{2.18}$$

where E is the modulus of elasticity.

Substituting Eq. (2.18) into Eq. (2.17) yields

$$U = \frac{1}{2}\int_V \{\varepsilon\}^T[E]\{\varepsilon\}dV \tag{2.19}$$

The elastic strain energy due to axial, torsional and bending deformations respectively is expressed as

$$U_a = \frac{1}{2}\int_0^{l_e} EA\left(\frac{\partial u}{\partial x}\right)^2 dx \tag{2.20}$$

$$U_\varphi = \frac{1}{2}\int_0^{l_e} GJ\left(\frac{\partial \theta_x}{\partial x}\right)^2 dx \tag{2.21}$$

$$U_b = \frac{1}{2}\int_0^{l_e} EI_y\left(\frac{\partial \theta_y}{\partial x}\right)^2 dx + \frac{1}{2}\int_0^{l_e} EI_z\left(\frac{\partial \theta_z}{\partial x}\right)^2 dx \tag{2.22}$$

where A is the cross sectional area, G is the shear modulus, I_y and I_z are the area of moment of inertia around the *y* & *z* axes and J polar area moment of inertia.

Due to cross section symmetry $I_y = I_z = I$, Eq. (2.22) can be simplified as

$$U_b = \frac{1}{2}\int_0^{l_e} EI\left\{\left(\frac{\partial\theta_y}{\partial x}\right)^2 + \left(\frac{\partial\theta_z}{\partial x}\right)^2\right\}dx \tag{2.23}$$

Also, the geometric stiffening strain energy due to gravitational field is given by

$$U_g = \frac{1}{2}\int_0^{l_e} F_g(x)\left\{\left(\frac{\partial v}{\partial x}\right)^2 + \left(\frac{\partial w}{\partial x}\right)^2\right\}dx \tag{2.24}$$

where $F_g(x)$ is gravitational force acting along the axis of the drill string element.

Hence, the total element strain energy becomes

$$U = U_a + U_\varphi + U_b + U_g$$

$$\begin{aligned} U = {} & \frac{1}{2}\int_0^{l_e} EA\left(\frac{\partial u}{\partial x}\right)^2 dx + \frac{1}{2}\int_0^{l_e} GJ\left(\frac{\partial\theta_x}{\partial x}\right)^2 dx \\ & + \frac{1}{2}\int_0^{l_e} EI\left\{\left(\frac{\partial\theta_y}{\partial x}\right)^2 + \left(\frac{\partial\theta_z}{\partial x}\right)^2\right\}dx \\ & + \frac{1}{2}\int_0^{l_e} F_g(x)\left\{\left(\frac{\partial v}{\partial x}\right)^2 + \left(\frac{\partial w}{\partial x}\right)^2\right\}dx \end{aligned} \tag{2.25}$$

In a compact matrix form, Eq. (2.25) can be written as

$$U = \frac{1}{2}\{\delta^e\}^T[K^e]\{\delta^e\} \tag{2.26}$$

where $[K^e] = [K_a^e] + [K_\varphi^e] + [K_b^e] + [K_g^e]$ is the augmented element stiffness matrix given by $[K_a^e]$ as the axial, $[K_\varphi^e]$ as torsional, $[K_b^e]$ as bending and $[K_g^e]$ as geometric stiffness matrices respectively.

The aforementioned element stiffness matrices are defined as

$$[K_a^e] = \int_0^{l_e} EA \frac{\partial [N_u]^T}{\partial x} \frac{\partial [N_u]}{\partial x} dx \tag{2.27}$$

$$[K_\varphi^e] = \int_0^{l_e} GJ \frac{\partial [N_\varphi]^T}{\partial x} \frac{\partial [N_\varphi]}{\partial x} dx \tag{2.28}$$

$$[K_b^e] = \int_0^{l_e} EI \left\{ \frac{\partial \left[N_{\theta_y}\right]^T}{\partial x} \frac{\partial \left[N_{\theta_y}\right]}{\partial x} + \frac{\partial \left[N_{\theta_z}\right]^T}{\partial x} \frac{\partial \left[N_{\theta_z}\right]}{\partial x} \right\} dx \tag{2.29}$$

$$[K_g^e] = \int_0^{l_e} F_g(x) \left\{ \frac{\partial [N_v]^T}{\partial x} \frac{\partial [N_v]}{\partial x} + \frac{\partial [N_w]^T}{\partial x} \frac{\partial [N_w]}{\partial x} \right\} dx \tag{2.30}$$

where $[N_u]$, $[N_v]$ and $[N_w]$ are the first, second and third row of Eq. (2.7) respectively.

The neutral point is defined as the point having zero longitudinal force which separates the tension (drill pipes) and compression (drill collars) fields of the drill string. Therefore, the gravitational force $F_g(x)$ in Eq. (2.30) is expressed by [11] in the tension and compression fields respectively as

$$F_{g_t}(x) = -\rho g A[L_t + (l_e - x)] \tag{2.31}$$

$$F_{g_c}(x) = \rho g A[L_c + x] \tag{2.32}$$

where ρ is the density, g is the gravitational acceleration constant, L_t is the sum of elements length under tension and L_c is the sum of elements length under compression. Fig. 2.2 illustrates the drill string longitudinal force distribution.

Substituting Eqs. (2.31) and (2.32) into Eq. (2.30), the geometric stiffness matrices for elements in the tension and compression fields, respectively can be written as

$$[K_{g_t}^e] = \int_0^{l_e} -\rho g A[L_t + (l_e - x)] \left\{ \frac{\partial [N_v]^T}{\partial x} \frac{\partial [N_v]}{\partial x} + \frac{\partial [N_w]^T}{\partial x} \frac{\partial [N_w]}{\partial x} \right\} dx \qquad (2.33)$$

$$[K_{g_c}^e] = \int_0^{l_e} \rho g A[L_c + x] \left\{ \frac{\partial [N_v]^T}{\partial x} \frac{\partial [N_v]}{\partial x} + \frac{\partial [N_w]^T}{\partial x} \frac{\partial [N_w]}{\partial x} \right\} dx \qquad (2.34)$$

Expressions of the aforementioned element stiffness matrices are given in Tables 2.6 - 2.10.

Table 2.6 Element axial stiffness matrix

$$[K_a^e] = \frac{EA}{l_e} \begin{bmatrix} 1 & 0 & 0 & 0 & 0 & 0 & -1 & 0 & 0 & 0 & 0 & 0 \\ 0 & 0 & 0 & 0 & 0 & 0 & 0 & 0 & 0 & 0 & 0 & 0 \\ 0 & 0 & 0 & 0 & 0 & 0 & 0 & 0 & 0 & 0 & 0 & 0 \\ 0 & 0 & 0 & 0 & 0 & 0 & 0 & 0 & 0 & 0 & 0 & 0 \\ 0 & 0 & 0 & 0 & 0 & 0 & 0 & 0 & 0 & 0 & 0 & 0 \\ 0 & 0 & 0 & 0 & 0 & 0 & 0 & 0 & 0 & 0 & 0 & 0 \\ -1 & 0 & 0 & 0 & 0 & 0 & 1 & 0 & 0 & 0 & 0 & 0 \\ 0 & 0 & 0 & 0 & 0 & 0 & 0 & 0 & 0 & 0 & 0 & 0 \\ 0 & 0 & 0 & 0 & 0 & 0 & 0 & 0 & 0 & 0 & 0 & 0 \\ 0 & 0 & 0 & 0 & 0 & 0 & 0 & 0 & 0 & 0 & 0 & 0 \\ 0 & 0 & 0 & 0 & 0 & 0 & 0 & 0 & 0 & 0 & 0 & 0 \\ 0 & 0 & 0 & 0 & 0 & 0 & 0 & 0 & 0 & 0 & 0 & 0 \end{bmatrix}$$

$$[K_a^e] = [K_a^e]^T$$

Table 2.7 Element torsional stiffness matrix

$$[K_{\varphi}^{e}] = \frac{GJ}{l_e}\begin{bmatrix} 0 & 0 & 0 & 0 & 0 & 0 & 0 & 0 & 0 & 0 & 0 & 0 \\ 0 & 0 & 0 & 0 & 0 & 0 & 0 & 0 & 0 & 0 & 0 & 0 \\ 0 & 0 & 0 & 0 & 0 & 0 & 0 & 0 & 0 & 0 & 0 & 0 \\ 0 & 0 & 0 & 1 & 0 & 0 & 0 & 0 & 0 & -1 & 0 & 0 \\ 0 & 0 & 0 & 0 & 0 & 0 & 0 & 0 & 0 & 0 & 0 & 0 \\ 0 & 0 & 0 & 0 & 0 & 0 & 0 & 0 & 0 & 0 & 0 & 0 \\ 0 & 0 & 0 & 0 & 0 & 0 & 0 & 0 & 0 & 0 & 0 & 0 \\ 0 & 0 & 0 & 0 & 0 & 0 & 0 & 0 & 0 & 0 & 0 & 0 \\ 0 & 0 & 0 & 0 & 0 & 0 & 0 & 0 & 0 & 0 & 0 & 0 \\ 0 & 0 & 0 & -1 & 0 & 0 & 0 & 0 & 0 & 1 & 0 & 0 \\ 0 & 0 & 0 & 0 & 0 & 0 & 0 & 0 & 0 & 0 & 0 & 0 \\ 0 & 0 & 0 & 0 & 0 & 0 & 0 & 0 & 0 & 0 & 0 & 0 \end{bmatrix}$$

$$[K_{\varphi}^{e}] = [K_{\varphi}^{e}]^{T}$$

Table 2.8 Element bending stiffness matrix

$$[K_{b}^{e}] = \frac{EI}{l_e^3}$$

$$\begin{bmatrix} 0 & 0 & 0 & 0 & 0 & 0 & 0 & 0 & 0 & 0 & 0 & 0 \\ 0 & 12 & 0 & 0 & 0 & 6l_e & 0 & -12 & 0 & 0 & 0 & 6l_e \\ 0 & 0 & 12 & 0 & -6l_e & 0 & 0 & 0 & -12 & 0 & -6l_e & 0 \\ 0 & 0 & 0 & 0 & 0 & 0 & 0 & 0 & 0 & 0 & 0 & 0 \\ 0 & 0 & -6l_e & 0 & 4l_e^2 & 0 & 0 & 0 & 6l_e & 0 & 2l_e^2 & 0 \\ 0 & 6l_e & 0 & 0 & 0 & 4l_e^2 & 0 & -6l_e & 0 & 0 & 0 & 2l_e^2 \\ 0 & 0 & 0 & 0 & 0 & 0 & 0 & 0 & 0 & 0 & 0 & 0 \\ 0 & -12 & 0 & 0 & 0 & -6l_e & 0 & 12 & 0 & 0 & 0 & -6l_e \\ 0 & 0 & -12 & 0 & 6l_e & 0 & 0 & 0 & 12 & 0 & 6l_e & 0 \\ 0 & 0 & 0 & 0 & 0 & 0 & 0 & 0 & 0 & 0 & 0 & 0 \\ 0 & 0 & -6l_e & 0 & 2l_e^2 & 0 & 0 & 0 & 6l_e & 0 & 4l_e^2 & 0 \\ 0 & 6l_e & 0 & 0 & 0 & 2l_e^2 & 0 & -6l_e & 0 & 0 & 0 & 4l_e^2 \end{bmatrix}$$

$$[K_{b}^{e}] = [K_{b}^{e}]^{T}$$

Table 2.9 Element geometric stiffness matrix for tension field

$$\left[K_{g_t}^e\right] = \frac{\rho g A}{60}$$

$$\begin{bmatrix}
0 & 0 & 0 & 0 & 0 & 0 & 0 & 0 & 0 & 0 & 0 & 0 \\
0 & 36t_1 & 0 & 0 & 0 & 6L_t & 0 & -36t_1 & 0 & 0 & 0 & 6t_3 \\
0 & 0 & 36t_1 & 0 & -6L_t & 0 & 0 & 0 & -36t_1 & 0 & -6t_3 & 0 \\
0 & 0 & 0 & 0 & 0 & 0 & 0 & 0 & 0 & 0 & 0 & 0 \\
0 & 0 & -6L_t & 0 & 2l_e t_4 & 0 & 0 & 0 & 6L_t & 0 & -l_e t_2 & 0 \\
0 & 6L_t & 0 & 0 & 0 & 2l_e t_4 & 0 & -6L_t & 0 & 0 & 0 & -l_e t_2 \\
0 & 0 & 0 & 0 & 0 & 0 & 0 & 0 & 0 & 0 & 0 & 0 \\
0 & -36t_1 & 0 & 0 & 0 & -6L_t & 0 & 36t_1 & 0 & 0 & 0 & -6t_3 \\
0 & 0 & -36t_1 & 0 & 6L_t & 0 & 0 & 0 & 36t_1 & 0 & 6t_3 & 0 \\
0 & 0 & 0 & 0 & 0 & 0 & 0 & 0 & 0 & 0 & 0 & 0 \\
0 & 0 & -6t_3 & 0 & -l_e t_2 & 0 & 0 & 0 & 6t_3 & 0 & 2l_e t_5 & 0 \\
0 & 6t_3 & 0 & 0 & 0 & -l_e t_2 & 0 & -6t_3 & 0 & 0 & 0 & 2l_e t_5
\end{bmatrix}$$

$t_1 = t_2/l_e$ $\quad$ $t_2 = (2L_t + l_e)$ $\quad$ $t_3 = (L_t + l_e)$

$t_4 = (4L_t + 3l_e)$ $\quad$ $t_5 = (4L_t + l_e)$

$$\left[K_{g_t}^e\right] = \left[K_{g_t}^e\right]^T$$

Table 2.10 Element geometric stiffness matrix for compression field

$$\left[K_{g_c}^{e}\right] = \frac{\rho g A}{60}$$

$$\begin{bmatrix}
0 & 0 & 0 & 0 & 0 & 0 & 0 & 0 & 0 & 0 & 0 & 0 \\
0 & 36c_1 & 0 & 0 & 0 & 6c_3 & 0 & -36c_1 & 0 & 0 & 0 & 6L_c \\
0 & 0 & 36c_1 & 0 & -6c_3 & 0 & 0 & 0 & -36c_1 & 0 & -6L_c & 0 \\
0 & 0 & 0 & 0 & 0 & 0 & 0 & 0 & 0 & 0 & 0 & 0 \\
0 & 0 & -6c_3 & 0 & 2l_e c_4 & 0 & 0 & 0 & 6c_3 & 0 & -l_e c_2 & 0 \\
0 & 6c_3 & 0 & 0 & 0 & 2l_e c_4 & 0 & -6c_3 & 0 & 0 & 0 & -l_e c_2 \\
0 & 0 & 0 & 0 & 0 & 0 & 0 & 0 & 0 & 0 & 0 & 0 \\
0 & -36c_1 & 0 & 0 & 0 & -6c_3 & 0 & 36c_1 & 0 & 0 & 0 & -6L_c \\
0 & 0 & -36c_1 & 0 & 6c_3 & 0 & 0 & 0 & 36c_1 & 0 & 6L_c & 0 \\
0 & 0 & 0 & 0 & 0 & 0 & 0 & 0 & 0 & 0 & 0 & 0 \\
0 & 0 & -6L_c & 0 & -l_e c_2 & 0 & 0 & 0 & 6L_c & 0 & 2l_e c_5 & 0 \\
0 & 6L_c & 0 & 0 & 0 & -l_e c_2 & 0 & -6L_c & 0 & 0 & 0 & 2l_e c_5
\end{bmatrix}$$

$c_1 = c_2/l_e$ $\quad$ $c_2 = (2L_c + l_e)$ $\quad$ $c_3 = (L_c + l_e)$

$c_4 = (4L_c + l_e)$ $\quad$ $c_5 = (4L_c + 3l_e)$

$$\left[K_{g_c}^{e}\right] = \left[K_{g_c}^{e}\right]^T$$

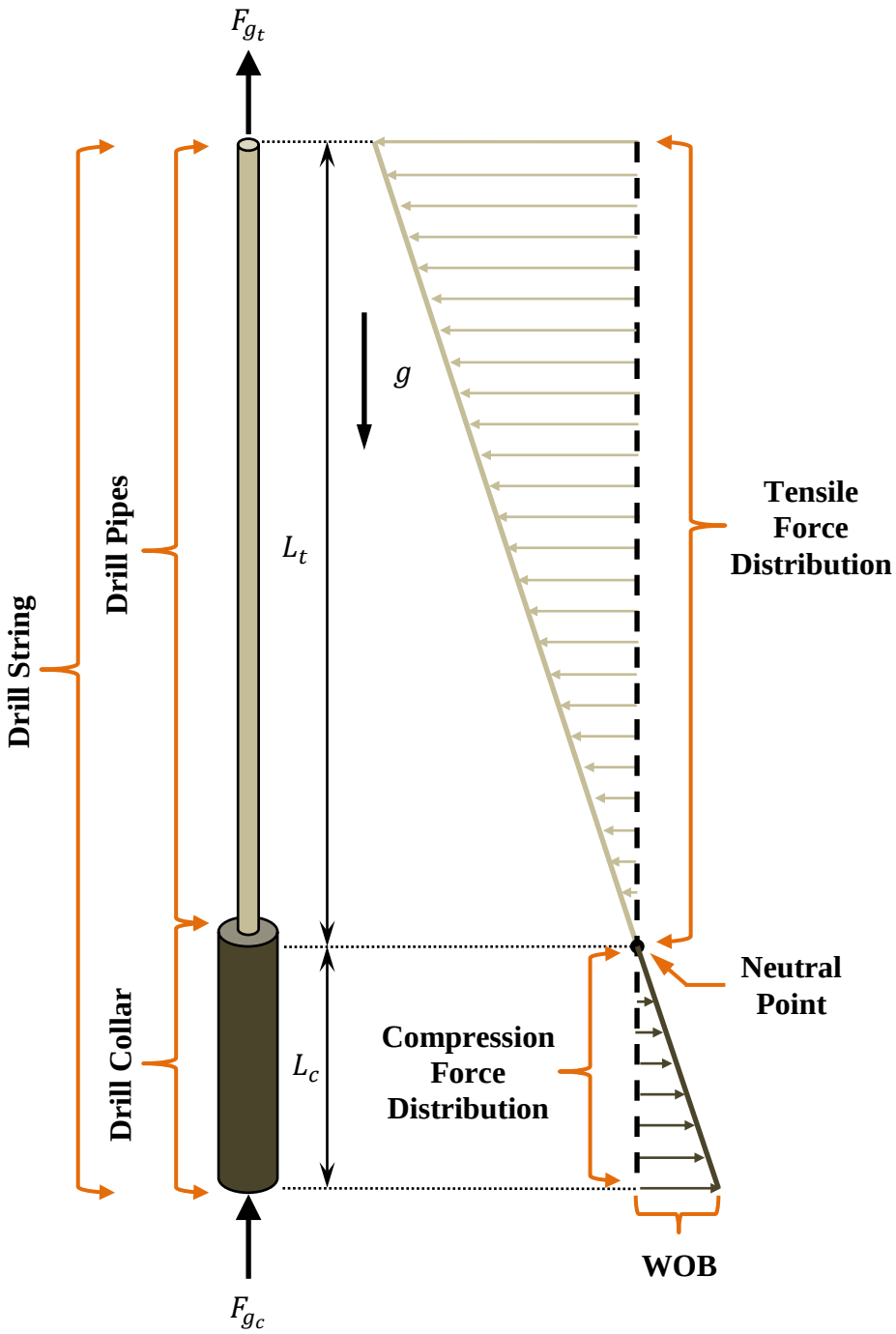

Fig. 2.2 Drill string longitudinal force distribution

2.2.5 Element Equation of Motion

Let $\boldsymbol{L}$ denotes the Lagrangian of the drill string beam element, then $\boldsymbol{L}$ is defined as

$$\boldsymbol{L} = KE - U \tag{2.35}$$

The equation of motion of the drill string beam element is given by

$$\frac{d}{dt}\left(\frac{\partial \boldsymbol{L}}{\partial\{\dot{\delta}^e\}}\right) - \frac{\partial \boldsymbol{L}}{\partial\{\delta^e\}} = \{Q^e\} \tag{2.36}$$

where $\{Q^e\}$ is the vector of generalized forces acting on the beam element such as external loads and moments.

Substituting Eqs. (2.12), (2.26) and (2.35) into Eq. (2.36), the element Eq. of motion becomes

$$[M^e]\{\ddot{\delta}^e\} + \Omega_x[G^e]\{\dot{\delta}^e\} + [K^e]\{\delta^e\} = \{Q^e\} \tag{2.37}$$

2.2.6 Element Matrices Assembly

Assembly of the mass, gyroscopic and stiffness matrices of the individual beam elements aims at forming the global matrices of the entire undamped drill string. During such a process, the compatibility of the deflections of the neighboring elements at the common nodes connecting them must be ensured. In addition, the equilibrium conditions of the forces and moments acting at the nodes must be guaranteed.

Let the vector of nodal deflections of the entire drill string be

$$\{\delta\} = \left[u_1\ v_1\ w_1\ \theta_{x_1}\ \theta_{y_1}\ \theta_{z_1}\ u_2\ v_2\ w_2\ \theta_{x_2}\ \theta_{y_2}\ \theta_{z_2} \ldots u_N\ \ v_N\ \ w_N\ \ \theta_{x_N}\ \ \theta_{y_N}\ \ \theta_{z_N}\right]^T$$

with N denoting number of nodal points. Then, the compatibility and equilibrium conditions require that

$$\sum_{e=1}^{n}[M^e]\{\ddot{\delta}^e\}+\sum_{e=1}^{n}\Omega_x[G^e]\{\dot{\delta}^e\}+\sum_{e=1}^{n}[K^e]\{\delta^e\}=\sum_{e=1}^{n}\{Q^e\} \tag{2.38}$$

Thus, the global drill string system equation of motion can be expressed as

$$[M]\{\ddot{\delta}\}+\Omega_x[G]\{\dot{\delta}\}+[K]\{\delta\}=\{Q\} \tag{2.39}$$

where n is the number of elements and $\{Q\}$ is the vector of global forces and moments acting on the drill string. Also $[M]$, $[G]$ and $[K]$ are the global mass, gyroscopic and stiffness matrices of the drill string respectively. One should note that the global mass $[M]$ and stiffness $[K]$ matrices are symmetric while the gyroscopic $[G]$ matrix is a skew symmetric. The assembled matrices are given by

$$[M] = \begin{bmatrix} [M^{e_1}] & & 0 \\ & [M^{e_2}] & \\ & & \ddots \\ 0 & & [M^{e_N}] \end{bmatrix} \tag{2.40}$$

$$[G] = \begin{bmatrix} [G^{e_1}] & & 0 \\ & [G^{e_2}] & \\ & & \ddots \\ 0 & & [G^{e_N}] \end{bmatrix} \tag{2.41}$$

$$[K] = \begin{bmatrix} [K^{e_1}] & & 0 \\ & [K^{e_2}] & \\ & & \ddots \\ 0 & & [K^{e_N}] \end{bmatrix} \tag{2.42}$$

2.2.7 Boundary Conditions

The final equation of motion of the rotating drill string is obtained by imposing the boundary conditions on Eq. (2.39). This is achieved by eliminating the columns and rows of the mass, gyroscopic and stiffness matrices corresponding to any restrained degree of freedom [24]. The resulting equation of motion becomes

$$[M_o]\{\ddot{\delta}_o\} + \Omega_x[G_o]\{\dot{\delta}_o\} + [K_o]\{\delta_o\} = \{Q_o\} \tag{2.43}$$

where $[M_o]$, $[G_o]$ and $[K_o]$ are the overall mass, gyroscopic and stiffness matrices. In addition, $\{\delta_o\}$ and $\{Q_o\}$ denote the overall deflection vector of unrestrained degrees of freedom and the corresponding loads and moments vector.

2.3 Model Verification

Based on the presented *FEM* formulations, a computational algorithm is developed using commercial software package such as *MATALB*®. Fig. 2.3 describes the flow chart of the developed *MATALB*® program.

2.3.1 Model Analysis

Let $\{\mathrm{X}\}$ and $\{F\}$ denote the state and force vectors, respectively and are defined as

$$\{\mathrm{X}\} = \begin{Bmatrix}\{\delta_o\} \\ \{\dot{\delta_o}\}\end{Bmatrix} \quad \& \quad \{F\} = \begin{Bmatrix}\{0\} \\ \{Q_o\}\end{Bmatrix} \tag{2.44}$$

Then, Eq. (2.43) can be represented in a state space [25] form such as

$$[M^*]\{\dot{\mathrm{X}}\} + [G^*]\{\mathrm{X}\} = \{F\} \tag{2.45}$$

where $[M^*]$ and $[G^*]$ are symmetric coefficient matrices given by

$$[M^*] = \begin{bmatrix}[K_o] & [0] \\ [0] & [M_o]\end{bmatrix} \quad \& \quad [G^*] = \begin{bmatrix}[0] & -[K_o] \\ [K_o] & \Omega_x[G_o]\end{bmatrix} \tag{2.46}$$

Matrices $[M_o]$, $[G_o]$ and $[K_o]$ have dimensions $(6n \times 6n)$ while matrices $[M^*]$ and $[G^*]$ have dimensions $(12n \times 12n)$ where n is the number of nodes.

The vibration characteristics of the drill string, namely, the natural frequencies and mode shapes can be obtained by reducing Eq. (2.45) to its corresponding

eigenvalue problem for the case of free vibrations with $\{F\} = 0$. Thus, Eq. (2.45) becomes

$$[D]\{\psi\} = \omega_n^2\{\psi\} \tag{2.47}$$

where ω_n and $\{\psi\}$ are the drill string eigenvalues (natural frequencies) and the eigenvectors (mode shapes), respectively. The matrix $[D]$ is given by

$$[D] = \left[[M^*]^{-1}[K^*]\right] \tag{2.48}$$

where $[K^*] = [G^*]^T[M^*]^{-1}[G^*]$ is a symmetric matrix [39].

For a non-rotating drill string ($\Omega_x = 0$), Eq. (2.43) reduces to its corresponding standard eigenvalue problem for the case of free vibrations with $\{Q_o\} = 0$ as

$$[\overline{D}]\{\psi\} = \omega_n^2\{\psi\} \tag{2.49}$$

where $[\overline{D}]$ is given by

$$[\overline{D}] = [M_o]^{-1}[K_o] \tag{2.50}$$

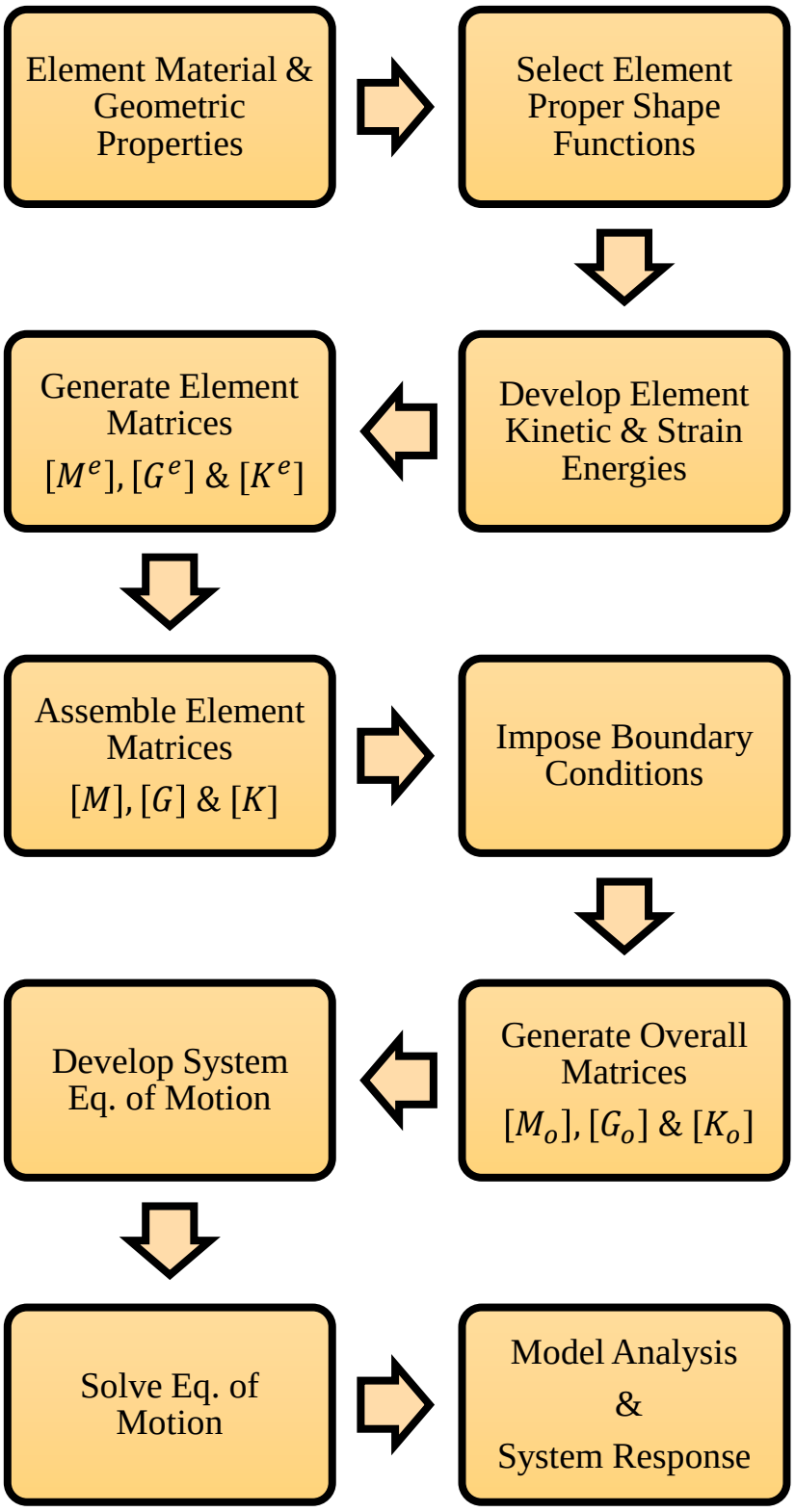

Fig. 2.3 *MATALB*® program flow chart

2.3.2 Numerical Simulations

To examine the capabilities of the developed computational algorithm on performing modal analysis of 3D-beam type structures, four numerical simulations are considered.

2.3.2.1 Simulation (A)

The effect of number of elements on the natural frequencies of a cantilever beam is investigated in this simulation. The cantilever beam example schematic drawing and specifications are displayed in Figure 2.4 and Table 2.11 respectively.

Table 2.11 Cantilever beam specifications

Geometric Properties	**Value**
Beam length, ***L***	1492 *mm*
Beam Diameter, ***D***	6.35 *mm*
Material Properties	
Mass density, $\boldsymbol{\rho}$	8000 kg/m^3
Modulus of Elasticity, ***E***	193 *GPa*

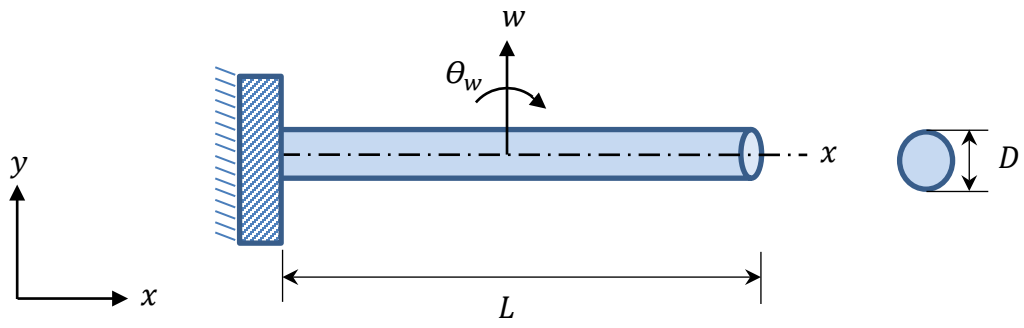

Fig. 2.4 Schematic drawing of cantilever beam

The cantilever beam is discretized into "*n*" number of elements where "*n*" is varied between 1 and 14. Each element has two degrees of freedom at each node which comprises of a transverse displacement (w) in the *y*-direction and a bending rotation (θ_w) about the *y*-axis. The beam model natural frequencies are determined using the developed *MATALB*® program. The obtained results are compared with the exact solution outlined, for example, in [26]. A summary of the obtained results is provided in Table 2.12.

In the exact solution, the natural frequencies are given by

$$\omega_n = \mu^2\sqrt{EI/mL^4} \tag{2.51}$$

where μ = 1.875, 4.694, 7.855 and 10.996, for $n = 1\ to\ 4$. For $n > 4$, $\mu = (2n-1)\pi/2$.

Table 2.12 shows that increasing the number of finite elements, used to model the beam dynamics makes the natural frequencies of the models converge monotonically to the exact solutions. In addition, the predictions of the *FEM* are always higher than the exact solutions. However, the difference between the predicted and the exact frequencies decreases as the number of elements increases. Such a difference is relatively large for higher order modes and is much smaller for the low order modes. These statements are emphasized by considering the plots shown in Figure 2.5.

It is also evident that if one is to accurately predict the first mode only, then one finite beam element is more than adequate. Hence, it is essential to use the lowest order of *FEM*, which can accurately predict the beam dynamics over the frequency range of

interest. Higher order models will unnecessarily complicate the design of the appropriate controllers.

Table 2.12 Effect of number of elements on natural frequencies (*Hz*)

Mode	Infinite	Number of Elements							
	(Exact)	14	12	10	8	6	4	2	1
1	1.96	1.96	1.96	1.96	1.96	1.96	1.96	1.96	1.97
2	12.28	12.28	12.28	12.28	12.28	12.28	12.29	12.38	19.40
3	34.39	34.39	34.39	34.39	34.40	34.44	34.65	41.88	
4	67.38	67.39	67.40	67.44	67.52	67.81	68.35	121.54	
5	111.38	111.44	111.51	111.65	112.01	113.04	127.12		
6	166.38	166.60	166.80	167.25	168.33	169.12	204.14		
7	232.39	232.99	233.52	234.64	236.94	260.76	323.60		
8	309.39	310.82	311.99	314.33	314.75	358.12	530.73		
9	397.39	400.37	402.66	406.39	442.48	489.32			
10	496.40	502.04	505.94	505.15	561.18	661.78			

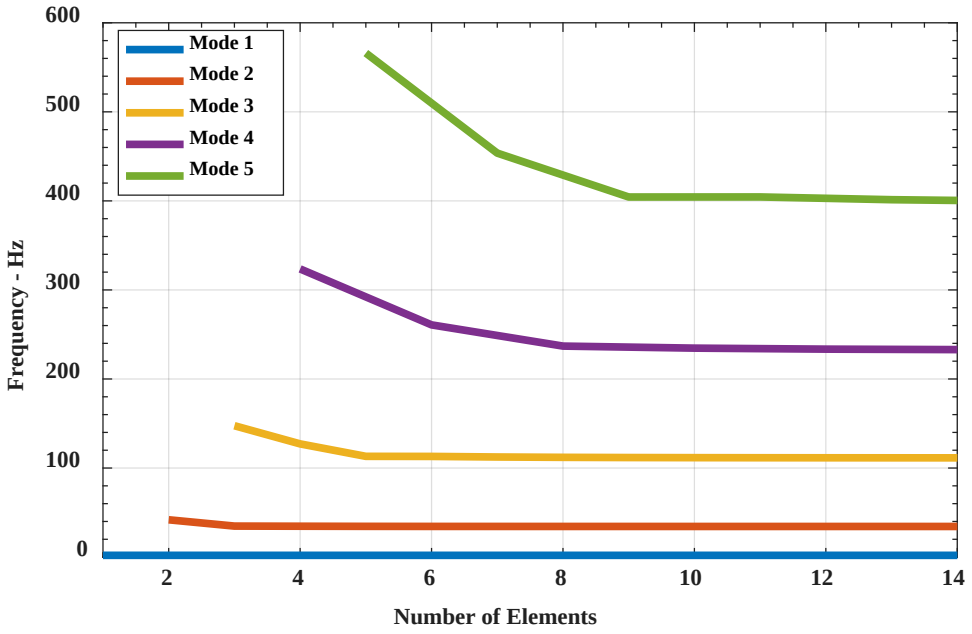

Fig. 2.5 Effect of number of elements on convergence of natural frequencies

2.3.2.2 Simulation (B)

The effect of gravity load on the natural frequencies of a suspended beam is studied in this simulation. The example of free vibration characteristics of vertically hanging uniform beam under the influence of gravity in [27] is adopted. The numerical data of the beam is provided in Table 2.13. The hanging cantilever beam is discretized with 20 elements of equal length. Each element has two degrees of freedom at each node, which comprises of a transverse displacement (w) in the y-direction and a bending rotation (θ_w) about the y-axis. Figure 2.6 is a schematic drawing of the vertically hanging cantilever beam. The first ten bending natural frequencies of the beam are computed using the developed algorithm and compared to the results of [27] in Table 2.14.

Table 2.13 Hanging cantilever beam specifications [27]

Geometric Properties	**Value**	
Beam length, L	2.9	m
Beam width, b	0.1	m
Beam thickness, t	0.001	m
Material Properties		
Mass density, ρ	8000	kg/m^3
Poisson's ratio, ν	0.3	
Young's Modulus, E	175.6	GPa
Number of Elements	20	

Table 2.14 Bending natural frequencies of hanging cantilever beam (*Hz*)

Mode	[27]		**Alsaffar**	
	Exact (w/o gravity)	**FEM (w. gravity)**	**FEM (w/o gravity)**	**FEM (w. gravity)**
1	0.09	0.37	0.089	0.373
2	0.56	1.02	0.564	1.020
3	1.58	2.14	1.579	2.136
4	3.09	3.73	3.095	3.727
5	5.12	5.80	5.116	5.796
6	7.64	8.35	7.644	8.355
7	10.67	11.41	10.681	11.413
8	14.21	14.97	14.227	14.975
9	18.25	19.05	18.289	19.047
10	22.80	23.64	22.870	23.637

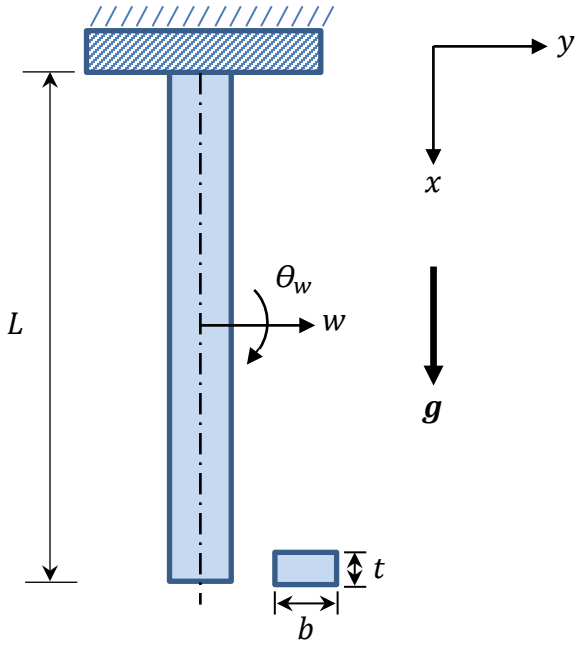

Fig. 2.6 Schematic drawing of vertically hanging cantilever beam

2.3.2.3 Simulation (C)

In this demonstration, the influence of the neutral point location on the natural frequencies of the drill string is evaluated. The specifications of the drill string in [11] are selected and provided in Table 2.15. The boundary conditions of the drill string are assumed to be clamped ($u_1 = v_1 = w_1 = \theta_{x_1} = \theta_{y_1} = \theta_{z_1} = 0$) at the top to the rotary table and pinned ($v_{21} = w_{21} = v_{25} = w_{25} = 0$) at the stabilizers locations (1000 and 1200 m). The drill string is divided into 24 elements of equal length. Figure 2.7 displays a schematic drawing of the drill string.

The axial, torsional and bending natural frequencies of the drill string are computed by the developed *MATALB*® program for the neutral point location at 800, 1000 and 1200 meters. Table 2.16 presents the comparison between the natural

frequencies obtained by the developed algorithm and [11] for the case of non-rotating drill string.

Table 2.15 Drill string specifications [11]

Drill Pipe Geometric Properties	**Value**	
Drill Pipe Length, $\boldsymbol{L_p}$	1000	*m*
Drill Pipe Outer Diameter, $\boldsymbol{D_o}$	0.127	*m*
Drill Pipe Inner Diameter, $\boldsymbol{D_i}$	0.095	*m*
Drill Collar Geometric Properties		
Drill Collar Length, $\boldsymbol{L_c}$	200	*m*
Drill Collar Outer Diameter, $\boldsymbol{D_o}$	0.2286	*m*
Drill Collar Inner Diameter, $\boldsymbol{D_i}$	0.095	*m*
Material Properties		
Mass density, $\boldsymbol{\rho}$	7850	kg/m^3
Modulus of Elasticity, $\boldsymbol{E}$	210	*GPa*
Shear Modulus, $\boldsymbol{G}$	76.923	*GPa*
Number of elements	24	

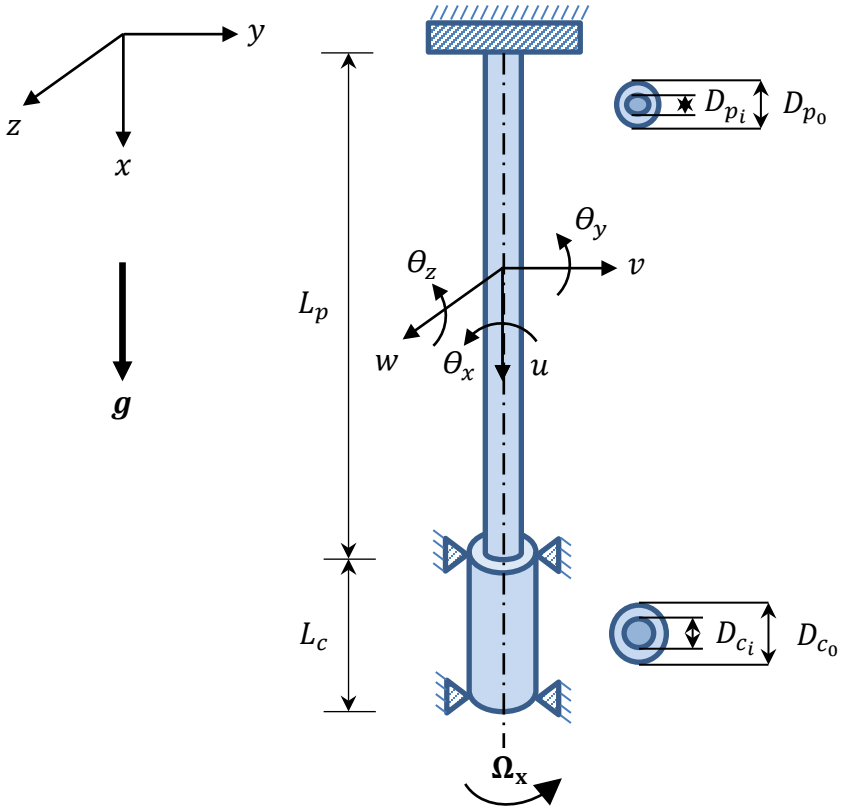

Fig. 2.7 Schematic drawing of full scale drill string

Table 2.16 Natural frequencies of drill string (rad/sec)

Mode	[11]			Alsaffar		
	Neutral Point Location					
	800 m	1000 m	1200 m	800 m	1000 m	1200 m
Lateral	0.1534	0.1694	0.2415	0.15338	0.16938	0.24154
Lateral	0.2955	0.3488	0.4230	0.29550	0.34884	0.42298
Lateral	0.3863	0.4272	0.4867	0.38634	0.42724	0.48666
Lateral	0.5344	0.5327	0.7310	0.53441	0.53265	0.73096
Lateral	0.6825	0.7134	0.9422	0.68247	0.71341	0.94216
Torsional	1.7050	1.7050	1.7050	1.70504	1.70504	1.70504
Torsional	10.1197	10.1197	10.1197	10.11974	10.11974	10.11974
Torsional	19.8168	19.8168	19.8168	19.81679	19.81679	19.81679
Torsional	29.7083	29.7083	29.7083	29.70832	29.70832	29.70832
Torsional	39.6990	39.6990	39.6990	39.69902	39.69902	39.69902
Axial	4.0076	4.0076	4.0076	4.00764	4.00764	4.00764
Axial	17.2617	17.2617	17.2617	17.26171	17.26171	17.26171
Axial	32.8832	32.8832	32.8832	32.88319	32.88319	32.88319
Axial	48.9437	48.9437	48.9437	48.94365	48.94365	48.94365
Axial	65.0280	65.0280	65.0280	65.02805	65.02805	65.02805

2.3.2.4 Simulation (D)

The gyroscopic effect on rotating shaft natural frequencies is demonstrated in this simulation. *ANSYS*® (Mechanical *APDL* 15.0, example 8.5) simulation of simply supported shaft spinning at 30,000 rad/sec is adopted. Table 2.17 shows the shaft material and geometric properties. The shaft is modeled with beam element having four degrees of freedom at each node. The four degrees of freedom consist of two translations (v, w) and two rotations (θ_y, θ_z). The translations degrees of freedom are two transverse displacements in the y & z directions while the rotations degrees of freedom are two bending rotations about the y & z axes as shown in Figure 2.8. The shaft is discretized with eight elements of equal length. The boundary conditions of the shaft are assumed to be pinned at both ends ($v_1 = w_1 = v_9 = w_9 = 0$). Using the

developed *MATALB®* program the bending natural frequencies of the shaft are determined for the case of non-rotating ($\Omega_x = 0$) and rotating ($\Omega_x = 30{,}000\ rad/sec$) shaft. The obtained bending natural frequencies are compared to results in Table 2.18. In addition, a Campbell diagram is generated for shaft rotational speeds ranging from 0 to 30,000 rad/sec as shown in Figure 2.9.

Table 2.17 Simply supported shaft specifications [*ANSYS®* - Example 8.5]

Geometric Properties	**Value**	
Shaft length, ***L***	8	*m*
Shaft Diameter, ***D***	0.2	*m*
Material Properties		
Mass density, $\boldsymbol{\rho}$	7800	kg/m^3
Poisson's ratio, $\boldsymbol{\nu}$	0.3	
Young's Modulus, ***E***	200	*GPa*
Number of Elements	8	

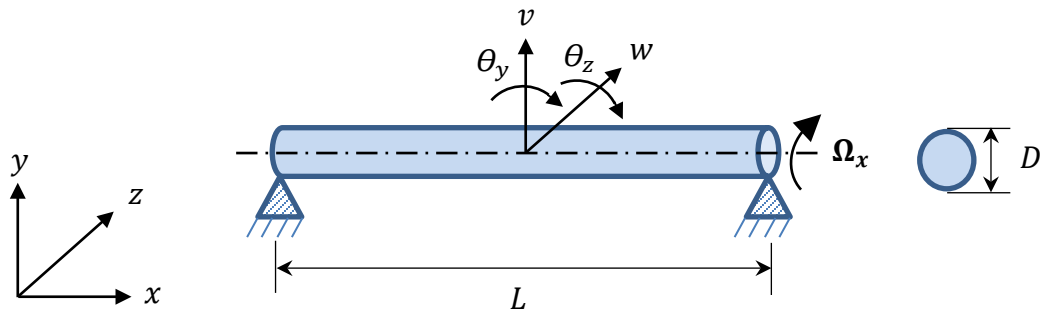

Fig. 2.8 Simply supported shaft (*ANSYS®* - Example 8.5)

Table 2.18 Shaft bending natural frequencies (*Hz*)

Mode		$\Omega_x = 0$ rad/sec			$\Omega_x = 30,000$ rad/sec		
		ANSYS® APDL	ANSYS® Workbench	Alsaffar	ANSYS® APDL	ANSYS® Workbench	Alsaffar
1	BW	6.207	6.206	6.213	4.639	4.637	4.639
	FW	6.207	6.206	6.213	8.305	8.304	8.319
2	BW	24.750	24.783	24.844	18.547	18.549	18.557
	FW	24.750	24.783	24.844	33.027	33.112	33.26
3	BW	55.461	55.712	55.902	41.735	41.800	41.778
	FW	55.461	55.712	55.902	73.701	74.225	74.447

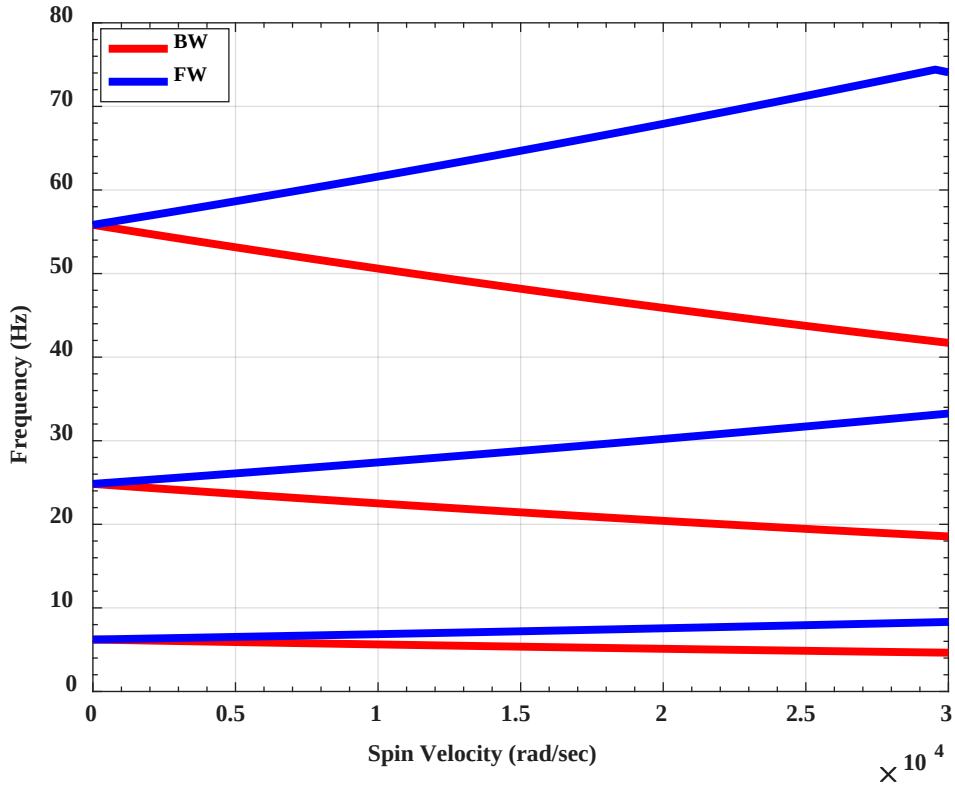

Fig. 2.9 Campbell diagram of simply supported rotating shaft

2.4 Summary

This chapter has presented the development of finite element model of conventional drill string based on Bernoulli-Euler beam theory. Torsional, lateral and longitudinal vibrations along with the gyroscopic and gravitational effects are considered in the developed model. The developed finite element formulations are integrated into a computational algorithm to obtain the drill string vibration characteristics. The validation of the generated *MATALB*® routine is achieved by performing four various numerical demonstrations.

Chapter 3

Passive Periodic Drill String

3.1 Overview

Periodic structures, whether passive or active, are structures that consist of identical substructures, or cells, connected in an identical manner. The periodicity can be introduced either by geometrical or material discontinuities as shown in Fig. 3.1. Because of such periodicity, these periodic structures exhibit unique dynamic characteristics stemming from their ability of acting as mechanical filters for wave propagation. As a result, waves propagate along the periodic structures only within specific frequency bands called the ‘‘*Pass Bands*’’, while these waves are completely blocked within other frequency bands called the ‘‘*Stop Bands*”. With such unique filtering characteristics, it would be possible to passively or actively control the wave propagation both in spectral and spatial domains in an attempt to stop or confine the propagation of undesirable external disturbances.

The development of periodic structure theory was originally intended for solid state applications [28] and extended, in the early 1970s, to the design of mechanical structures [29] and [30]. Since then, the theory has been applied to a wide variety of structures such as discrete spring-mass systems [31], continuous periodic beams [29], [32] and [33], stiffened plates [34], [35] and [36], ribbed shells [37] and space structures.

In this chapter, the theory of periodic structures is presented and applied to the conventional drill string with passive periodic inserts in an attempt to passively

generate and control the zones of stop bands. Numerical examples of passive periodic drill string are provided and compared with conventional drill string in order to emphasize the potential and merits of the proposed approach.

In addition, the stop and pass bands characteristics of gyroscopic periodic drill string are determined by developing a novel approach which is compatible with gyroscopic systems while maintain the concept of Bloch wave propagation in periodic structures. The dispersion curves of the gyroscopic periodic drill string are obtained for different rotational speeds and compared with non-rotating periodic drill string in an attempt to quantify the effect of the gyroscopic forces on the band gap characteristics. Numerical simulations are provided and compared with Campbell diagram as well as with structural frequency responses generated by the theory of finite element presented in chapter two.

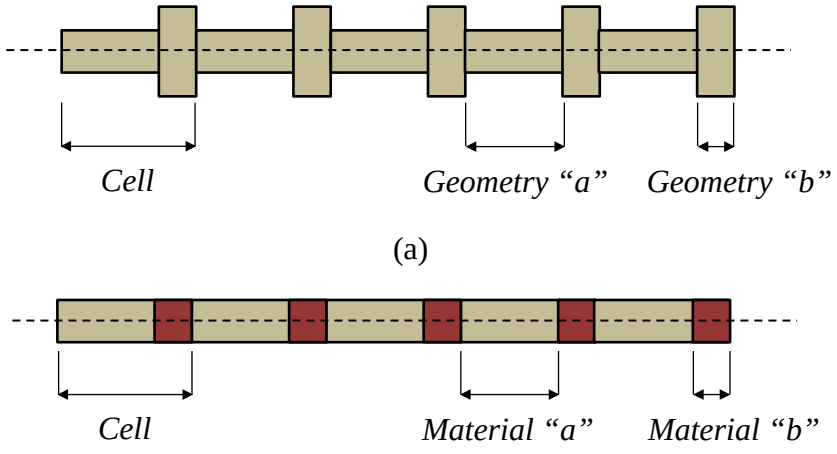

Fig. 3.1 Types of passive periodic structures, (a) Geometrical discontinuity and (b) Material discontinuity

3.2 Modeling of Non-Rotating Passive Periodic Drill String

3.2.1 Overview

The dynamics of non-rotating passive periodic drill string are determined using the transfer matrix method as described by [38]. The methodologies for determining the pass and stop bands, the natural frequencies, the mode shapes and the frequency response of the periodic drill string are introduced. Illustrating example is given and compared with the theory of finite element presented in chapter two.

3.2.2 Transfer Matrix Method

The drill pipes section of the proposed periodic drill string shown in Fig. 1.4 is divided into identical periodic cells. Fig. 3.2 shows the dynamics of two adjacent periodic cells. For a given cell k, the vector $\{\delta^e\}$ defines the deflection vector described in Eq. (2.3) and the vector $\{F^e\}$ defines the force vector with subscripts t_k and b_k denoting the top and bottom sides of the k^{th} cell respectively.

For a non-rotating drill string ($\Omega_x = 0$), the dynamics of the k^{th} cell are determined from the finite element expression [38]:

$$[M^e]\{\ddot{\delta}^e\}_k + [K^e]\{\delta^e\}_k = \{F^e\}_k \tag{3.1}$$

or,

$$\begin{bmatrix}[M^e_{tt}] & [M^e_{tb}]\\ [M^e_{bt}] & [M^e_{bb}]\end{bmatrix}\begin{Bmatrix}\{\ddot{\delta}^e\}_t\\ \{\ddot{\delta}^e\}_b\end{Bmatrix}_k + \begin{bmatrix}[K^e_{tt}] & [K^e_{tb}]\\ [K^e_{bt}] & [K^e_{bb}]\end{bmatrix}\begin{Bmatrix}\{\delta^e\}_t\\ \{\delta^e\}_b\end{Bmatrix}_k = \begin{Bmatrix}\{F^e\}_t\\ \{F^e\}_b\end{Bmatrix}_k \tag{3.2}$$

where $\left[M^e_{ij}\right]^c$ and $\left[K^e_{ij}\right]^c$ are the cell's mass and stiffness matrices that can be appropriately assembled from the augmented element mass and stiffness matrices derived in Eqs. (2.12) and (2.26) respectively. Also, $\{\delta^e\}_k$ defines the cell's deflection

vector with $\{\delta^e\}_k = \{\{\delta^e\}_t \quad \{\delta^e\}_b\}_k^T$ while $\{F^e\}_k$ defines the cell's force vector with$\{F^e\}_k = \{\{F^e\}_t \quad \{F^e\}_b\}_k^T$.

For a sinusoidal excitation at a frequency ω, Eq. (3.2) can be written as

$$\begin{bmatrix} [K_{tt}^e] - \omega^2[M_{tt}^e] & [K_{tb}^e] - \omega^2[M_{tb}^e] \\ [K_{bt}^e] - \omega^2[M_{bt}^e] & [K_{bb}^e] - \omega^2[M_{bb}^e] \end{bmatrix} \begin{Bmatrix} \{\delta^e\}_t \\ \{\delta^e\}_b \end{Bmatrix}_k = \begin{Bmatrix} \{F^e\}_t \\ \{F^e\}_b \end{Bmatrix}_k \tag{3.3}$$

or,

$$\begin{bmatrix} [K_{d_{tt}}] & [K_{d_{tb}}] \\ [K_{d_{bt}}] & [K_{d_{bb}}] \end{bmatrix} \begin{Bmatrix} \{\delta^e\}_t \\ \{\delta^e\}_b \end{Bmatrix}_k = \begin{Bmatrix} \{F^e\}_t \\ \{F^e\}_b \end{Bmatrix}_k \tag{3.4}$$

where $[K_d]$ is the cell dynamic stiffness matrix.

Consequently, Eq. (3.4) can be rearranged and written as

$$\begin{Bmatrix} \{\delta^e\}_b \\ \{F^e\}_b \end{Bmatrix}_k = \begin{bmatrix} -[K_{d_{tb}}]^{-1}[K_{d_{tt}}] & [K_{d_{tb}}]^{-1} \\ -[K_{d_{bb}}][K_{d_{tb}}]^{-1}[K_{d_{tt}}] + [K_{d_{bt}}] & [K_{d_{bb}}][K_{d_{tb}}]^{-1} \end{bmatrix} \begin{Bmatrix} \{\delta^e\}_t \\ \{F^e\}_t \end{Bmatrix}_k \tag{3.5}$$

Considering the compatibility and equilibrium conditions at the interface between k^{th} and $k+1^{th}$ cells, yields the following constraint

$$\begin{Bmatrix} \{\delta^e\}_b \\ \{F^e\}_b \end{Bmatrix}_k = \begin{bmatrix} 1 & 0 \\ 0 & -1 \end{bmatrix} \begin{Bmatrix} \{\delta^e\}_t \\ \{F^e\}_t \end{Bmatrix}_{k+1} \tag{3.6}$$

Substituting Eq. (3.6) into Eq. (3.5) yields

$$\begin{Bmatrix} \{\delta^e\}_t \\ \{F^e\}_t \end{Bmatrix}_{k+1} = \begin{bmatrix} -[K_{d_{tb}}]^{-1}[K_{d_{tt}}] & [K_{d_{tb}}]^{-1} \\ [K_{d_{bb}}][K_{d_{tb}}]^{-1}[K_{d_{tt}}] - [K_{d_{bt}}] & -[K_{d_{bb}}][K_{d_{tb}}]^{-1} \end{bmatrix} \begin{Bmatrix} \{\delta^e\}_t \\ \{F^e\}_t \end{Bmatrix}_k \tag{3.7}$$

or,

$$\begin{Bmatrix} \{\delta^e\}_t \\ \{F^e\}_t \end{Bmatrix}_{k+1} = [T_k] \begin{Bmatrix} \{\delta^e\}_t \\ \{F^e\}_t \end{Bmatrix}_k \tag{3.8}$$

where $[T_k]$ is the transfer matrix that relates the state vector $\{\{\delta^e\}_t \ \{F^e\}_t\}^T$ at the top end of the $k+1^{th}$ cell to that at the top end of the k^{th} cell.

For identical cells along the drill string, $[T_k]$ is the same for all the cells and Eq. (3.8) reduces to

$$\begin{Bmatrix}\{\delta^e\}_t \\ \{F^e\}_t\end{Bmatrix}_{k+1} = [T]\begin{Bmatrix}\{\delta^e\}_t \\ \{F^e\}_t\end{Bmatrix}_k \tag{3.9}$$

In a more compact form, Eq. (3.9) can be written as

$$S_{k+1} = [T]S_k \tag{3.10}$$

where S_k and $[T]$ denote the state vector $\{\{\delta^e\}_t \ \{F^e\}_t\}_k^T$ and the cell transfer matrix of the drill string respectively.

The band gap characteristics of the drill string are determined by using the transfer matrix $[T]$ described in Eq. (3.10).

The transfer matrix $[T]$ has the following eigenvalue expression

$$[T]S_{k+1} = \lambda S_{k+1} \tag{3.11}$$

where λ denotes the eigenvalues of the transfer matrix $[T]$ and can be written as

$$\lambda = e^{\mu} = e^{\alpha+i\beta} \tag{3.12}$$

where μ is defined as the cell's propagation constant. The real part of the propagation constant α represents the logarithmic decay of the state vector from one cell to the subsequent, while the imaginary part β defines the phase difference between the adjacent cells. A zero α (i.e. when μ is purely imaginary), a pass band condition is established as the wave propagates through the periodic cells with no amplitude attenuation. A non-zero α represents a condition equivalent to a "*stop*" or "*attenuation*" band where the wave propagation is attenuated from one cell to the

adjacent one. In this case, the purely elastic passive periodic drill string acts as if it is a damped structure that stops rather than attenuates the structural vibration. For such unique behavior, the passive periodic drill string can be very effective in impeding the propagation of undesirable destructive vibration as shown in section 3.2.3.

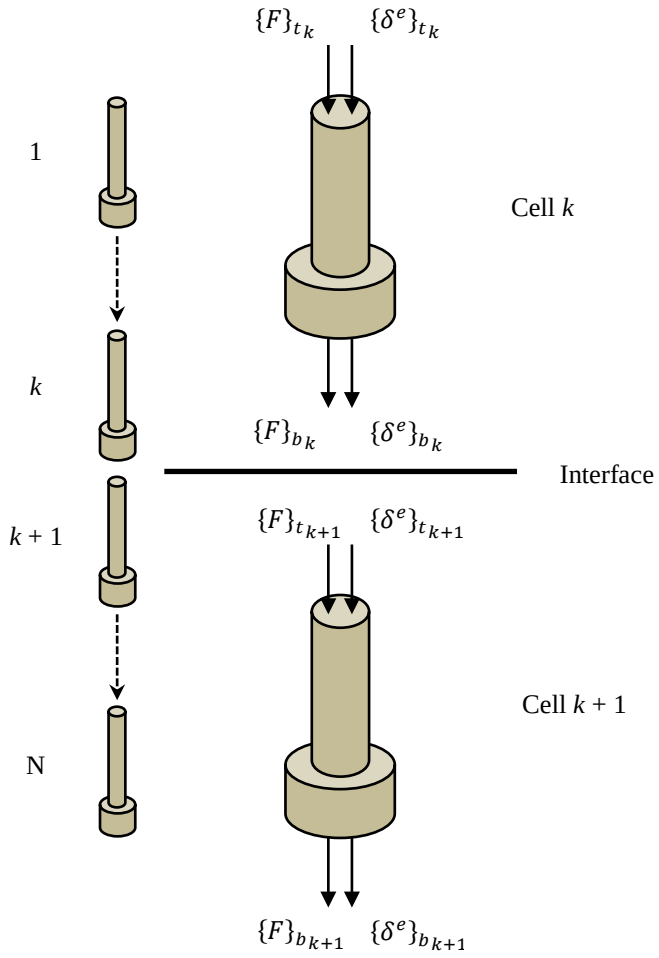

Fig. 3.2 Interaction between two neighboring periodic drill string cells

For a passive periodic unit cell of the drill string shown in Fig. 3.3, the dynamic characteristics of the individual substructures, "*a*" and "*b*" can be described by the transfer matrices $[T_a]$ and $[T_b]$, which can be obtained from Eq. (3.8). Combining the

transfer matrices of the substructures "*a*" and "*b*", yields the transfer matrix $[T]$ for the unit cell as follows

$$[T] = [T_b][T_a] \tag{3.13}$$

The pass and stop bands characteristics of the passive periodic drill string can then be determined by investigating the eigenvalues of the transfer matrix $[T]$ described in Eq. (3.10) for different combinations of longitudinal rigidities and physical properties of segments "*a*" and "*b*".

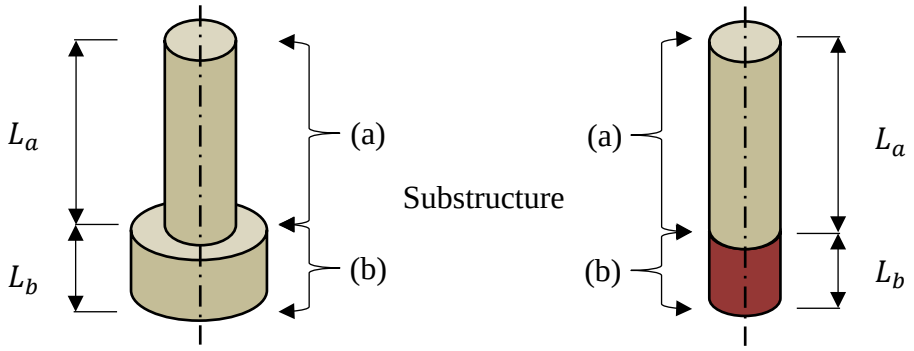

Fig. 3.3 Unit cells of passive periodic drill string

3.2.3 Band Gap Characteristics of Non-Rotating Periodic Drill String

In this section, the methodologies for determining the band gap characteristics of non-rotating passive periodic structures are introduced. Illustrating example is provided to demonstrate the application of these methodologies to passive periodic drill string.

Consider the suspended passive periodic drill string shown in Fig. 3.4, which has geometrical specifications and material properties provided in Table 3.1. The drill string is assumed to be fixed at its upper end and simply supported at its lower end ($L - L_{in}$) by a one inch long sleeve bearing. The drill string is made of assemblies of periodic cells. Each of these unit cells consists of two substructures, "Drill String Shaft" and "Insert", which have the same material with different cross sections.

The dynamic characteristics of the individual substructure can be described by its transfer matrix $[T_{sh}]$ and $[T_{in}]$, as defined by Eq. (3.8). Combining the transfer matrices of the substructures "Drill String Shaft" and "Insert", yields the transfer matrix $[T] = [T_{in}][T_{sh}]$ for the unit cell k.

The band gap characteristics of the non-rotating passive periodic drill string is determined by investigating the eigenvalues of the transfer matrix $[T]$. Using a set of five periodic inserts, the stop and pass bands for the lateral, longitudinal and torsional vibration modes of the considered example are generated by the theory of periodic structures as shown in Fig. 3.5 (c), Fig. 3.6 (c) and Fig. 3.7 (c).

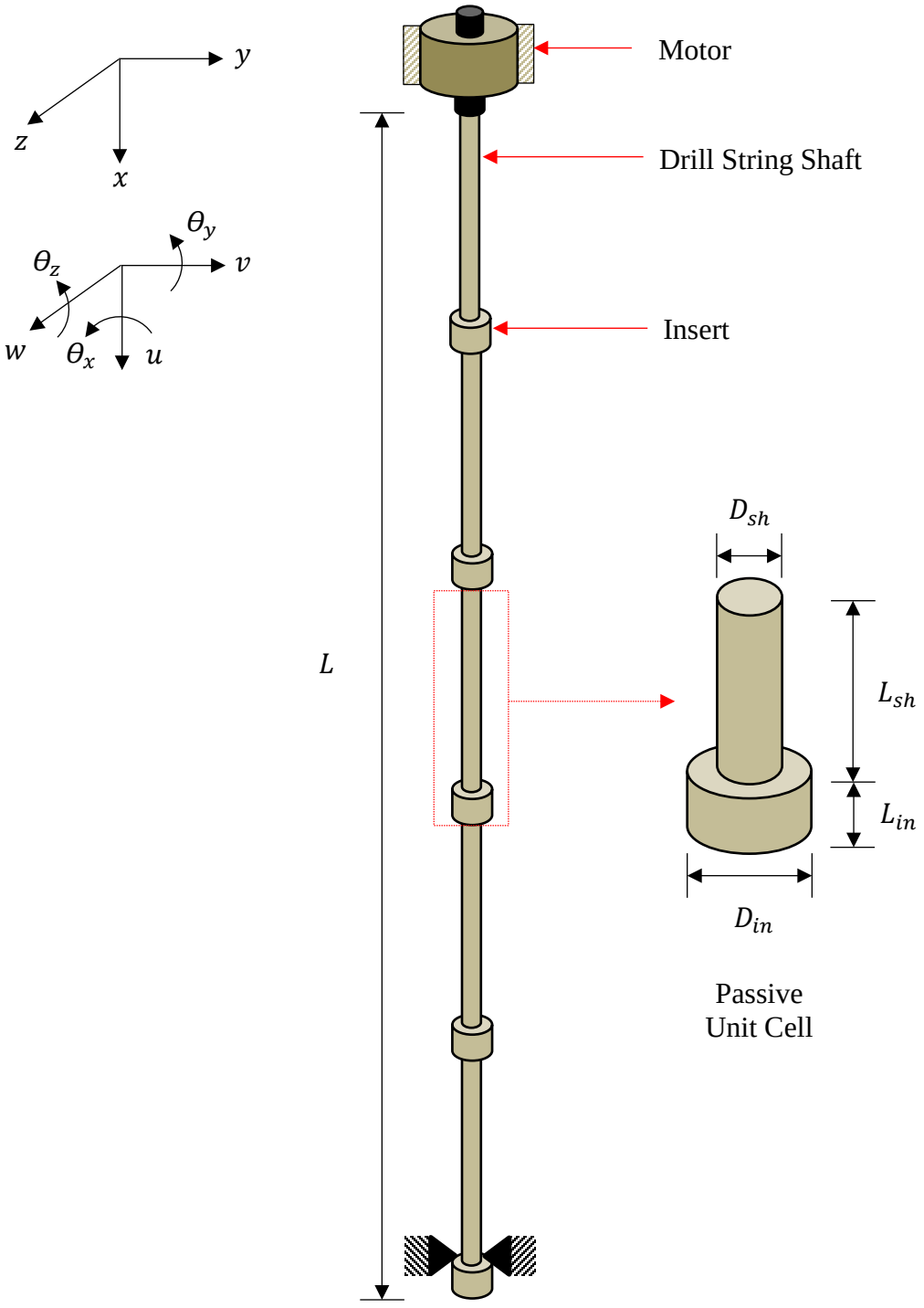

Fig. 3.4 Passive periodic drill string

To validate the band gap characteristics of the considered passive periodic drill string example, the structure is subjected to a combination of torsional moment, axial and bending forces at its bottom end. Non-Collocated dynamic responses near the root of the drill string are generated by the method of finite element described in chapter two. Fig. 3.5 (a), Fig. 3.6 (a) and Fig. 3.7 (a) show the lateral, longitudinal and torsional frequency responses for conventional drill string while Fig. 3.5 (b), Fig. 3.6 (b) and Fig. 3.7 (b) show the lateral, longitudinal and torsional frequency responses for the passive periodic drill string respectively.

From the set of Fig. 3.5 to Fig. 3.7, it is evident that the periodic drill string exhibits stop band zones where the system natural frequencies were completely eliminated. Therefore, it is advantageous to operate the periodic drill string in the stop band zones without experiencing high vibration amplitudes.

Table 3.1 Passive periodic drill string specifications

Geometric Properties	**Value**	
Drill String Total Length, $\boldsymbol{L}$	1771.65	mm
Drill String Shaft Diameter, $\boldsymbol{D_{sh}}$	3.175	mm
Periodic Inserts Length, $\boldsymbol{L_{in}}$	6.35	mm
Periodic Inserts Outer diameter, $\boldsymbol{D_{in}^{o}}$	50.80	mm
Periodic Inserts Inner diameter, $\boldsymbol{D_{in}^{i}}$	3.175	mm
Material Properties		
Mass density, $\boldsymbol{\rho}$	8000	kg/m^3
Modulus of Elasticity, $\boldsymbol{E}$	193	GPa
Shear Modulus, $\boldsymbol{G}$	77.2	GPa

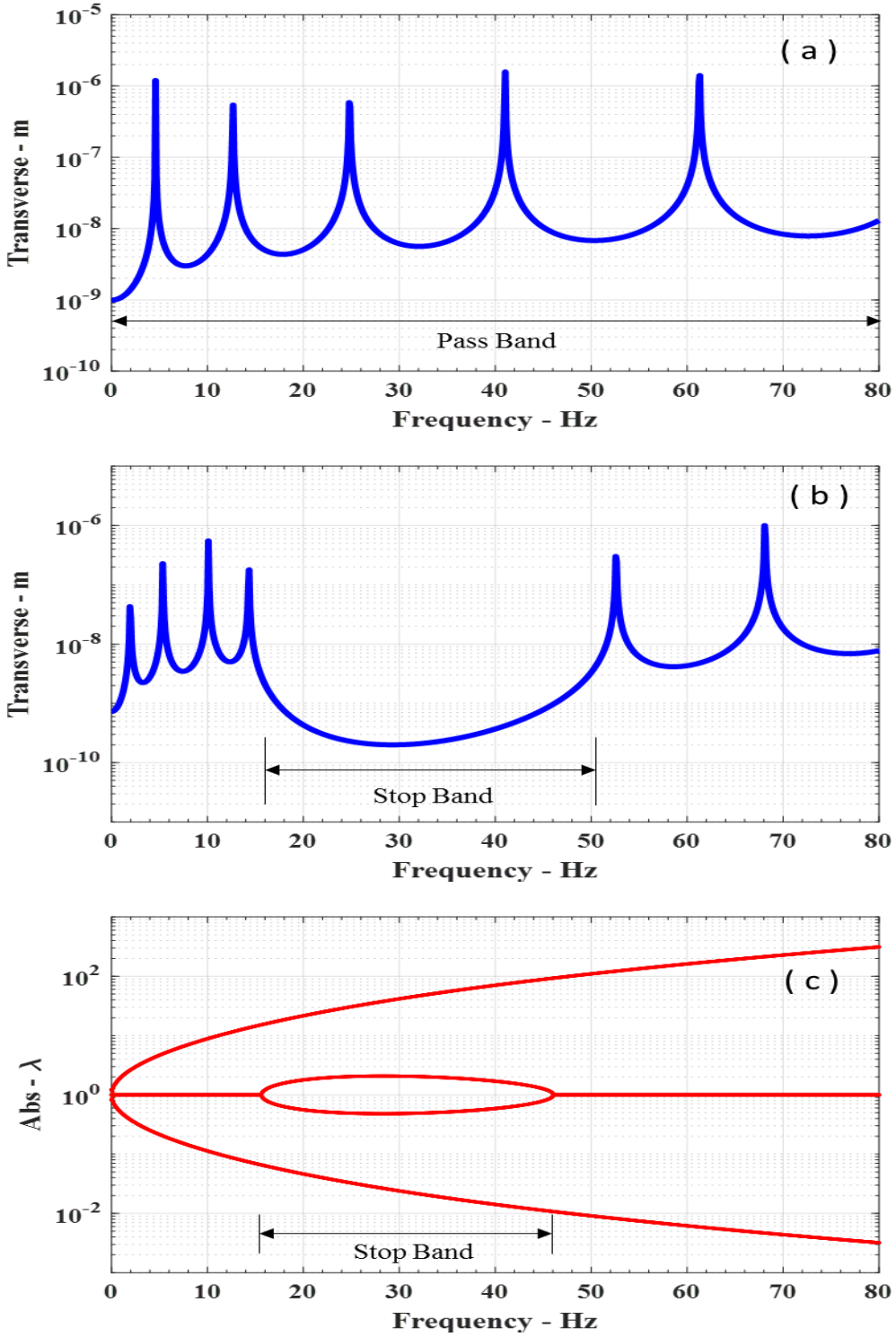

Fig. 3.5 (a) Lateral frequency response of passive conventional drill string, (b) Lateral frequency response of passive periodic drill string & (c) Lateral band gap characteristics of passive periodic drill string

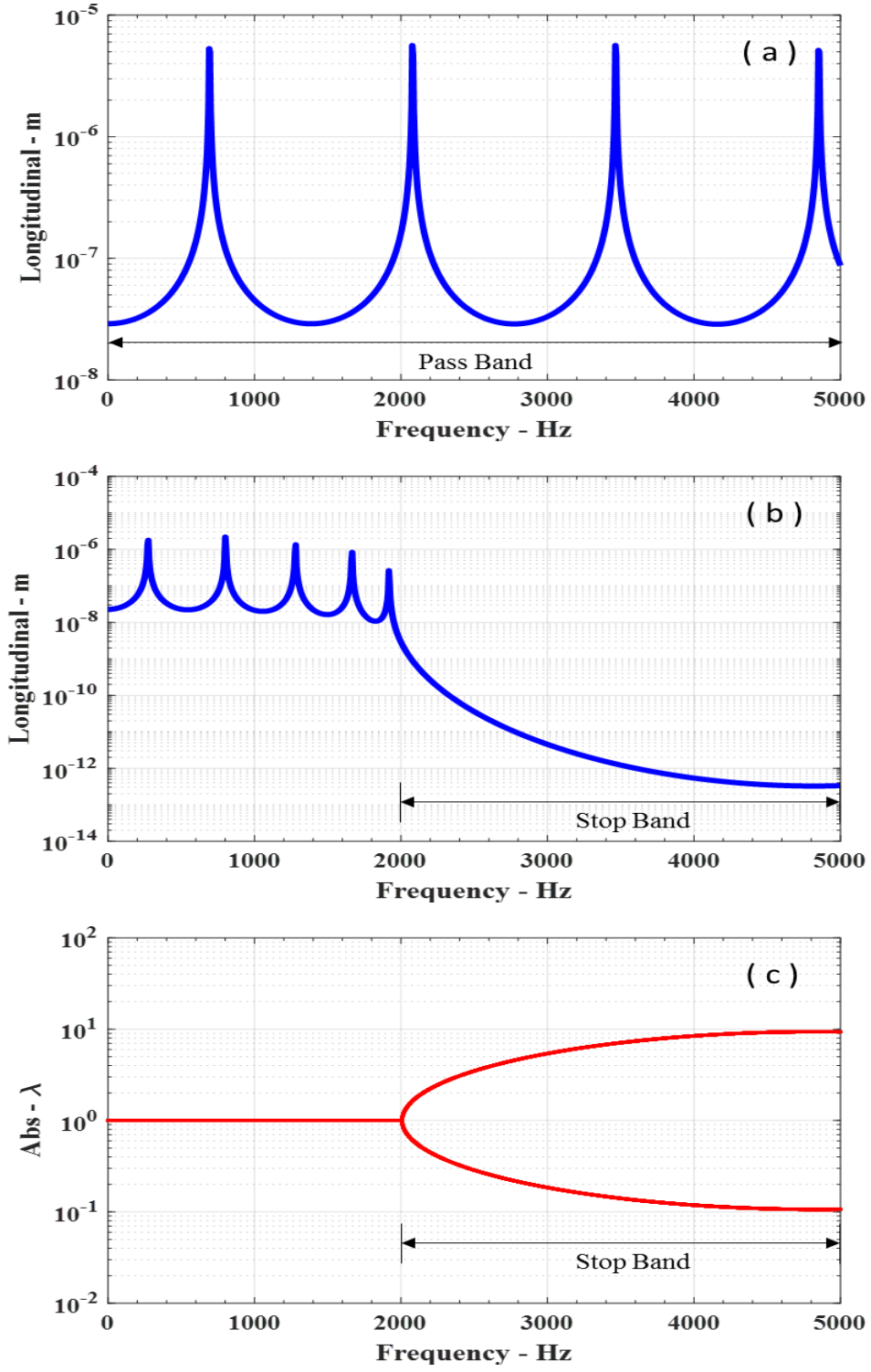

Fig. 3.6 (a) Longitudinal frequency response of passive conventional drill string, (b) Longitudinal frequency response of passive periodic drill string & (c) Longitudinal band gap characteristics of passive periodic drill string

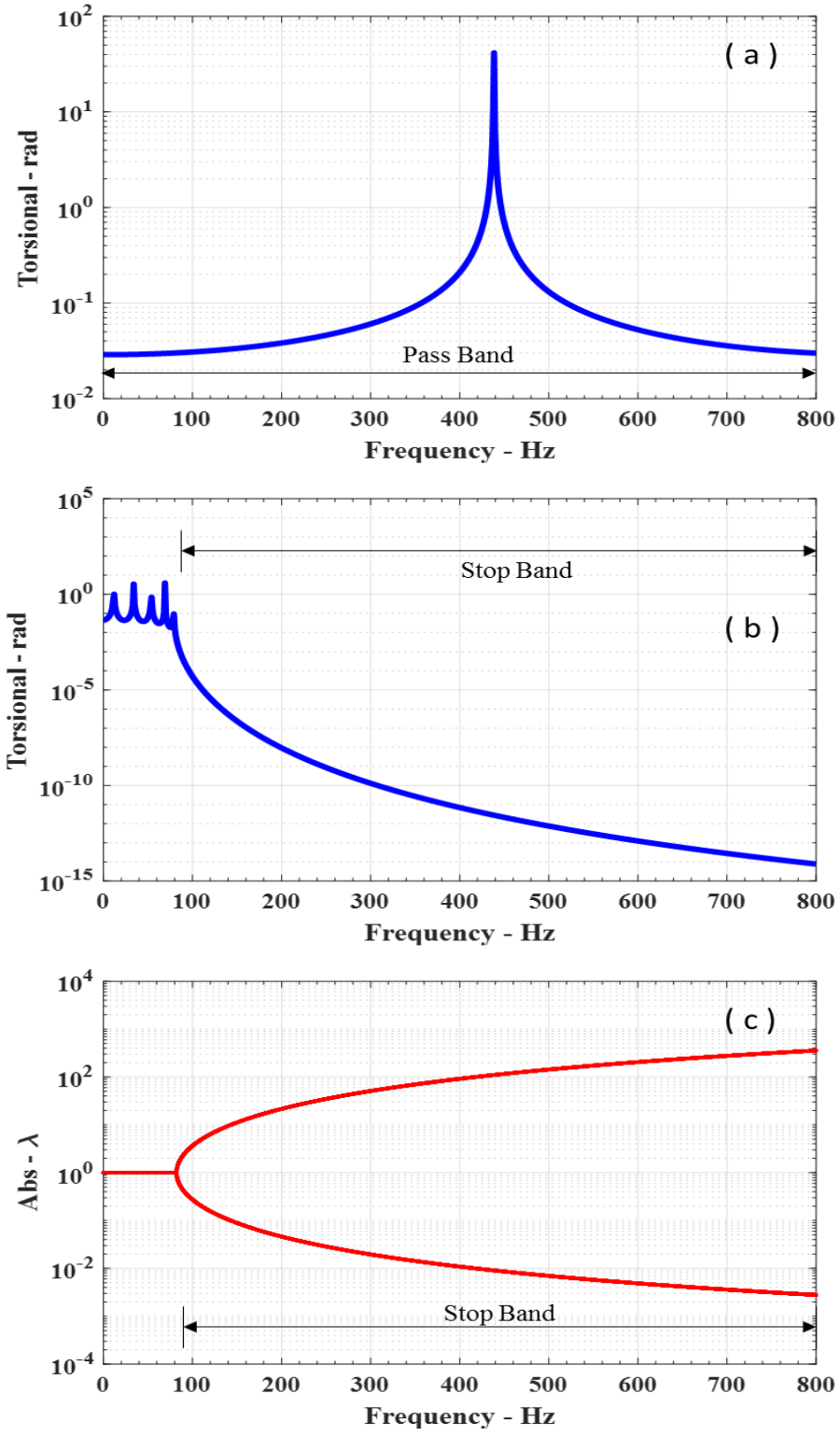

Fig. 3.7 (a) Torsional frequency response of passive conventional drill string, (b) Torsional frequency response of passive periodic drill string & (c) Torsional band gap characteristics of passive periodic drill string

3.3 Modeling of Gyroscopic Passive Periodic Drill String

3.3.1 Overview

The dynamic characteristics for a non-rotating passive periodic drill string are presented in section 3.2.2. In this section, the stop and pass bands of the passive periodic drill string are determined using a novel approach which is compatible with gyroscopic systems while maintaining the concept of Bloch wave propagation in periodic structures. In this approach, the dispersion curves of the periodic drill string are determined based on complex wavenumbers versus real frequencies. The obtained characteristics would relate to wave propagation admitting spatial attenuation due energy redistribution.

In this approach, the dispersion curves of the passive periodic gyroscopic drill string are determined for different rotational speeds. The obtained characteristics are compared with non-rotating passive periodic drill string in an attempt to quantify the effect of the gyroscopic forces on the band gap characteristics.

The developed approach has not been considered before in the literature particularly for gyroscopic systems. Illustrating numerical example of passive periodic drill string is provided and compared with conventional drill string in order to emphasize the potential and merits of the proposed approach.

3.3.2 Bloch Wave Propagation Theory

The drill pipes section of the proposed periodic drill string shown in Fig. 1.4 is divided into identical periodic cells. Fig. 3.8 shows the degrees of freedom of a passive unit cell. For a given unit cell, the vector $\{\delta^e\}$ defines the nodal deflection vector described in Eq. (2.3) and the vector $\{F^e\}$ defines the generalized forcing function acting on the unit cell such as external loads and moments.

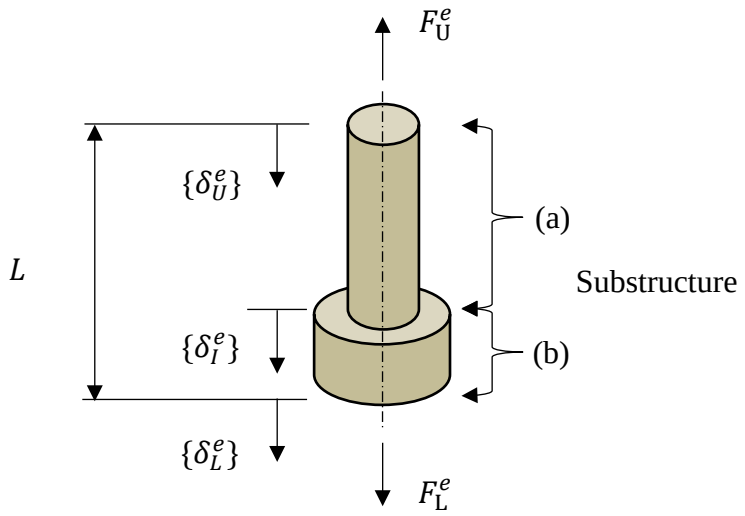

Fig. 3.8 Passive unit cell degrees of freedom of periodic drill string

For a gyroscopic passive periodic drill string, the finite element model for a unit cell can be written as

$$[M]^c\{\ddot{\delta}\}^c + \Omega_x[G]^c\{\dot{\delta}\}^c + [K]^c\{\delta\}^c = \{F\}^c \tag{3.14}$$

where $[M]^c$, $[G]^c$ and $[K]^c$ are the cell's mass, gyroscopic and stiffness matrices that can be appropriately assembled from the augmented element mass, gyroscopic and

stiffness matrices derived in Eqs. (2.12) and (2.26) respectively with superscript c denoting the gyroscopic unit cell.

The nodal deflection vector of a unit cell $\{\delta\}^c$ is defined as

$$\{\delta\}^c = \left\{\{\delta_U^e\}\,\{\delta_I^e\}\,\{\delta_L^e\}\right\}^T \tag{3.15}$$

where $\{\delta_U^e\}$, $\{\delta_I^e\}$ and $\{\delta_L^e\}$ denote the upper, internal and lower deflection vectors.

Eq. (3.15) is condensed to support Block wave propagation. Hence, the displacements at the boundaries are related as

$$\{\delta_L^e\} = e^{-ikL}\{\delta_U^e\} \tag{3.16}$$

where k and L denote the wave number and the length of the unit cell, respectively.

Hence, $\{\bar{\delta}\}^c$ is defined as an independent nodal deflection vector such that

$$\{\bar{\delta}\}^c = \left\{\{\delta_U^e\}\,\{\delta_I^e\}\right\}^T \tag{3.17}$$

The deflection vectors $\{\delta\}^c$ and $\{\bar{\delta}\}^c$ are related as

$$\{\delta\}^c = T\{\bar{\delta}\}^c \tag{3.18}$$

where T is a transformation matrix described as

$$T = \begin{bmatrix} I & 0 & Ie^{-ikL} \\ 0 & I & 0 \end{bmatrix}^T \tag{3.19}$$

Substituting Eqs. (3.18) and (3.19) into Eq. (3.14) , the finite element model for a gyroscopic unit cell reduces to

$$[\bar{M}]^c\{\ddot{\bar{\delta}}\}^c + \Omega_x[\bar{G}]^c\{\dot{\bar{\delta}}\}^c + [\bar{K}]^c\{\bar{\delta}\}^c = \{\bar{F}\}^c \tag{3.20}$$

where

$$[\bar{M}]^c = T^T\,[M]^c\,T \qquad [\bar{G}]^c = T^T\,[G]^c\,T$$

$$[\bar{K}]^c = T^T\,[K]^c\,T \qquad \{\bar{F}\}^c = T^T\,\{F\}^c$$

Eq. (3.20) can be represented in a state space form [39] such as

$$\begin{bmatrix} [\bar{K}]^c & 0 \\ 0 & [\bar{M}]^c \end{bmatrix} \{\dot{\bar{y}}\}^c + \begin{bmatrix} 0 & -[\bar{K}]^c \\ [\bar{K}]^c & \Omega_x[\bar{G}]^c \end{bmatrix} \{\bar{y}\}^c = \begin{Bmatrix} 0 \\ \{\bar{F}\}^c \end{Bmatrix} \tag{3.21}$$

where $\{\bar{y}\}^c = \left\{\{\bar{\delta}\}^c \ \{\dot{\bar{\delta}}\}^c\right\}^T$

Let the state space solution be assumed as

$$\{\bar{y}\}^c = e^{\lambda t}\{\hat{y}\}^c \tag{3.22}$$

where $\{\hat{y}\}^c = \{\ \{x\} + i\{z\}\ \}^c$ and $\lambda = \pm i\omega$

Eq. (3.22) leads to the following eigenvalue problem

$$\left[i\omega \begin{bmatrix} [\bar{K}]^c & 0 \\ 0 & [\bar{M}]^c \end{bmatrix} + \begin{bmatrix} 0 & -[\bar{K}]^c \\ [\bar{K}]^c & \Omega_x[\bar{G}]^c \end{bmatrix} \right] \{\ \{x\} + i\{z\}\ \}^c = \begin{Bmatrix} 0 \\ 0 \end{Bmatrix} \tag{3.23}$$

In a compact form, Eq. (3.23) reduces to

$$[\ i\omega[M^*]^c + [G^*]^c\ ]\ \{\ \{x\} + i\{z\}\ \}^c = 0 \tag{3.24}$$

where

$$[M^*]^c = \begin{bmatrix} [\bar{K}]^c & 0 \\ 0 & [\bar{M}]^c \end{bmatrix} \quad \text{and} \quad [G^*]^c = \begin{bmatrix} 0 & -[\bar{K}]^c \\ [\bar{K}]^c & \Omega_x[\bar{G}]^c \end{bmatrix}$$

Equating the real and imaginary coefficients in Eq. (3.24) yields

Real: $$[G^*]^c\{x\}^c = \omega[M^*]^c\{z\}^c \tag{3.25}$$

Imaginary: $$-[G^*]^c\{z\}^c = \omega[M^*]^c\{x\}^c \tag{3.26}$$

Eqs. (3.25) and (3.26) can be rewritten in compact and standard eigenvalue problem form such that

$$[A]^c\{z\}^c = \omega^2\{z\}^c \tag{3.27}$$

where

$$[A]^c = [M^*]^{c^{-1}}\ [\ [G^*]^c[M^*]^{c^{-1}}[G^*]^c\ ]$$

Note that all the entries of the matrix $[A]^c$ are function of the dimensionless wave number kL. Therefore, the eigenvalues of the matrix $[A]^c$ can be determined for different values of the wave number kL.

The eigenvalues λ_s are given by

$$\lambda_s(kL) = \omega_s \tag{3.28}$$

where $s = 1$ to n

The dispersion characteristics of the gyroscopic unit cell of the passive periodic drill string are constructed by plotting the resonant frequency ω_s against the wave number kL. The resulted dispersion curves further define the zones of stop and pass bands of the periodic drill string as illustrated in section 3.3.3.

3.3.3 Band Gap Characteristics of Gyroscopic Periodic Drill String

The considered numerical example in section 3.2.3 is used to demonstrate the generation of the dispersion characteristics of the gyroscopic unit cell of the passive periodic drill string. Using a set of five periodic inserts, the drill string dispersion characteristics are generated using only one single cell for the drill string rotational speeds of zero and 1920 *RPM* (32 *Hz*) as illustrated in Figs. 3.9 and 3.10. The numerical values of Figs. 3.9 and 3.10 are tabulated in Table 3.2. The unit cell finite element model computations are performed by dividing the periodic insert and the shaft into two and fifty elements respectively.

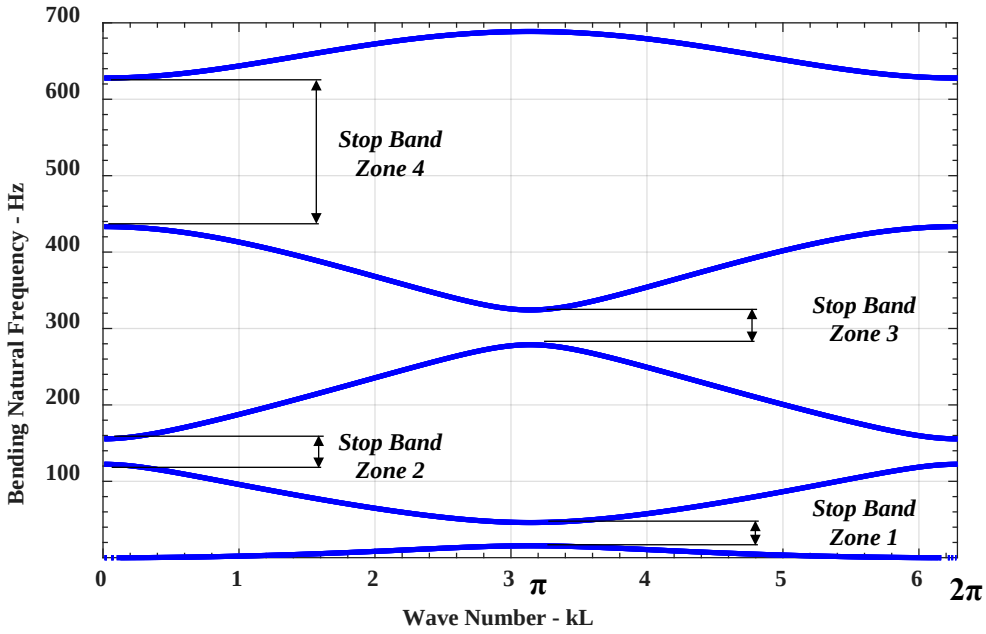

Fig. 3.9 Dispersion characteristics of a unit cell of passive periodic drill string at rotational speed of zero *RPM* – (zero *Hz*)

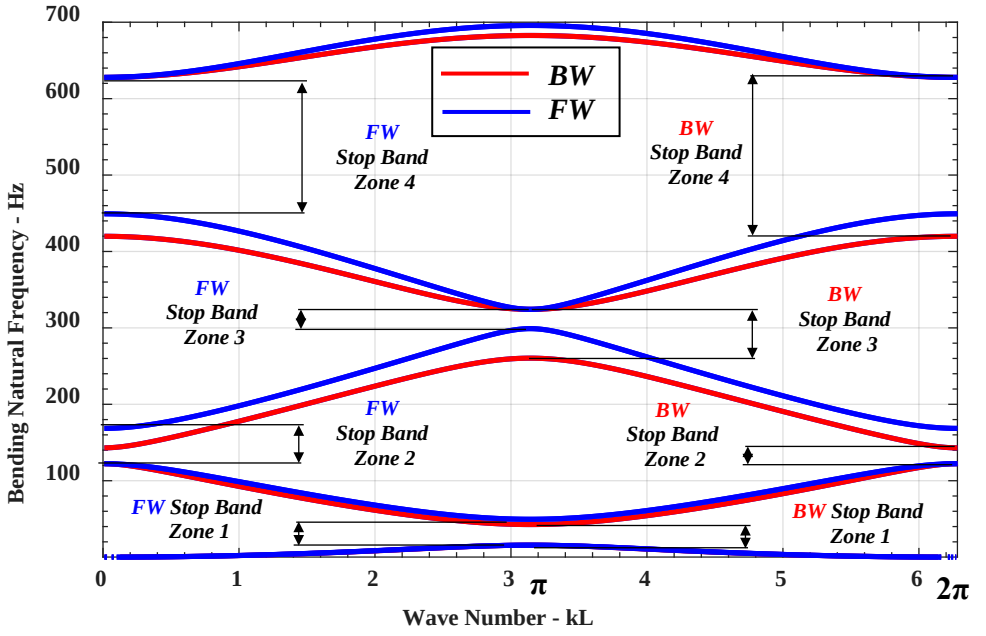

Fig. 3.10 Dispersion characteristics of a unit cell of passive periodic drill string at rotational speed of 1920 *RPM* – (32 *Hz*), (*BW* = Backward Whirl & *FW* = Forward Whirl)

In Fig. 3.10, the effect of the gyroscopic forces manifest themselves by splitting the modes of vibration to forward (*FW*) and backward (*BW*) modes. The vibrational modes that travel along an orbit in the direction of the drill string's rotation are denoted forward whirling modes whereas those traveling in the opposite direction are denoted as backward whirling modes. In particular, the gyroscopic forces contribute to changing the stiffness of the drill string system and hence its frequency. The stiffness is enhanced during forward whirling and degrades during backward whirling. Such an effect is magnified as the rotational speed increases as demonstrated in the frequency map shown in Fig. 3.11.

Table 3.2 Band gap limits numerical values of Figs. 3.9 and 3.10, (*BW* = Backward Whirl & *FW* = Forward Whirl)

Stop Bands	**Rotational Speed - *RPM***		
Hz	**0**	**1920**	
Zone 1	15.63	15.63	*BW*
		15.63	*FW*
	46.06	42.65	*BW*
		49.56	*FW*
Zone 2	122.30	122.30	*BW*
		122.30	*FW*
	155.60	143.00	*BW*
		168.50	*FW*
Zone 3	278.70	260.40	*BW*
		299.00	*FW*
	324.30	324.30	*BW*
		324.30	*FW*
Zone 4	433.40	419.90	*BW*
		449.30	*FW*
	627.80	627.80	*BW*
		627.80	*FW*

To validate the obtained gyroscopic band gap characteristics of the passive periodic drill string, Campbell diagram is generated using the finite element method described in chapter two. Campbell diagram is named after the Wilfred Campbell who introduced the concept in 1924. The diagram displays the evolution of the natural frequencies corresponding to the different mode of vibration as a function of the rotational speed of the shaft. Fig. 3.11 shows the Campbell diagram of the periodic drill string with shaft rotational speeds ranging from zero to 1920 *RPM*.

Besides Campbell diagram validation, the periodic drill string is subjected to bending force at its bottom at shaft rotational speeds of zero and 1920 *RPM*. Non-Collocated dynamic response near the root of the drill string are obtained by the method of the finite element described in chapter two. Fig. 3.12 displays Non-collocated lateral frequency response of the periodic drill string at shaft rotational speeds of zero and 1920 *RPM* respectively.

It is evident in Figs. 3.9-3.12 that the periodic drill string exhibits stop band zones where the system natural frequencies are completely eliminated. Therefore, it is advantageous to operate the periodic drill string in the stop band zones without experiencing high vibration amplitudes. Also, due to the gyroscopic forces effect the non-rotating stop band zones range splits into backward and forward stop band zones as the drill string starts to rotate. The range of the rotating stop band zones decreases as the speed of the drill string increases. This fact is illustrated experimentally in Fig. 4.10.

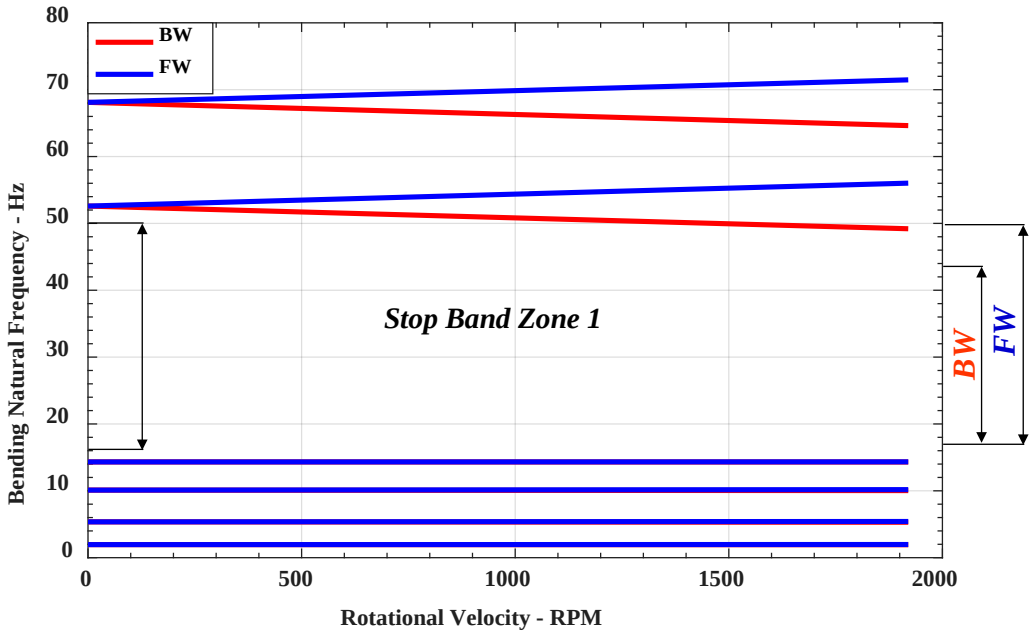

Fig. 3.11 Campbell diagram of passive periodic drill string at 1920 *RPM* (32 *Hz*), (*BW* = Backward Whirl & *FW* = Forward Whirl)

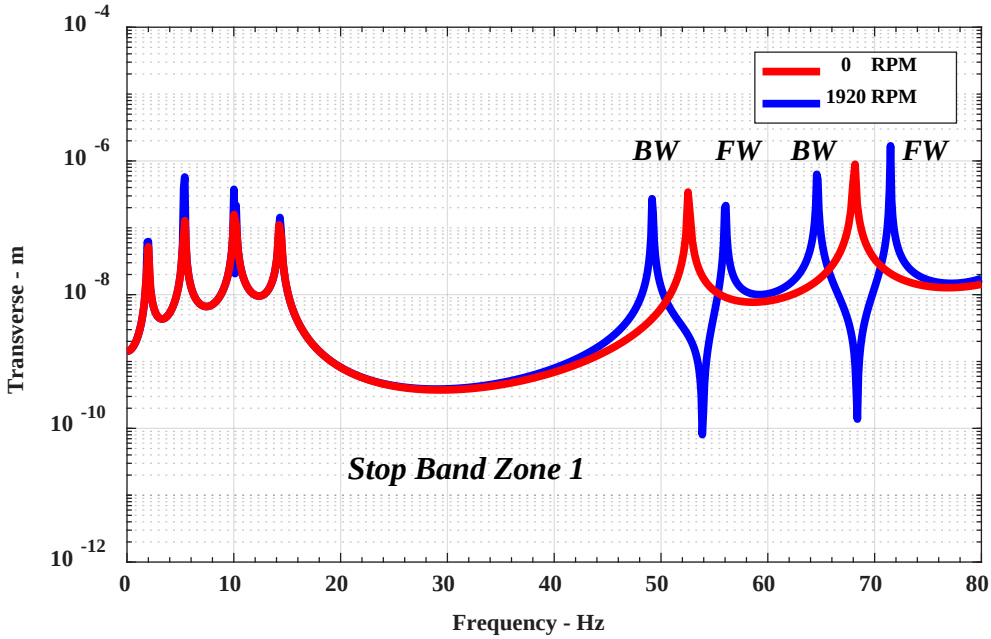

Fig. 3.12 Non-collocated lateral frequency response of passive periodic drill string at rotational speeds of zero and 1920 *RPM*, (*BW* = Backward Whirl & *FW* = Forward Whirl)

3.4 Full Scale Model Simulation

In order to establish a practical comparison between conventional drill string and the proposed design of periodic drill string with passive periodic inserts, the drill string full scale model of the parameters adopted in [11] and listed in Table 3.3 is considered.

The dynamic characteristics of the conventional and periodic drill string is investigated by subjecting the structure to a combination of torsional moment, axial and bending forces near the lower end and monitoring the vibration near the root of the structure. The design of periodic drill string is accomplished by dividing the drill pipe section into 300 periodic cells. The drill pipe section of the considered model is divided into 1800 elements while the drill collar section is divided into 200 elements. The boundary conditions of the considered drill string are assumed to be fixed at both ends of the drill string.

Fig. 3.13 displays comparison between the frequency response characteristics of the conventional drill string and the periodic drill string with 300 passive periodic inserts. The periodic inserts specifications are listed in Table 3.3. It should be noted that the size of the outer diameter of the drill collar in the considered model is slightly modified to accommodate for the size of the periodic inserts.

It is observed that the periodic drill string with passive periodic inserts generates stop band zones in the transverse direction only at low-frequency range extended between 25 – 35 *Hz*. However, the periodic inserts are not effective in mitigating the vibration for the axial and torsional directions in the considered range.

Fig. 3.14 displays the effect of the gyroscopic forces on the pass and stop band characteristics of the drill string when it is rotating at 1800 *RPM* (30 *Hz*) as compared with the non-rotating drill string. The 1800 *RPM* (30 *Hz*) is selected as a typical operating speed of the drill string. It can be seen that there is no significant gyroscopic effect on the spectral width of the stop band.

Table 3.3 Drill string and periodic insert specifications for the considered model in [11]

Drill Pipe Geometric Properties	**Value**	
Drill Pipe Length, $\boldsymbol{L_p}$	1000	*m*
Drill Pipe Outer Diameter, $\boldsymbol{D_o}$	0.127	*m*
Drill Pipe Inner Diameter, $\boldsymbol{D_i}$	0.095	*m*
Drill Collar Geometric Properties		
Drill Collar Length, $\boldsymbol{L_c}$	200	*m*
Drill Collar Outer Diameter, $\boldsymbol{D_o}$	0.2286	*m*
Drill Collar Inner Diameter, $\boldsymbol{D_i}$	0.095	*m*
Periodic Insert Geometric Properties		
Length, $\boldsymbol{L_i}$	0.25	*m*
Outer Diameter, $\boldsymbol{D_{o_i}}$	0.2355	*m*
Inner Diameter, $\boldsymbol{D_{i_i}}$	0.095	*m*
Material Properties		
Mass density, $\boldsymbol{\rho}$	7850	kg/m^3
Modulus of Elasticity, $\boldsymbol{E}$	210	*GPa*
Shear Modulus, $\boldsymbol{G}$	76.923	*GPa*

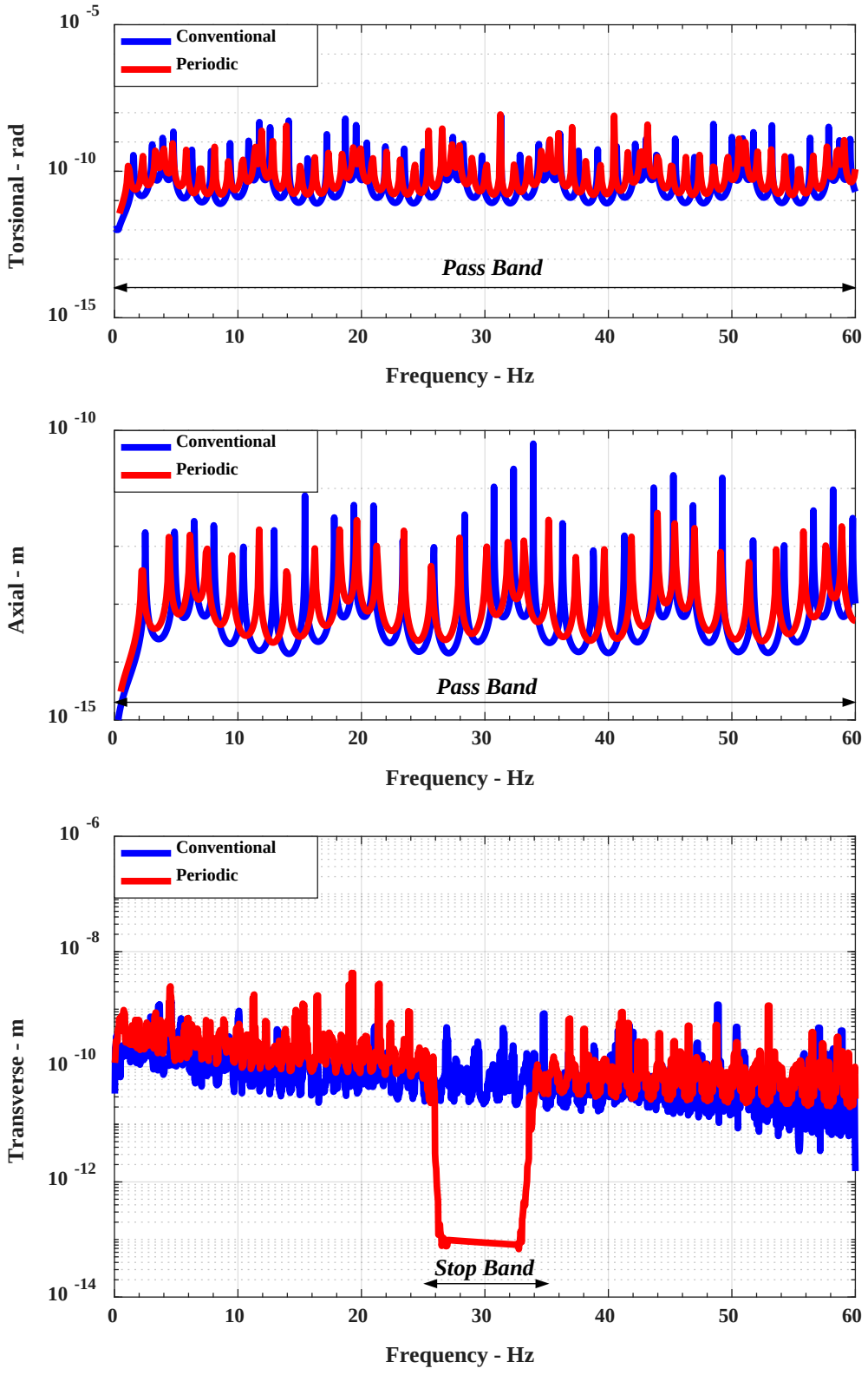

Fig. 3.13 Non-collocated frequency response comparison between conventional and periodic drill strings with 300 passive periodic inserts

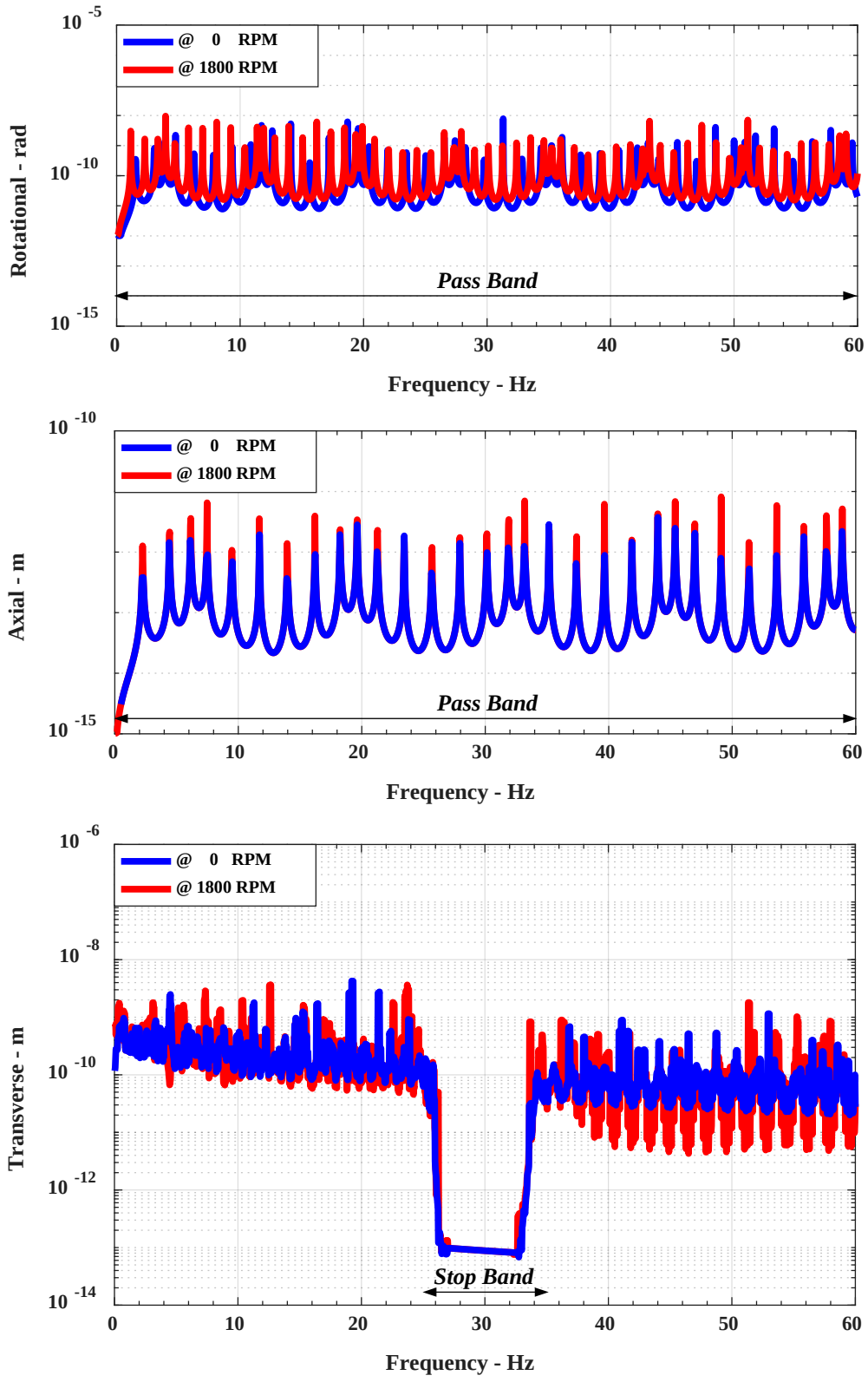

Fig. 3.14 Periodic drill string with 300 passive periodic inserts comparison between rotational velocity of zero and 1800 *RPM* (30 *Hz*)

3.5 Summary

The dynamic characteristics of passive periodic drill string are presented in this chapter. For a non-rotating periodic drill string, the periodic theory is implemented to extract the transfer matrix of the unit cell to determine its stop and pass band characteristics. For a gyroscopic periodic drills string, the "*band gap*" characteristics are determined by developing a novel approach, which is based on the concept of Bloch wave propagation theory in periodic structures. In this approach, the dispersion curves of the periodic gyroscopic systems are determined for different rotational speeds. The obtained characteristics are compared with non-rotating systems in an attempt to quantify the effect of the gyroscopic forces on the "*band gap*" characteristics. Numerical simulations are performed to illustrate the merit of the developed approach on passive periodic drill string.

Chapter 4

Experimental Results

4.1 Overview

This chapter presents the different experiments carried out for conventional and passive periodic drill string using a laboratory scale model in attempts to validate the theoretical predictions of chapters two and three. The laboratory experimental setup along with a detailed description is provided. The experimental dynamic characteristics of conventional and periodic drill string are compared with those obtained previously from periodic structures and the Bloch waves propagation theories based on the finite element model described in chapter two. It should be noted that the focus of this experimental work is placed on monitoring the effect of the periodic inserts on filtering out the transverse vibration of the drill string.

4.2 Experimental Set-up

The experimental arrangement construction along with the equipment used is described in this section. Using a laboratory scale model, the experimental setup of the proposed concept of periodic drill string is displayed photographically in Fig. 4.1. A support system consists of frame system (80/20) and a one-inch thick plywood sheet is built and firmly attached to the laboratory wall. An inverted lathe machine from JET (Model JWL-1221VS) is fixed to the wall support system. The speed of the lathe ranges between 60 to 3600 RPM controlled by electronic variable speed dial which facilitates the selection of the desired operating speed of the drill string.

The periodic drill string used in this experiment is assembled by using stainless steel solid shaft and periodic inserts. The drill string boundary conditions are assumed to be fixed at its upper end and simply supported at its lower end $(L - L_{in})$ where it is connected to a one-inch long sleeve bearing. The periodic drill string is excited using an electromagnetic shaker connected to the drill string through a carbon fiber stinger located approximately at $(L - 3)$. The drill string material and geometric properties are presented in Table 3.1.

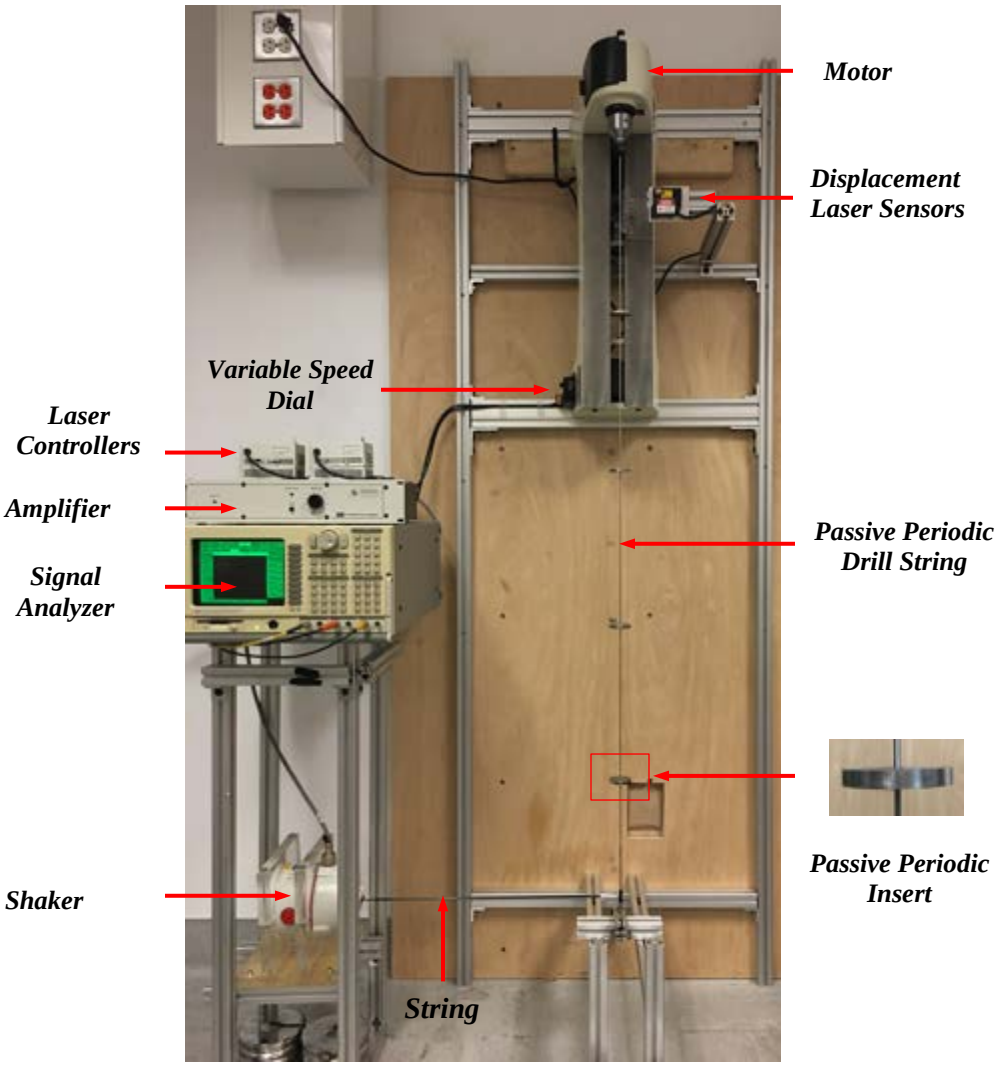

Fig. 4.1 Photograph of the periodic drill string experimental setup

The electromagnetic shaker is connected to a power amplifier. The specifications of the electromagnetic shaker (V408, from LDS Test and Measurement LLC, Middleton, WI) are listed in Table 4.1. Table 4.2 lists the specifications of the power amplifier of the shaker (PA100E, from LDS Test and Measurement LLC, Middleton, WI).

Table 4.1 Electromagnetic shaker specifications (V408 – LDS Test and Measurement LLC, Middleton, WI)

Shaker Properties	**Value**	
System sine force peak (naturally cooled)	98	N
System sine force peak (forced cooling)	196	N
Shaker max random force rms	89	N
Max acceleration sine peak	100	g
System velocity sine peak	1.78	m/s
System continuous displacement (pk-pk)	17.6	mm
Moving element mass	0.2	kg
Usable frequency rang	5-9,000	Hz

Table 4.2 Shaker power amplifier specifications, (PA100E – LDS Test and Measurement LLC, Middleton, WI)

Power Amplifier Properties	Value	
Rated sinusoidal power output matched	147	W
Resistive load	2.9	Ω
Max. continuons sinusoidal VA output, 0.5pf	147	VA
Frequency range at rated power	10 Hz–10 kHz	
Total harmonic distortion at rated output 20Hz-10kHz	Type 0.5	%
Max. output voltage	20	Vrms
Max. no load voltage	32	Vrms
Voltage regulations	3	%
Output current at rated VA	7A	rms
Random output	14 A	pk
Over-current trip level	10A	rms
Input sensitivity for max output (4kHz)	1 V	rms
Signal to noise ratio	>75	dB
Amplifier efficiency	58	%

Two displacement laser sensors, LM 200 (ANL2535REC) are installed 90 degrees apart at a location 3.5 inches down from the drill string upper end. Fig. 4.2 shows photography the laser sensor arrangement. The sensor is usable over a measurable range of 44 - 56 mm with an accuracy of 4.5 μm over a frequency range 0 - 30 kHz.

The displacement laser sensors are connected to a dynamic signal analyzer, Stanford Research System (Model SR780) where the experimental data are acquired.

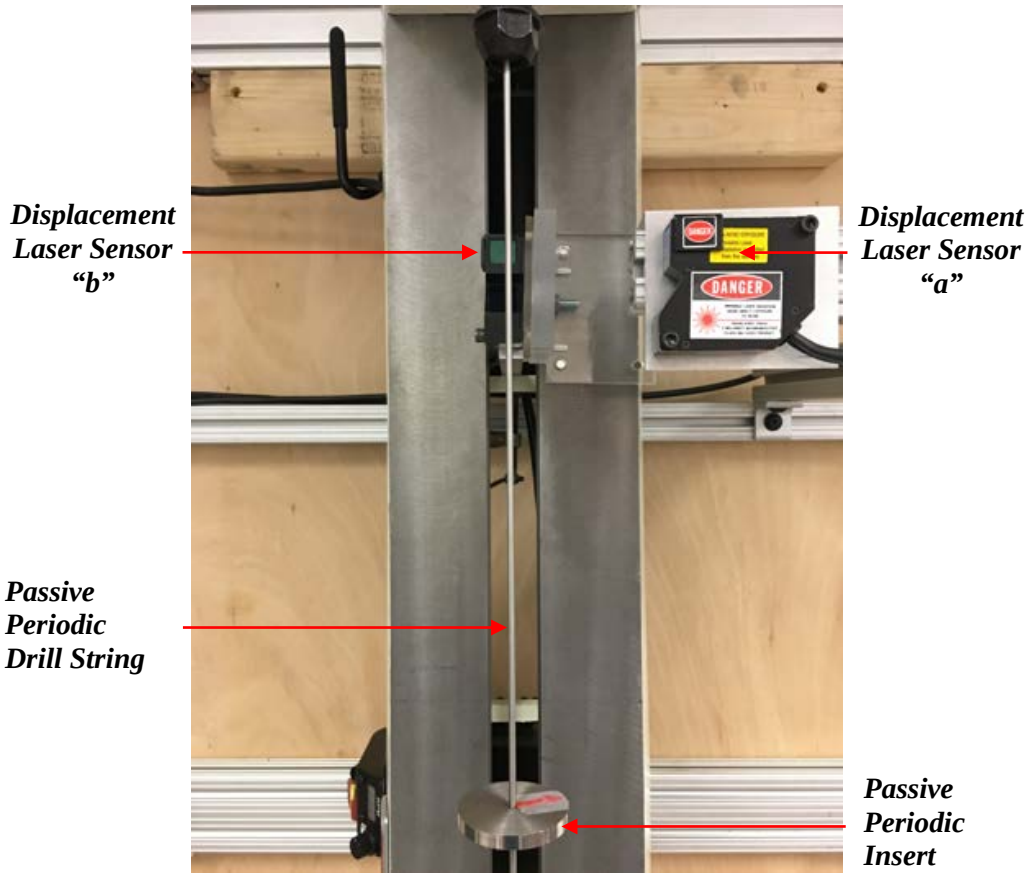

Fig. 4.2 Photograph of the displacement sensors arrangement

4.3 Performance of Conventional Drill String

The dynamic characteristics of the conventional drill string are measured in the frequency domain by subjecting the drill string to swept sine wave excitation. The drill string motion is provided by the electromagnetic shaker that excites the drill string through a one-inch sleeve bearing located approximately at ($L - 3$"). The drill string displacement frequency response is monitored using a displacement laser sensor "a" installed opposite to the excitation direction, at a location 3.5 inches down from the

drill string upper end as indicated in Fig. 4.2. The sensor is connected to the dynamic signal analyzer where the experimental data are acquired.

4.3.1 Predictions of Resonant Frequencies

The experimentally measured values of the bending natural frequencies of the conventional drill string with the effect of the shaker excitation along with those predicted by the developed *FEM MATALB*® algorithm and *ANSYS*® are listed in Table 4.3.

It can be seen that the experimental values are in excellent agreement with the predictions of the finite element model and *ANSYS*®.

The vibration mode shapes corresponding to the first four natural frequencies of conventional drill string are presented in Fig. 4.3.

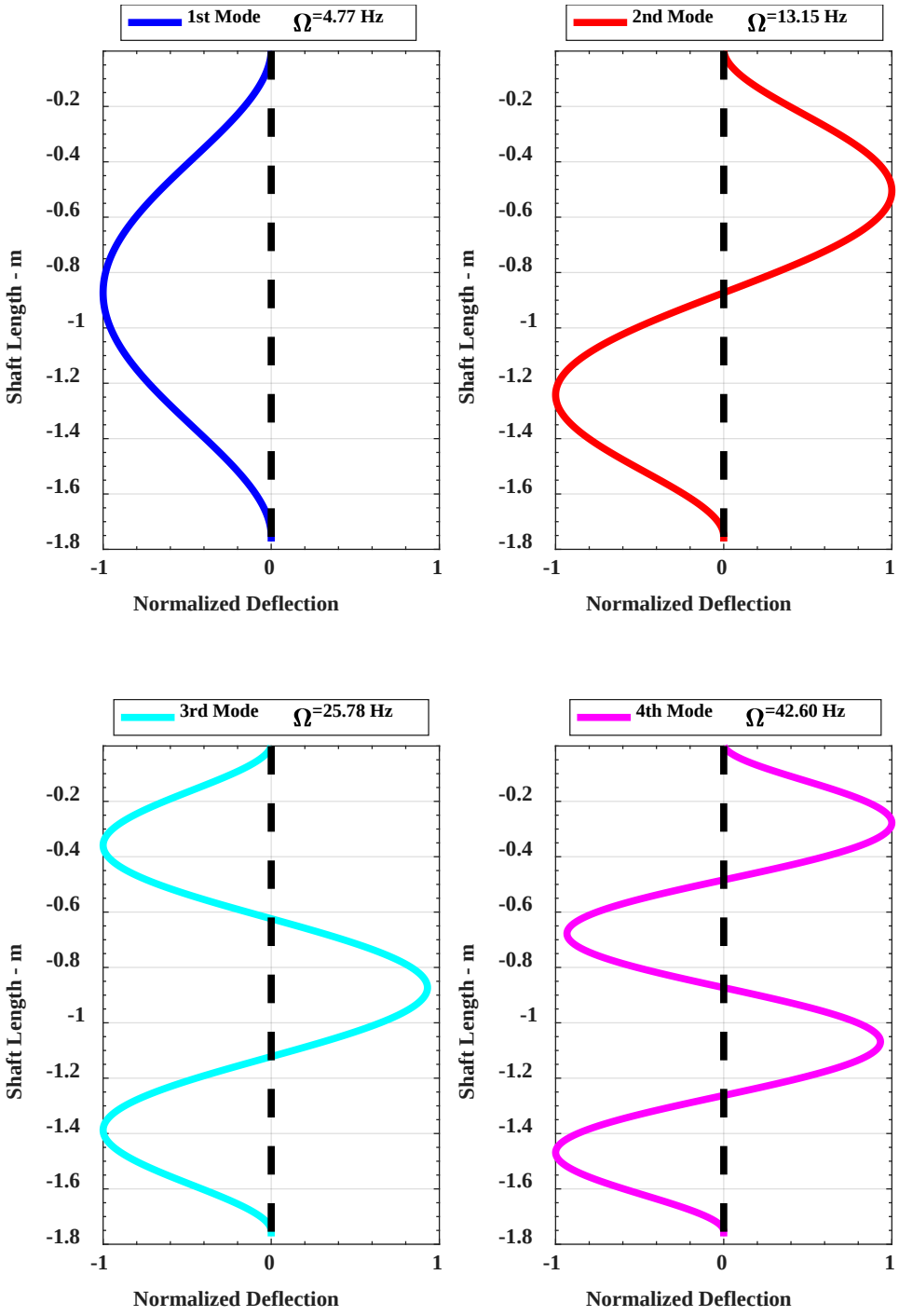

Fig. 4.3 Conventional drill string first four modes of vibration

Table 4.3 Conventional drill string bending natural frequencies comparison between experimental, *FEM MATALB*® and *ANSYS*®

Mode	Experiment (*Hz*)	MATLAB® (*Hz*)	Error (%)	ANSYS® (*Hz*)	Error (%)
1	4.97	4.77	4.02	4.81	3.31
2	13.08	13.15	0.54	13.25	1.28
3	25.16	25.78	2.46	25.97	3.22
4	41.39	42.60	2.92	42.93	3.71
5	64.30	63.66	1.00	64.12	0.28

4.3.2 Performance in Frequency Domain

Fig. 4.4 shows a Non-collocated frequency response comparison between the experimental results and the finite element model predictions when the conventional drill string is excited by a swept sinusoidal excitation.

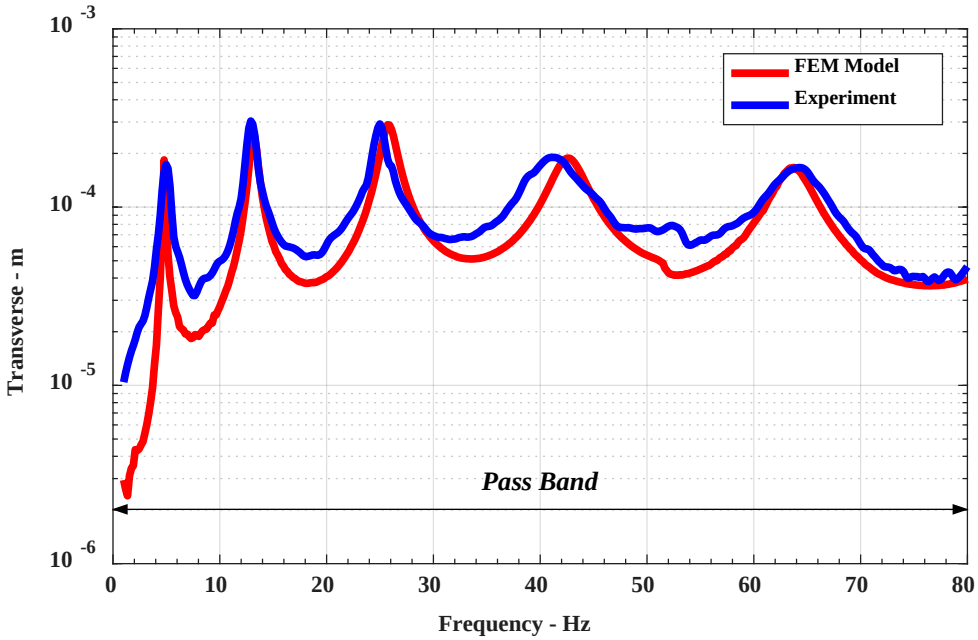

Fig. 4.4 Conventional drill string non-collocated frequency response comparison between the experimental results and *FEM* model

It is obvious from Fig. 4.4 that the predictions are in good agreement with the experimental results at the resonant frequencies. The conventional drill string in Fig. 4.4 experiences continuous vibration over the considered frequency band from 0 - 80 *Hz*. This band represents a continuous "*Pass Band*".

4.4 Performance of Non-Rotating Passive Periodic Drill String

A total of five stainless steel periodic inserts, shown in Fig. 4.1 and described in Table 3.1, are inserted into the conventional drill string to form the periodic drill string. To ensure structure periodicity, the periodic inserts are equally spaced along the drill string. The dynamic characteristics of the periodic drill string are measured with the same techniques used for conventional drill string, as previously described in section 4.3.

4.4.1 Predictions of Resonant Frequencies

Table 4.4 lists the bending natural frequencies of the non-rotating periodic drill string, with the effect of the shaker excitation, as predicted by the developed *FEM MATALB*® algorithm and *ANSYS*® in comparison with the experimentally measured values.

It can be seen that the experimental values are in excellent agreement with the predictions of the finite element model and *ANSYS*®.

4.4.2 Performance in Frequency Domain

A Non-collocated frequency response comparison between the experimental results and the finite element model predictions, when the non-rotating periodic drill string is excited by a swept sinusoidal excitation, is shown in Fig. 4.5.

It can be seen from Fig. 4.5 that the response exhibits a very wide "*stop band*" over the frequency range 15 – 46 *Hz* as predicted theoretically in Table 3.2. This fact clearly prove the effectiveness of the proposed concept in mitigating the vibration experienced by the drill string, particularly when excited within the stop band. In addition, the stop band range obtained experimentally is in excellent agreement with the one predicted by the Bloch waves propagation theory previously presented in section 3.3.3.

Fig. 4.6 shows a comparison between the experimental frequency response characteristics of the non-rotating periodic and the conventional drill strings. The figure displays clearly the effect of the concept of the periodic drill string in introducing a significant "*stop band*" characteristics.

Table 4.4 Non-rotating periodic drill string bending natural frequencies comparison between experiment, *FEM MATALB*® and *ANSYS*®

Mode	Experiment (*Hz*)	MATLAB® (*Hz*)	Error (%)	ANSYS® (*Hz*)	Error (%)
1	2.15	2.03	5.58	2.06	3.97
2	5.84	5.58	4.45	5.67	2.87
3	10.53	10.54	0.09	10.73	1.85
4	14.69	14.75	0.41	14.99	2.01
5	53.96	53.09	1.61	53.23	1.35
6	69.78	69.51	0.39	69.94	0.22

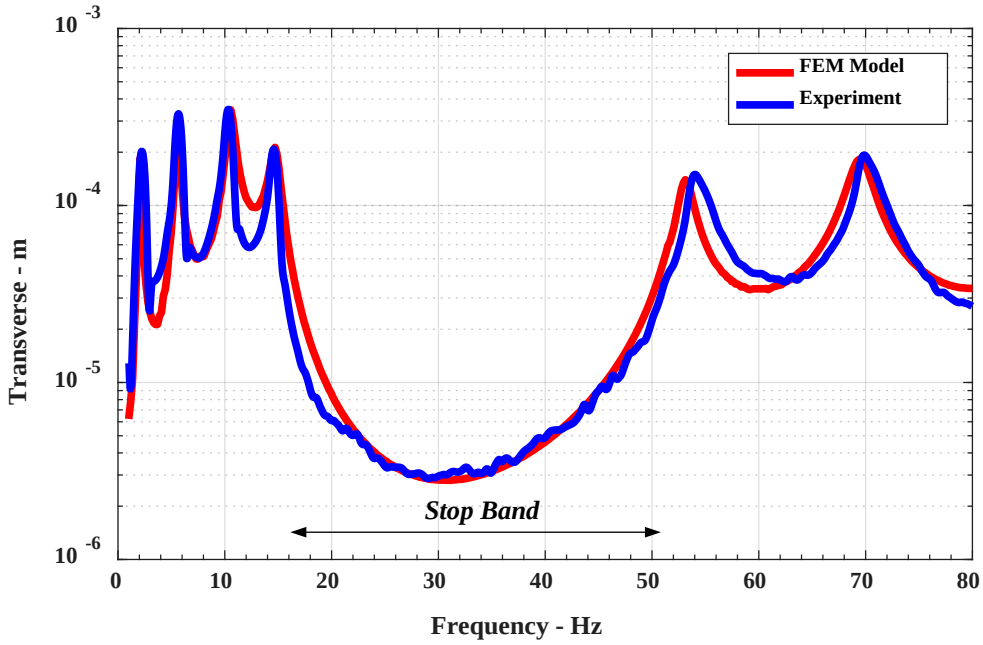

Fig. 4.5 Non-rotating periodic drill string frequency response comparison between the experimental results and *FEM* model

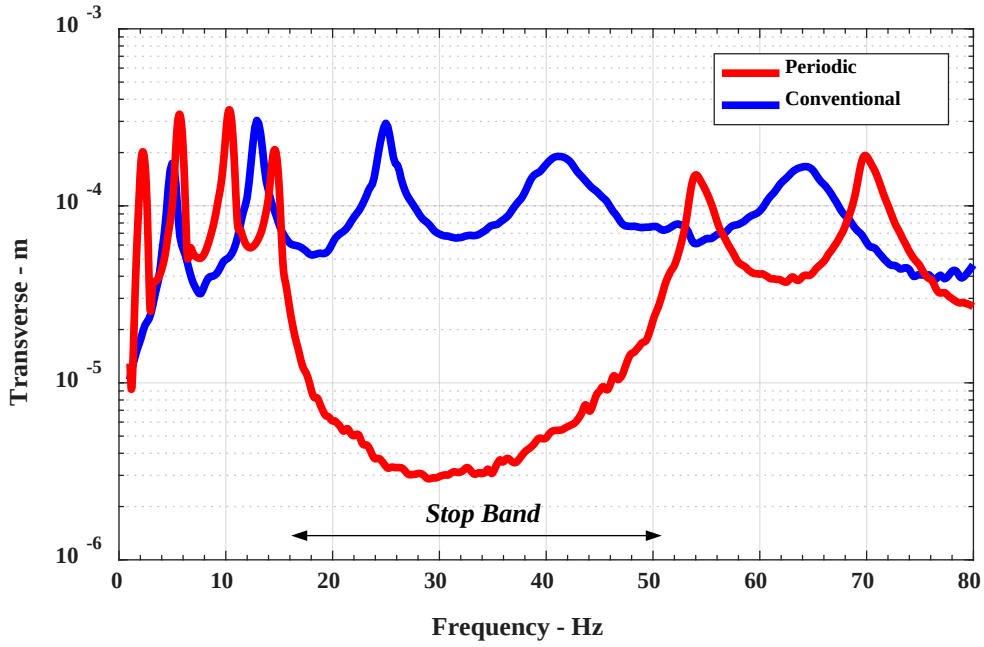

Fig. 4.6 Experimental results comparison between conventional drill string vs non-rotating periodic drill string

4.5 Performance of Gyroscopic Passive Periodic Drill String

Using the variable speed dial, the drill string is rotated at rotational speeds of 1200, 1920 and 2640 *RPM* (20, 32 and 44 *Hz*) respectively. The selected rotational speeds lay within stop band zone 1 as shown in Fig. 3.10.

4.5.1 Predictions of Resonant Frequencies

The experimentally measured values of the bending natural frequencies of the conventional drill string with the effect of the shaker excitation along with those predicted by the developed *FEM* and *MATALB*® algorithm are listed in Table 4.3.

It can be seen that the experimental values are in excellent agreement with the predictions of the finite element model.

Table 4.5 Periodic drill string bending natural frequencies comparison between experiment, *FEM* and *MATALB*® at 1200 *RPM* (20 *Hz*),

Mode		Experiment (*Hz*)	MATLAB® (*Hz*)	Error (%)
1	*BW*	2.08	1.95	6.25
	FW	2.08	2.03	2.40
2	*BW*	5.51	5.35	2.90
	FW	5.51	5.59	1.45
3	*BW*	10.20	10.10	0.98
	FW	10.20	10.55	3.43
4	*BW*	14.34	14.32	0.14
	FW	14.34	14.76	2.93
5	*BW*	51.31	50.73	1.13
	FW	55.82	54.97	1.52
6	*BW*	65.74	66.54	1.22
	FW	71.15	71.03	0.17

Table 4.6 Periodic drill string bending natural frequencies comparison between experiment, *FEM* and *MATALB*® at 1920 *RPM* (32 *Hz*)

Mode		Experiment (*Hz*)	MATLAB® (*Hz*)	Error (%)
1	*BW*	2.08	1.95	6.25
	FW	2.08	2.03	2.40
2	*BW*	5.51	5.34	3.09
	FW	5.51	5.60	1.63
3	*BW*	10.20	10.09	1.08
	FW	10.20	10.55	3.43
4	*BW*	14.34	14.32	0.14
	FW	14.34	14.76	2.93
5	*BW*	50.41	49.47	1.86
	FW	56.90	56.24	1.16
6	*BW*	64.66	65.30	0.99
	FW	71.87	72.20	0.46

Table 4.7 Periodic drill string bending natural frequencies comparison between experiment, *FEM* and *MATALB*® at 2640 *RPM* (44 *Hz*)

Mode		Experiment (*Hz*)	MATLAB® (*Hz*)	Error (%)
1	*BW*	2.08	1.94	6.73
	FW	2.08	2.04	1.92
2	*BW*	5.51	5.33	3.27
	FW	5.51	5.61	1.81
3	*BW*	10.20	10.07	1.27
	FW	10.20	10.56	3.53
4	*BW*	14.34	14.32	0.14
	FW	14.34	14.76	2.93
5	*BW*	49.15	48.24	1.85
	FW	58.16	57.49	1.15
6	*BW*	63.57	64.00	0.68
	FW	72.59	73.39	1.10

4.5.2 Performance in Frequency Domain

Non-Collocated frequency responses comparison between the experimental results and the finite element model predictions, when the rotating periodic drill string is excited by a swept sinusoidal excitation, are shown in Figs. 4.7-4.10.

It is evident in Figs. 4.7-4.10 that the gyroscopic responses still exhibit a very wide "*stop band*" when compared to non-rotating response. However, the gyroscopic stop band range splits into backward and forward stop band range as the speed of the drill string increases due to the gyroscopic forces effect. The range of the backward stop band decreases as the speed of the drill string increases while the range of the forward stop band increases as the drill string speed increases. This fact clearly prove the effectiveness of the proposed concept in mitigating the vibration experienced by the gyroscopic drill string, particularly when excited within the stop band. In addition,

the stop band range obtained experimentally is in excellent agreement with the one predicted by the Bloch waves propagation theory previously presented in section 3.3.3.

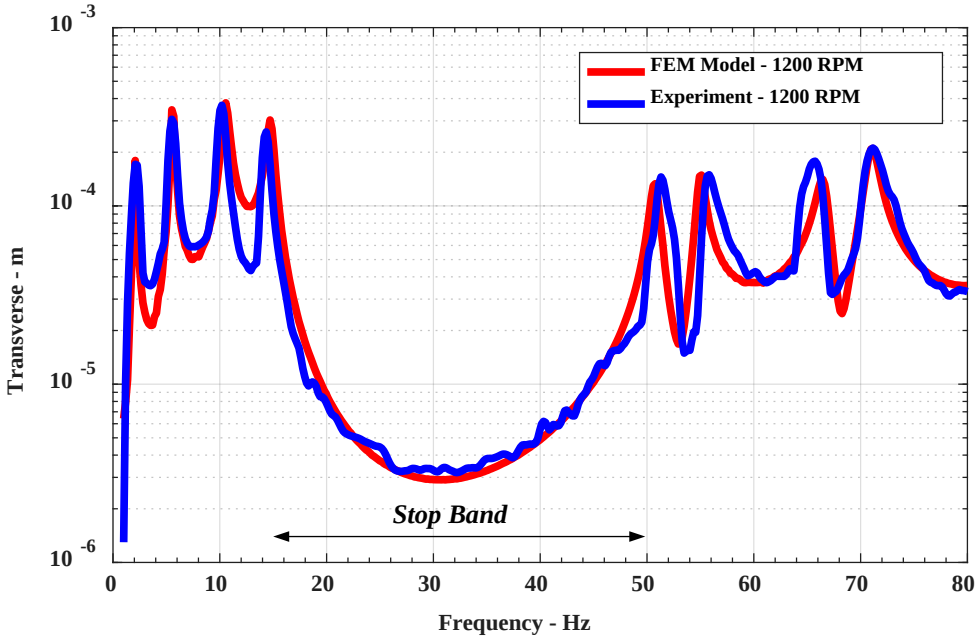

Fig. 4.7 Periodic drill string non-collocated frequency response comparison between the experimental results and *FEM* model at 1200 *RPM* (20 *Hz*)

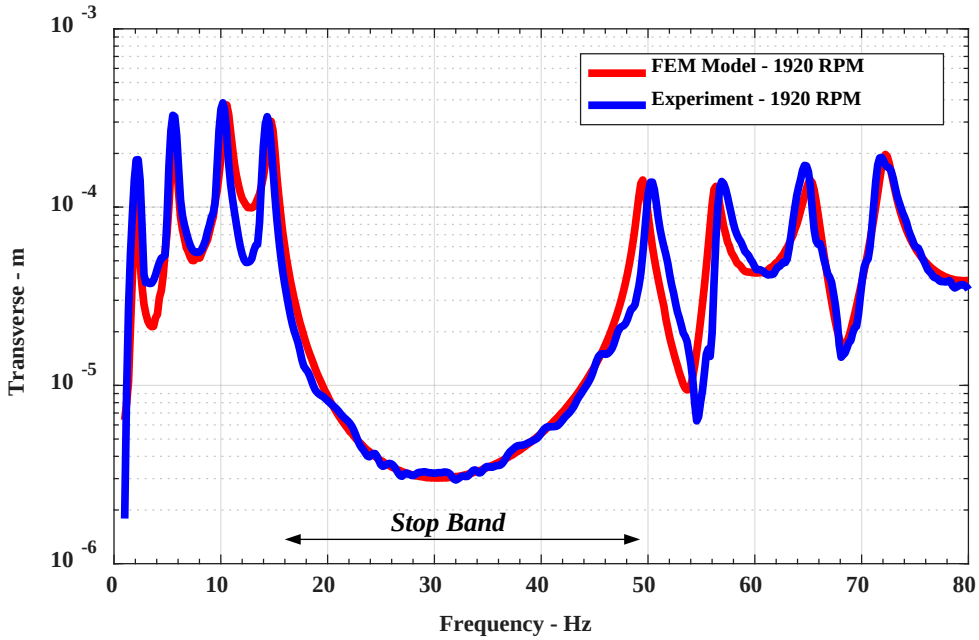

Fig. 4.8 Periodic drill string non-collocated frequency response comparison between the experimental results and *FEM* model at 1920 *RPM* (32 *Hz*)

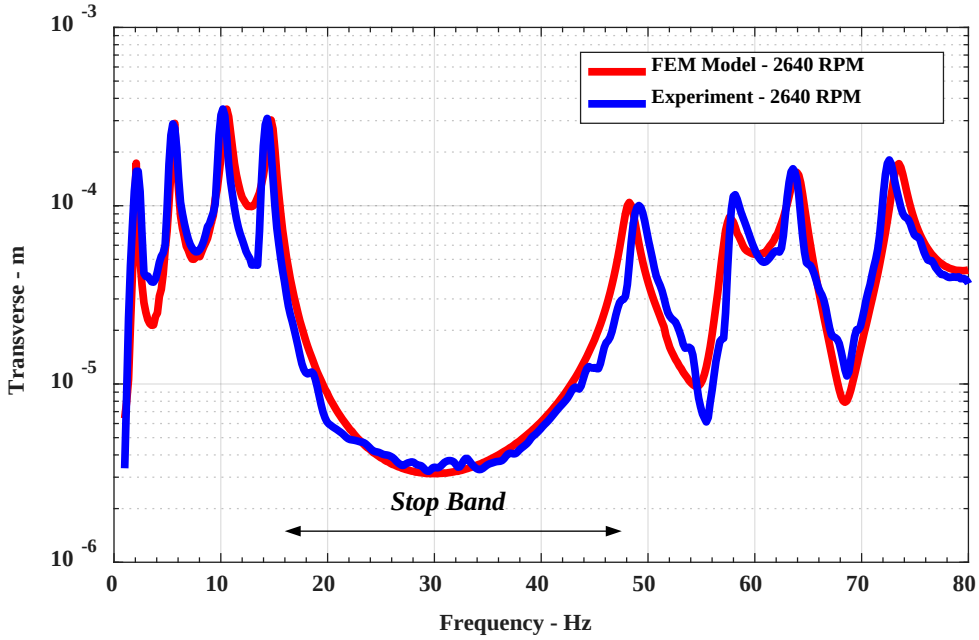

Fig. 4.9 Periodic drill string non-collocated frequency response comparison between the experimental results and *FEM* model at 2640 *RPM* (44 *Hz*)

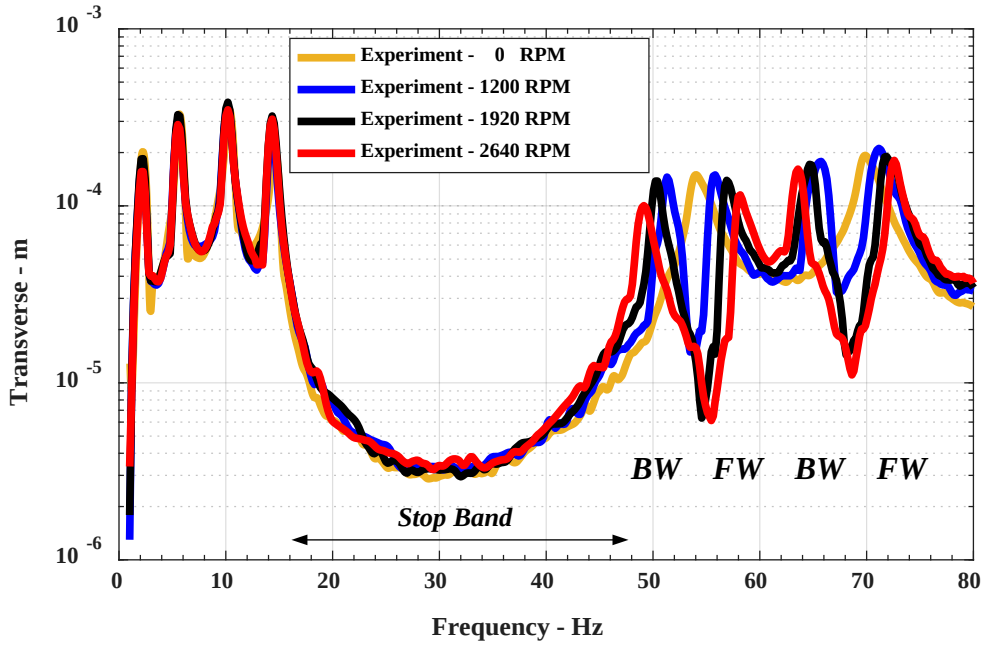

Fig. 4.10 Experimental results comparisons between periodic drill string rotational speeds of zero, 1200, 1920 and 2640 *RPM* (20, 32 and 44 *Hz*)

4.6 Summary

This chapter has presented an experimental realization of the proposed concept of passive periodic drill string. The experimental dynamic performance characteristics of a laboratory prototype of passive periodic drill string are determined. These characteristics are utilized to validate the predictions of the theoretical finite element model. Furthermore, the experimental results are determined also for conventional drill sting in order to provide basis for establishing the merits and effectiveness of periodic drill string in attenuating the structural vibration.

It has been demonstrated through the set of experimental results obtained by using prototype of the proposed concept of passive periodic drill string that periodic drill string exhibits a very wide "*stop band*" range while the conventional drill string exhibits a continues "*pass band*" range. In addition, it has been found that the model is capable of predicting the resonant frequencies as well as the frequency responses of both the conventional and periodic drill strings very accurately.

Chapter 5

Conclusions and Recommendations

5.1 Overview

This chapter summarizes the conclusions arrived at during the course of this research work. Presented also some recommended ideas which may be needed to expand the utility of the concepts proposed in this dissertation. Finally, the major contributions of the dissertation in relation to the current state-of-the-art in the field of vibration mitigation of drill strings are outlined.

5.2 Conclusions

This dissertation has presented an approach for determining the stop and pass bands (*i.e*. the "*band gaps*") characteristics of periodic gyroscopic systems using Bloch wave propagation theory. In this approach, the dispersion curves of the periodic gyroscopic systems are determined for different rotational speeds. The obtained characteristics are compared with non-rotating systems in an attempt to quantify the effect of the gyroscopic forces on the band gap characteristics. The developed approach is illustrated by a new class design of drill strings with passive periodic inserts whereby optimally designed and placed periodic inserts are utilized to filter out the vibration transmission along the drill strings. The comprehensive theoretical and experimental demonstration emphasize the effectiveness of the concept of drill strings with passive periodic inserts in mitigating the low-frequency vibrations of the drill string.

The dynamics and vibrations of such a class of structure are described by developing a finite element model (*FEM*). The developed *FEM* model is exercised to generate the dispersion characteristics of the gyroscopic unit cell of the passive periodic drill string. The experimental demonstration of the proposed class of periodic drill string exhibits a very wide "*stop band*" extending from 15 – 46 *Hz*. This stop band range splits into backward and forward range as the speed of the drill string increases due to the gyroscopic forces effect. This demonstration enhances the ability of this class of periodic drill string to operate over frequency bands that are wider than those possible with conventional drill strings.

5.3 Recommendations

This dissertation has attempted to establish the fundamentals governing the operation of a new class of passive periodic drill strings, and during this process has opened the door for a slew of unanswered questions that need to be addressed in future studies. Distinct among these issues is the need to model the interactions between the rock formation and the drill string in order to realistically account for these interactions in the finite element model. Hence, it would be possible to study the vibrations of the drill string which are caused by the resulting forces and moments. Experimental demonstration of these interactions would be essential to the validation of the developed finite element models.

Investigation of the interaction forces and moments on the stick-slip characteristics of the drill string, its stability as well as on its orbits is essential to the

understanding of the effect of the periodic inserts in improving the drill string performance as compared to conventional systems.

More work is needed to optimize the dimensions and the location of the passive periodic inserts in order to make the design of the new class of drill string minimum in weight, effective in controlling the vibration over a broad frequency band, and appealing to the oil industry.

Another natural extension of this work would be to provide the drill string with the active periodic inserts in order to tune the spectral characteristics of the stop bands according to the drilling depth and other operating parameters. During this process, it is essential to develop robust control strategy for the active periodic drill string to accommodate any uncertainty and reject the effect of the external disturbances acting on the drill string.

5.4 Major Contributions

This dissertation has presented the concept of drill strings with passive periodic inserts along with their performance characteristics. The comprehensive presentation of the passive periodic drill strings through mathematical modeling and experimental realization and evaluation emphasizes the following major contributions of the work to the current state-of-the-art of vibration mitigation of drill strings:

First, the concept of drill strings with passive periodic inserts is original and has not been considered at all in the open-literature for application to drill strings.

Second, the developed approach based on Bloch wave propagation theory for determining the stop and pass bands (*i.e*. the "*band gaps*") characteristics for periodic gyroscopic systems is pioneer in the field of periodic structures.

Last, the comprehensive theoretical and experimental demonstration of the effectiveness of the concept of drill strings with passive periodic inserts in mitigating the low-frequency vibrations of drill strings is another major contribution of this dissertation.

5.5 Summary

This chapter has presented a brief summary of the conclusions arrived at and the recommendations for the potential directions of extending the current work. In addition, the major contributions for this research work has been presented.

References

[1] L. V. d. Steen, "Suppressing Stick-Slip-Induced Drillstring Oscillations: A Hyperstability Approach," Ph.D. Dissertation, Netherlands: University of Twente, 1997.

[2] D. W. Dareing, "Drill Collar Length is a Major Factor in Vibration Control," *Journal of Petroleum Technology,* vol. 36, no. 4, pp. 637-644, 1984.

[3] P. D. Spanos, A. K. Sengupta, R. A. Cunningham and P. R. Paslay, "Modeling of Roller Cone Bit Lift-Off Dynamics in Rotary Drilling," *Journal of Energy Resources Technology,* vol. 117, no. 3, pp. 197-207, 1995.

[4] J. D. Jansen and L. Van Den Steen, "Active Damping of Self-Excited Torsional Vibrations in Oil Well Drillstrings," *Journal of Sound and Vibration,* vol. 179, no. 4, pp. 647-668, 1995.

[5] K. K. Millheim and M. C. Apostal, "The Effect of Bottomhole Assembly Dynamics on the Trajectory of a Bit," *Journal of Petroleum Technology,* vol. 33, no. 12, pp. 2323-2338, 1981.

[6] P. D. Spanos, A. M. Chevallier, N. P. Politis and M. L. Payne, "Oil and Gas Well Drilling: A Vibrations Perspective," *Journal of The Shock and Vibration Digest,* vol. 35, no. 2, pp. 85-103, 2003.

[7] A. A. Besaisow and M. L. Payne, "A Study of Excitation Mechanisms and Resonances Inducing Bottomhole-Assembly Vibrations," *SPE Drilling Engineering,* vol. 3, no. 1, pp. 93-101, 1988.

[8] T. V. Aarrestad, H. A. Tonnesen and A. Kyllingstad, "Drillstring Vibrations: Comparison Between Theory and Experiments on a Full-Scale Research Drilling Rig," in *SPE/IADC Drilling Conference,* Dallas, TX, Feb 9-12, 1986.

[9] J. D. Jansen, "Non-Linear Rotor Dynamics as Applied to Oilwell Drillstring Vibrations," *Journal of Sound and Vibration,* vol. 147, no. 1, pp. 115-135, 1991.

[10] S. L. Chen and M. Geradin, "An Improved Transfer Matrix Technique as Applied to BHA Lateral Vibration Analysis," *Journal of Sound and Vibration,* vol. 185, no. 1, pp. 93-106, 1995.

[11] Y. A. Khulief and H. Al-Naser, "Finite Element Dynamic Analysis of Drillstrings," *Finite Elements in Analysis and Design,* vol. 41, no. 13, pp. 1270-1288, 2005.

[12] A. S. Yigit and A. P. Christoforou, "Coupled Axial and Transverse Vibrations of Oil Well Drillstrings," *Journal of Sound and Vibration,* vol. 195, no. 4, pp. 617-627, 1996.

[13] A. P. Christoforou and A. S. Yigit, "Dynamic Modelling of Rotating Drillstrings with Borehole Interactions," *Journal of Sound and Vibration,* vol. 206, no. 2, pp. 243-260, 1997.

[14] S. A. Al-Hiddabi, B. Samanta and A. Seibi, "Non-Linear Control of Torsional and Bending Vibrations of Oilwell Drillstrings," *Journal of Sound and Vibration,* vol. 265, no. 2, pp. 401-415, 2003.

[15] H. Melakhessou, A. Berlioz and G. Ferraris, "A Nonlinear Well-Drillstring Interaction Model," *Sound and Vibration,* vol. 125, no. 1, pp. 46-52, 2003.

[16] R. I. Leine and D. H. van Campen, "Stick-Slip Whirl Interaction in Drillstring Dynamics," *Journal of Vibration and Acoustics,* vol. 124, pp. 209-220, 2002.

[17] N. Mihajlovic, N. van de Wouw, M. P. M. Hendriks and H. Nijmeijer, "Friction-Induced Limit Cycling in Flexible Rotor Systems: An Experimental Drillstring Set-Up," *Nonlinear Dynamics,* vol. 46, no. 3, pp. 273-291, 2006.

[18] Y. A. Khulief, F. A. Al-Sulaiman and S. Bashmal, "Vibration Analysis of Drillstrings with Self-Excited Stick-Slip Oscillations," *Sound and Vibration,* vol. 299, no. 3, pp. 540-558, 2007.

[19] Z. N. Ahmadabadi and S. E. Khadem, "Self-Excited Oscillation Attenuation of Drill-String System Using Nonlinear Energy Sink," *Proceedings of the Institution of Mechanical Engineers, Part C: Journal of Mechanical Engineering Science,* vol. 227, no. 2, pp. 230-245, 2013.

[20] X. Zhu and C. Lai, "Design and Performance Analysis of a Magnetorheological Fluid Damper for Drillstring," *International Journal of Applied Electromagnetics and Mechanics,* vol. 40, no. 1, pp. 67-83, 2012.

[21] H. Moradi, F. Bakhtiari-Nejad and M. Sadighi, "Suppression of the Bending Vibration of Drill Strings via an Adjustable Vibraiton Absorber," *International Journal of Acoustics and Vibration,* vol. 17, no. 3, pp. 155-163, 2012.

[22] S. A. Aldushaishi, "Investigation of Drillstring Vibration Reduction Tools," Master Thesis, University of Science and Technology, Missouri, USA, 2012.

[23] H. D. Nelson, "A Finite Rotating Shaft Element Using Timoshenko Beam Theory," *Journal of Mechanical Design,* vol. 102, no. 4, pp. 793-803, 1980.

[24] J. N. Reddy, An Introduction to Finite Element Method, 3rd Edition, New York: McGraw Hill, Inc., 2006.

[25] L. Meirovitch, "A New Method of Solution of the Eigenvalue Problem for Gyroscopic Systems," *AIAA,* vol. 12, no. 10, pp. 1337-1342, 1974.

[26] L. Meirovitch, Principles & Techniques of Vibrations, New Jersey: Prentice-Hall, 1997.

[27] T. Yokoyama, "Vibrations of a Hanging Timoshenko Beam Under Gravity," *Journal of Sound and Vibration,* vol. 141, no. 2, pp. 245-258, 1990.

[28] L. Brillouin, Wave Propatation in Periodic Structures, 2nd Edition, Dover, 1946.

[29] D. J. Mead, "Free Wave Propagation in Periodically Supported Infinite Beams," *Jouranl of Sound and Vibration,* vol. 11, no. 2, pp. 181-197, 1970.

[30] L. Cremer, M. Heckel and E. Ungar, Structure-Borne Sound, New York: Springer-Verlag Berlin Heidelberg, 1988.

[31] M. Faulkner and D. Hong, "Free Vibrations of a Mono-Coupled Periodic System," *Journal of Sound and Vibration,* vol. 99, no. 1, pp. 29-42, 1985.

[32] D. J. Mead, "Wave Propagation and Natural Modes in Periodic System: I. Mono-Coupled Systems," *Journal of Sound and Vibration,* vol. 40, no. 1, pp. 1-18, 1975.

[33] D. J. Mead and S. Markus, "Coupled Flexural-Longitudinal Wave Motion in a Periodic Beam," *Journal of Sound and Vibration,* vol. 90, no. 1, pp. 1-24, 1983.

[34] D. J. Mead, "Vibration Response and Wave Propagation in Periodic Structures," *ASME Journal of Engineering for Industry,* vol. 93, no. 1, pp. 783-792, 1971.

[35] D. J. Mead and Y. Yaman, "The Harmonic Response of Rectangular Sandwich Plates with Multiple Stiffening: A Flexural Wave Analysis," *Journal of Sound and Vibration,* vol. 145, no. 3, pp. 409-428, 1991.

[36] G. S. Gupta, "Natural Flexural Waves and the Normal Modes of Periodically-Supported Beams and Plates," *Journal of Sound and Vibration,* vol. 13, no. 1, pp. 89-111, 1970.

[37] Z. Liu, C. T. Chan and P. Sheng, "Analytic Model of Phononic Crystals with Local Resonances," *Physical Review B,* vol. 71, no. 1, p. 014103, 2005.

[38] M. Nouh, O. Aldraihem and A. Baz, "Vibration Characteristics of Metamaterial Beams with Periodic Local Resonances," *Journal of Vibration and Acoustics,* vol. 136, no. 6, p. 061012, 2014.

[39] L. Meirovitch, Fundamentals of Vibration, Long Grove, IL: Waveland, 2010.

[40] A. S. Yigit and A. P. Christoforou, "Coupled Torsional and Bending Vibrations Actively Controlled Drillstrings," *Journal of Sound and Vibration,* vol. 234, no. 1, pp. 67-83, 2000.

[41] A. P. Christoforou and A. S. Yigit, "Fully Coupled Vibrations of Actively Controlled Drillstrings," *Journal of Sound and Vibration,* vol. 267, no. 5, pp. 1029-1045, 2003.

[42] N. Mihajlovic, "Torsional and Lateral Vibrations in Flexible Rotor Systems with Friction," Ph.D. Dissertation, Eindhoven: Technische Universiteit Eindhoven, 2005.

[43] B. Hoie, "Drillstring Oscillations During Connections When Drilling From a Semi-Submersible Platform," Master Thesis, Stavanger University, Stavanger, Norway, 2012.

[44] A. Esmaeili, B. Elahifar, R. K. Fruhwirth and G. Thonhauser, "Axial Vibration Monitoring in Laboratory Scale Using CDC MiniRig and Vibration Sensor Sub," in *Instrumentation and Measurement Technology Conference*, Graz, Austria, May 13-16, 2012.

[45] I. Boussaada, H. Mounier, S. I. Niculescu and A. Cela, "Analysis of Drilling Vibrations: a Time-Delay System Approach," in *Control and Automation (MED), 20th Mediterranean Conference*, Barcelona, Spain, July 3-6, 2012.

[46] A. Ghasemloonia, D. G. Rideout and S. D. Butt, "Coupled Transverse Vibration Modeling of Drillstrings Subjected to Torque and Spatially Varying Axial Load," *Proceedings of the Institution of Mechanical Engineers, Part C: Journal of Mechanical Engineering Science,* vol. 227, no. 5, pp. 946-960, 2013.

[47] Y. A. Khulief, F. A. Al-Sulaiman and S. Bashmal, "Laboratory Investigation of Drillstring Vibrations," *Proceedings of the Institution of Mechanical Engineers, Part C: Journal of Mechanical Engineering Science,* vol. 223, no. 1, pp. 2249-2262, 2009.

[48] Y. A. Khulief, F. A. Al-Sulaiman and S. Bashmal, "Vibration Analysis of Drillstrings with String-Borehole Interaction," *Proceedings of the Institution of Mechanical Engineers, Part C: Journal of Mechanical Engineering Science,* vol. 222, no. 1, pp. 2099-2110, 2008.

[49] T. G. Ritto, C. Soize and R. Sampaio, "Non-Linear Dynamics of a Drill-String with Uncertain model of the Bit-Rock Interaction," *International Journal of Non-Linear Mechanics,* vol. 44, no. 8, pp. 865-876, 2009.

[50] A. Bazoune and Y. A. Khulief, "Shape Functions of the Three-Dimensional Timoshenko Beam Element," *Journal of Sound and Vibration,* vol. 259, no. 2, pp. 473-480, 2002.

[51] S. H. Choi, C. Pierre and A. G. Ulsoy, "Consistent Modeling of Rotating Timoshenko Shafts Subject to Axial Loads," *ASME Journal of Vibration and Acoustics,* vol. 114, no. 2, pp. 249-259, 1992.

[52] ANSI/IEEE Std 176-1987, *Standard on Piezoelectricity.*

[53] Karkoub, M.; Zribi, M.; Elchaar, L.; Lamont, L.;, "Robust mu-Synthesis Controllers for Suppressing Stick-Slip induced Vibrations in Oil Well Drillstrings," *Multibody System Dynamics*, vol. 23, pp. 191-207, 2010.

[54] L. Li, Q. Zhang and N. Rasol, "Time Varying Sliding Mode Adaptive Control for Rotary Drilling System," *Journal of Computers,* vol. 6, no. 3, pp. 564-570, 2011.

[55] G. Downton, "Challenges of Modeling Drilling Systems for the Purposes of Automation and Control," in *IFAC Workshop on Automatic Control in Offshore Oil and Gas Production*, Norwegian University of Science and Technology, Trondheim, Norway, May 31 - June 1, 2012.

[56] V. Utkin, Sliding Modes in Control Optimization, Berlin: Springer-Verlag, 1992.